博士論文

Realization of 3D image reconstruction from transillumination images of animal body

生体透視像からの 3D 像再構成の実現

北海道大学大学院情報科学研究科

TRAN TRUNG NGHIA

学　位　論　文　内　容　の　要　旨

博士の専攻分野の名称　　博士（工学）　　氏名　Tran Trung Nghia

学　位　論　文　題　名

Realization of 3D image reconstruction from transillumination images of animal body
（生体透視像からの 3D 像再構成の実現）

Three-dimensional (3D) imaging with X-ray or MRI has contributed greatly not only to medical diagnosis, but also to life science. The number of experimental animals killed for experimentation would be reduced if the animals ’ internal structures can be visualized non-invasively. In transillumination imaging using near-infrared (NIR) light, the location of internal bleeding, infection, and angiogenesis can be visualized. Functional imaging is also possible using spectroscopic principles. With specific contrast media, the usefulness of NIR imaging is expanded significantly. However, the NIR transillumination technique has not been used widely. The major reason for that relative lack of use is the difficulty of the strong scattering in tissues. In transillumination images, the deeper structure is blurred and cannot be differentiated from the shallower and less-absorbing structure. To overcome this problem, great effort has been undertaken to develop optical computed tomography (optical CT) techniques. The typical technique for a macroscopic structure is diffuse optical tomography (DOT). Using this technique, cross-sectional imaging of human breasts and infant heads was achieved. Once the cross-sectional images become available, 3D imaging is possible. However, current techniques require great computational effort such as finite element method calculation, and large devices such as numerous fiber bundles around the object body.

It would be possible to reconstruct the 3D structure with a common filtered back-projection algorithm and with a CCD or CMOS camera if the scattering effect in transillumination images can be suppressed effectively. They require much simpler and more compact device as well as much less computational effort. This study proposes the 3D imaging of internal absorbing structure of a small experimental animal from two-dimensional (2D) NIR transillumination images using new scattering suppression techniques. This thesis presents the principle, implementation, and the results to show the feasibility of the proposed method.

For scattering suppression, the deconvolution technique using the point spread function (PSF) is effective. In previous study, the PSF for the light source located inside the medium had been derived by applying the diffusion approximation to the equation of transfer. With a known depth of the light source in a diffuse medium, the light distribution can be recovered clearly through an interstitial tissue by the deconvolution with this PSF. Therefore, realization of the 3D imaging from the transillumination images can be expected if this light-source PSF can be applied to the transillumination image of light-absorbing structure. Through theoretical and experimental study, the applicability of the PSF for the light source to the transillumination images of the light-absorbing structure was confirmed. The

effectiveness of this technique was also confirmed in the experiments with a tissue-equivalent phantom and animal tissue.

The PSF is depth-dependent, and the technique explained above was applicable only for an object with known internal structure. To expand the applicability of this technique, new algorithms were devised. An observed transillumination image is deconvoluted with the PSFs of different depths. Then the deconvoluted images are summed up to produce a new image that serves as a projection image in cross-sectional reconstruction. The projection image contains the projection of the true absorption distribution and the incompletely deconvoluted projection as well. To suppress the effect of this erroneous projection, an erasing process was devised. An initial cross-sectional image is reconstructed from the projection images obtained from many orientations. It is used as a template to erase the erroneous distribution in the cross-section. After the application of this erasing process, a new improved projection image is formed in which the effect of the erroneous distribution is suppressed effectively. Using the projections from many orientations obtained in this process, an improved cross-sectional image can be reconstructed. With the cross-sectional images at different heights, the 3D image can be reconstructed.

The feasibility of the proposed technique was examined in a computer simulation and an experiment with a model phantom. The results demonstrated the effectiveness of the proposed technique. Finally, the applicability of the proposed technique to a living animal was examined. An anesthetized mouse was fixed in a transparent cylinder. To produce a transillumination image of good quality, a light trap in the cylinder was devised. Using the proposed technique, the 3D structure of the mouse abdomen was reconstructed. High-absorbing organs such as the kidneys and parts of the liver became visible.

Results of this study suggest that a new optical CT having different features from those of currently available techniques is possible. This simple system can provide a cross-sectional image and reconstruct the 3D structure of internal organ in the mouse body. It can provide a useful and safe tool for the functional imaging of internal organs of experimental animals and for optical CT imaging of the near-surface structure of a human body.

Contents

List of figures

Chapter 1
Introduction

Nowadays, in biomedical research, small animal imaging has become an essential translational tool between preclinical research and clinical application. The number of experimental animals killed for experimentation would be reduced if the animals' internal structures can be visualized non-invasively. Three-dimensional (3D) imaging with X-ray computed tomography (X-ray CT), magnetic resonance imaging (MRI), positron emission tomography (PET), and single photon emission computed tomography (SPECT) has contributed greatly not only to medical diagnosis, but also to life science. These imaging systems have been optimized for the non-invasive routine imaging of small animals [1.1–1.7]. However, the optical computed tomography (optical CT) using near-infrared light (NIR) constitute a promising powerful alternative imaging modality for noninvasive imaging of an animal body. Optical imaging has several advantages over existing imaging methods, such as the non-ionizing radiation, the requirement of relatively simple and inexpensive imaging equipment, the high sensitivity, and particularly well suited for the repeated and long-term studies events in live animals [1.7–1.22].

In transillumination imaging using near-infrared (NIR) light of 700–1200 nm wavelength region, the location of internal bleeding, infection, and angiogenesis can be visualized due to the low absorption coefficient of water, oxyhemoglobin, and de-oxyhemoglobin [1.23–1.30]. Functional imaging is also possible using spectroscopic principles [1.26–1.41]. With specific contrast media, the usefulness of NIR imaging is expanded significantly. Although, the possibility and the potential of the NIR transillumination technique were pointed out early [1.23–1.25], the technique has not been used widely. The major reason for that relative lack of use is the difficulty of the strong scattering in tissues [1.7–1.30]. In transillumination images, the deep structure is blurred and cannot be differentiated from the shallower and less-absorbing structure. To overcome this problem, great effort has been undertaken to develop optical computed tomography (optical CT) techniques. For macroscopic optical imaging, the diffuse

optical tomography (DOT) [1.42–1.53] and fluorescence tomography [1.7–1.22] are well known. Using this technique, cross-sectional imaging of the human breasts and the human heads was achieved [1.42–1.52]. Once the cross-sectional images become available, 3D imaging is possible. However, they commonly require sophisticated hardware such as numerous fiber bundles around the object body, and great computational effort such as finite element method calculation. It would be possible to reconstruct the 3D structure with a common filtered back-projection algorithm and with a CCD or CMOS camera if the scattering effect in transillumination images can be suppressed effectively. It requires much simpler and more compact device as well as much less computational effort.

This study proposes the 3D imaging of the internal absorbing-structure of a small experimental animal from two-dimensional (2D) NIR transillumination images using new scatter-suppression techniques. This thesis presents the principle implementation and to show the feasibility of the proposed method.

In the experiment, the NIR light from a laser (Ti:Sapphire, 800 or 850 nm wavelength) through a beam expander for homogeneous illumination was used as the light source. An image is obtained using a cooled CMOS camera (C11440-10C; Hamamatsu Photonics K.K.) oriented toward the opposite face of the phantom to the light-incident side.

The image blurring in transillumination image can be considered as the convolution of a point spread function (PSF) of the scattering medium. For scattering suppression, the deconvolution technique [1.54,1.55] using the PSF is effective. In the previous study, the PSF for the light source located in the medium by applying the diffusion approximation to the equation of transfer had been derived [1.56]. With the known depth of the light source in a diffuse medium, the light distribution can be recovered clearly through an interstitial tissue by the deconvolution with this PSF. Therefore, realization of the 3D imaging from the transillumination images can be expected if this light-source PSF can be applied to the transillumination image of light-absorbing structure. Through theoretical and experimental study, the applicability of the PSF for the light source to the transillumination images of the light-absorbing structure was

confirmed. The effectiveness of this technique in the experiment with a tissue-equivalent phantom and an animal-tissue phantom were also confirmed.

The PSF is depth-dependent, and the technique explained above was applicable only for an object with known internal structure. To expand the applicability of this technique, new algorithms were devised. An observed transillumination image is deconvoluted with the PSFs of different depths. Then the deconvoluted images are summed up to produce a new image that serves as a projection image in cross-sectional reconstruction. The projection image contains the projection of the true absorption distribution and the incompletely deconvoluted projection as well. To suppress the effect of this erroneous projection, an erasing process was devised. An initial cross-sectional image is reconstructed from the projection images obtained from many orientations. It is used as a template to erase the erroneous distribution in the cross-section. After the application of this erasing process, a new improved projection image is formed in which the effect of the erroneous distribution is suppressed effectively. Using the projections from many orientations obtained in this process, an improved cross-sectional image can be reconstructed. With the cross-sectional images at different heights, a 3D image can be reconstructed.

The feasibility of the proposed technique was examined in a computer simulation and an experiment with a model phantom. The results demonstrated the effectiveness of the proposed technique. Finally, the applicability of the proposed technique to a living animal was examined. An anesthetized mouse was fixed in a transparent cylinder. To produce a transillumination image of good quality, a light trap in the cylinder was devised. Using the proposed technique, the 3D structure of the mouse abdomen was reconstructed. High-absorbing organs such as the kidneys and parts of livers became visible.

This thesis consists of nine chapters. The remainder of this thesis will follow the outline below.

Chapter 2 presents the background, the state of the art, and the aims of this study.

Chapter 3 describes the principles and the methodology.

Chapter 4 details the application of the light PSF to transillumination of light-absorbing object. The feasibility of applying the point spread function, which has derived for the light source located in the turbid medium, to the transillumination image of light-absorbing structure was investigated. The experiments were conducted in order to confirm the validity of the proposed method.

Chapter 5 describes the 3D reconstruction of the known-structure images. In order to verify and validate the effectiveness of the proposed method, the experiments with tissue-equivalent phantom and animal-tissue phantom were conducted.

Chapter 6 describes the 3D reconstruction of unknown-structure images. In the previous chapter, the technique was validated and the effectiveness was confirmed in experiments with the known-structure models. In this chapter a new technique has developed to expand the applicability of the proposed method to unknown structure. The effectiveness was investigated in simulation and experiment with complex structure.

Chapter 7 describes the 3D optical imaging of an animal body. A new technique has devised to obtain the transillunination image of animal body sensitively. The applicability of the proposed method to realize the 3D optical tomography for small animal was described.

Chapter 8 describes the preliminary study for more practical use. To expand the applicability of this research, some preliminary studies were conducted with promising results such as the localization of the physiological changes in animal body and the new depth estimation technique for simple structures.

Chapter 9 summarizes the results obtained by this study and discusses about the future works.

Chapter 2
Background

In this chapter, the most commonly used methods for small animal tomography imaging will be introduced and discussed the pros and cons of different imaging modalities. Then the optical tomography imaging will be presented as the background of this research with respect to the optical characteristics of the biological tissue. Finally, the aims of this research will be introduced.

2.1 Common small animal tomography imaging [2.1–2.7]

Nowadays, in biomedical research, small animal imaging played an essential role as a translational tool between pre-clinical research and clinical application. With the growing of this role, the availability of small animal imaging techniques became more crucial. The number of experimental animals killed for experimentation would be reduced if the animals' internal structures can be visualized non-invasively. Figure 2.1 shows the currently available imaging modalities for small animals. The most prominent and commonly three-dimensional (3D) imaging modalities included X-ray computed tomography (X-ray CT), magnetic resonance imaging (MRI), positron emission tomography (PET), and single photon emission computed tomography (SPECT). These imaging systems have been optimized and available for the use with small animal [2.1–2.7]. However, the optical computed tomography (optical CT) using near-infrared light (NIR) constitute a promising alternative imaging modality for noninvasive imaging of an animal body [2.7–2.22].

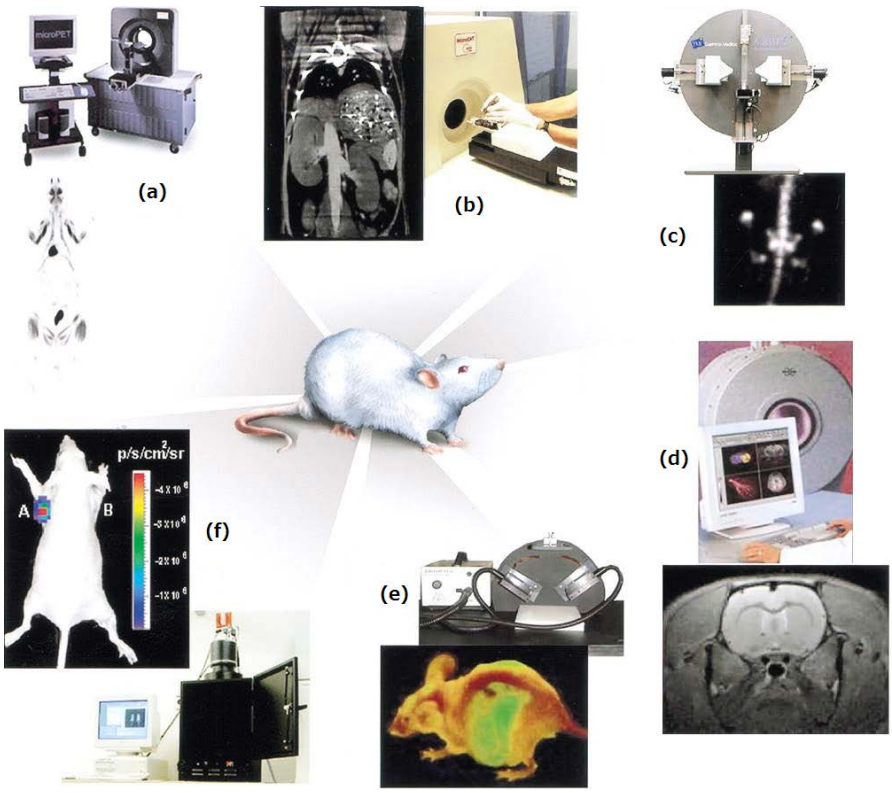

Fig. 2.1. Small animal imaging modalities with typical instruments available and illustrative example images that can be obtained with these modalities: (a) micro-PET, (b) micro-CT, (c) micro-SPECT, (d) micro-MRI, (e) optical reflectance fluorescence imaging, (f) optical bioluminescence imaging. (Figure adapted from [2.11]).

2.1.1 X-ray CT

Conventional X-ray CT is commonly used in clinical application. Almost of the systems adopt the third-generation CT (rotation/rotation scanner CT) scanning structure. The scanning geometry consists of the rotational bed and rotational gantry, as shown in Fig. 2.2. The radiation source and the detector are paired and rotated around the animal placed in the middle. The rotational gantry geometry usually provided higher spatial resolution than the rotational bed geometry since it avoided the movement of animal's soft tissues. The ray attenuation is different due to the density of tissue and result the contrast in capturing images. With these 2D images obtained in the circumferential direction, the 3D structures can be reconstructed by the computer.

However, the application for small animal has been limited due to the low spatial resolution. Recently, micro computed tomography (micro-CT) devices have been developed for small animal imaging with high spatial resolution as shown in Fig. 2.1(b).

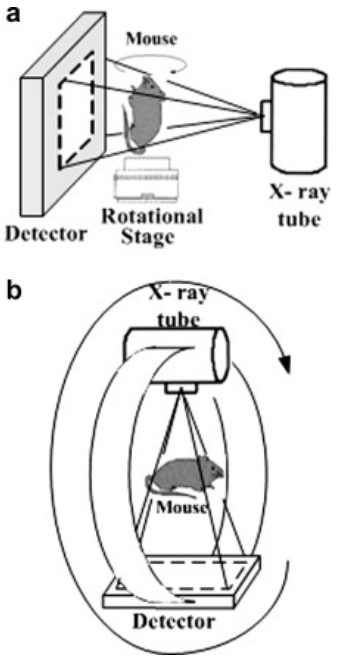

Fig. 2.2. Scanning geometry: (a) rotation bed, (b) rotation gantry. (Figure reprinted from [2.5]).

Figure 2.3 shows an example of small animal computed tomography. Figure 2.3(a) shows the schematic illustrating the principles of CT. Figure 2.3(b) shows an example of small animal CT axial images and 3D representation of tumor volumes in a genetically engineered mouse model of non-small-cell lung cancer. The images on the left (axial and 3D) show that lung tumors can be detected via CT (shown in red on 3D depiction).

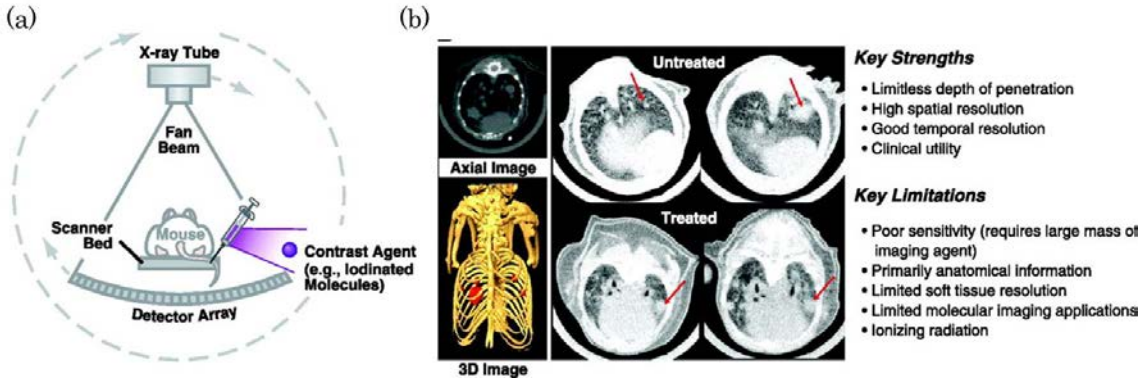

Fig. 2.3. Small animal computed tomography (CT): (a) schematic illustrating the principles of CT, (b) small animal CT axial images and 3D representation of tumor volumes in a genetically engineered mouse model of non-small-cell lung cancer. (Figure reprinted from [2.7]).

Although, the radiation dose is generally not lethal for small animal, the radiation is high enough to affect the biological tissue and other biological pathways that may change experimental results [2.1]. In addition, similar tissue types cannot be distinguished by this technique due to the quite poor contrast resolution.

2.1.2 MRI

Magnetic resonance imaging (MRI) is another common method of clinical imaging. Recently, it has been optimized to use for small animals. MRI is based on the facts that exploit the nuclear magnetic alignments of different atoms inside a magnetic field to generate images. MRI machines consist of large magnets that generate magnetic fields around the animal [2.2]. An MRI machine generally consists of three embedded coils: the main coil that generates the main relatively homogenous magnetic field, the gradient coils that produce variations in the magnetic field in the x, y, and z directions that are used to localize the source of the magnetic resonance signal, and the radio-frequency (RF) coils that generate an RF pulse responsible for altering the alignment of the magnetic dipoles. These paramagnetic atoms such as hydrogen, gadolinium, and manganese aligned themselves in the magnetic dipoles along the magnetic fields. While the magnetic field is temporarily ceased, these atoms turn back to their normal alignment. The signal of the relaxation of the atoms will be obtained. With this data, an image will be generated by the computer based on the resonance characteristics of

different tissue types.

Figure 2.4 shows an example of small animal magnetic resonance imaging. Figure 2.4(a) shows the schematic of the MRI machine. Figure 2.4(b) shows the cross-sectional images that obtained by MRI imaging.

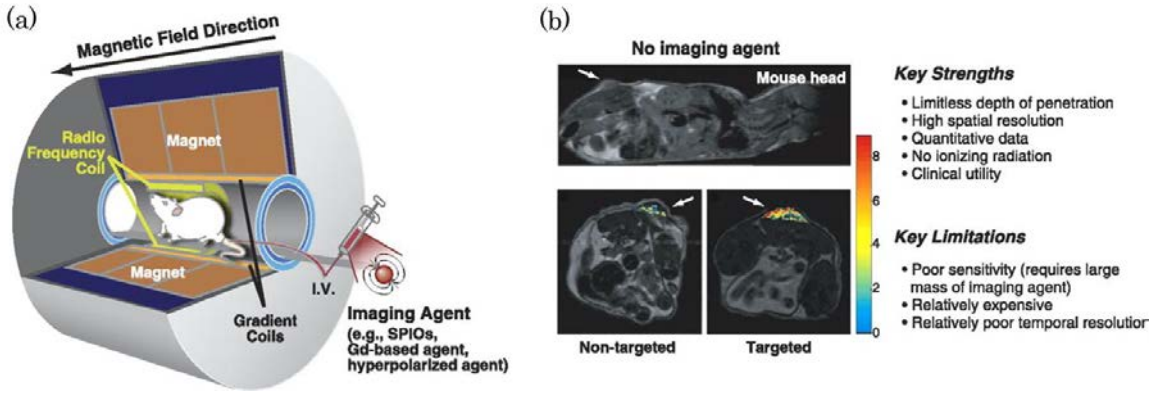

Fig. 2.4. Small animal magnetic resonance imaging (MRI): (a) schematic showing the basic principles of this technique, (b) Cross-sectional MRI images of the mouse, whereby the tumor is highlighted with an arrow. (Figure reprinted from [2.7]).

MRI is useful for detecting tumors and measuring morphological parameters since it has a good spatial resolution and contrast resolution to distinguish between normal and pathological tissue. However, the system is extremely expensive and the long image acquisition time may cause negative affects to anesthetized animals.

2.1.3 PET and SPECT

Positron emission tomography (PET) and single photon emission computed tomography (SPECT) are the nuclear medicine imaging techniques based on detection of gamma ray photons emitted from radionuclides (radioactive isotopes) injected into the body. PET requires the utilization of radioactive isotopes that emit positrons, such as ^{18}F, ^{15}O, ^{13}N, and ^{11}C, while SPECT uses tracers that emit gamma rays or high-energy X-ray photons, such as ^{123}I, ^{125}I, and ^{99m}Tc. As the radioisotopes decay, they emit positrons, which annihilate with electrons found naturally in the body, producing

two high energy gamma rays or photons traveling outward and in opposite directions to one another (180° apart). These gamma rays are detected by sensors on polar ends of the PET machine. The location of annihilation events are calculated by observing multiple events. Then the signal data set is converted into sinograms and reconstructed to produce tomographic images. In SPECT, gamma rays are directly emitted, instead of from annihilation events of a positron and electron. Unlike PET, the energy of gamma rays is attenuated. These rays will be captured by a γ-camera rotated around the object and subsequently rendered into images.

Figure 2.5 shows an example of small animal positron emission tomography. Figure 2.5(a) shows the schematic that illustrated the principle of PET. Figure 2.5(b) shows the images that obtained with PET in the example.

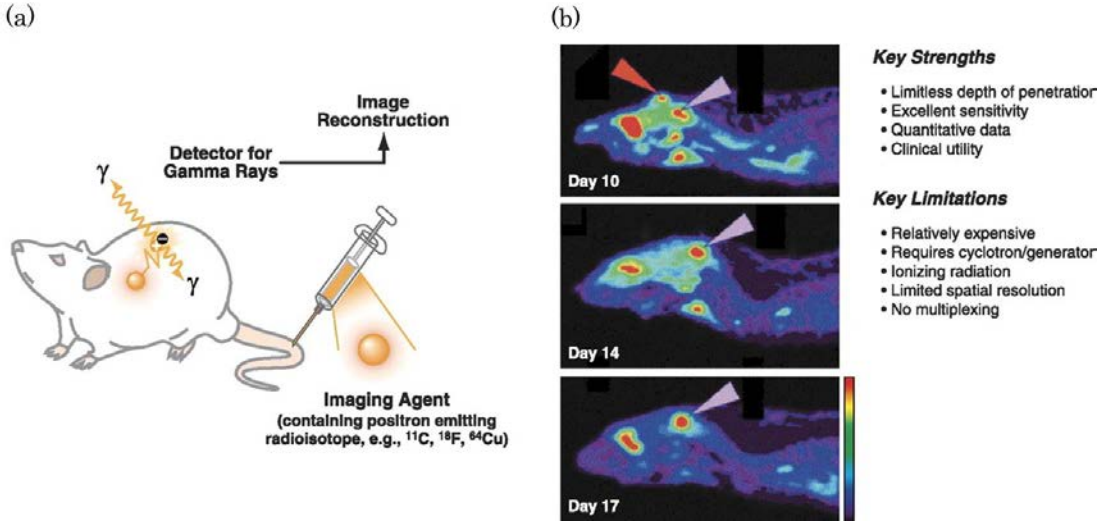

Fig. 2.5. Small animal positron emission tomography (PET): (a) schematic illustrating the basic principles of PET, (b) images demonstrating the noninvasive visualization of an orthotopic brain tumor in a rat. Pinks arrows show the tumor, and the red arrow shows wound due to intracerebral implantation of tumor cells. (Figure reprinted from [2.7]).

Figure 2.6 shows an example of small animal single photon emission tomography. Figure 2.6(a) shows the schematic that illustrated the principle of SPECT. Figure 2.6(b) shows the images that obtained by SPECT in the example.

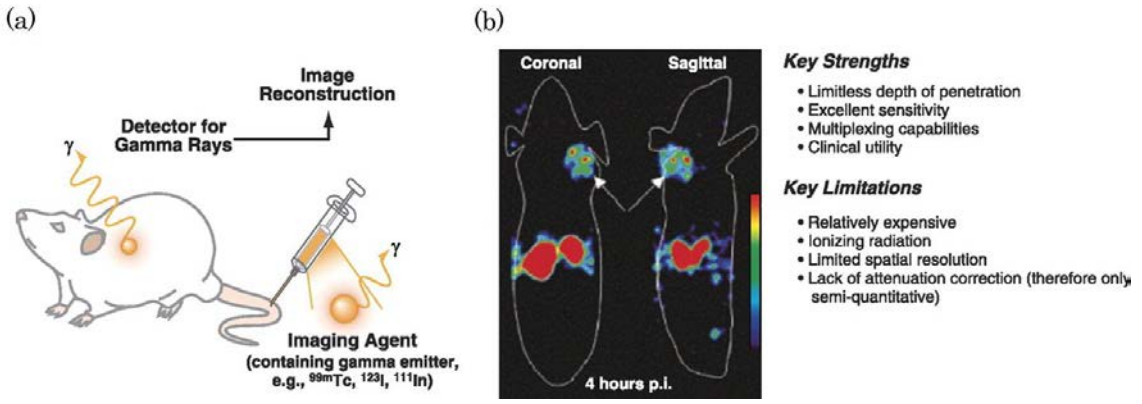

Fig. 2.6. Small animal single photon emission computed tomography (SPECT): (a) schematic illustrating the principles of SPECT, (b) SPECT images demonstrating the utility of visualizing gastrin-releasing peptide receptor in mice. Arrows point to tumor. (Figure reprinted from [2.7]).

Like X-ray CT, the radiation may cause some affects to the small animals, and thus extra control groups might be needed [2.11,2.20]. Due to the poor spatial resolution, these modalities needs to be used in conjunction with MRI or X-ray CT, which further decreases accessibility to the researchers because of high cost and specialized facilities.

2.2 Optical tomography imaging [2.7–2.83]

Optical imaging is based on the detection of the light propagated through the biological tissues. When the light propagates through the tissue, the photon propagation is strongly affected by absorption and scattering in the tissue. This technique utilizes the light in the near-infrared spectral region (700–1200 nm wavelength) wherein the major tissue chromophores are oxy-hemoglobin (HbO_2), deoxy-hemoglobin (Hb). The absorption from water and lipids can be neglected due to their low absorption in near-infrared region. In this region, photon transport is dominated by scattering, and light can penetrate a few centimeters below the tissue surface. Optical imaging has several advantages over existing imaging methods, such as the non-ionizing radiation, the requirement of relatively simple and inexpensive imaging equipment, the high sensitivity, and particularly well suited for the repeated and long-term studies events in live animals.

These advantages make optical imaging one of the most promising tools in preclinical research. With specific contrast media, the usefulness of NIR imaging is expanded significantly.

Figure 2.7 shows an example of optical fluorescence molecular imaging. An excitation light of appropriate wavelength is used to illuminate the animal as shown in Fig. 2.7(a). It leads to excitation of the fluorophore or fluorescent protein and the subsequent emission of light. The emitted light propagated throughout the tissue and then detected by a camera. Figure 2.7(b) shows the fluorescence images in the example.

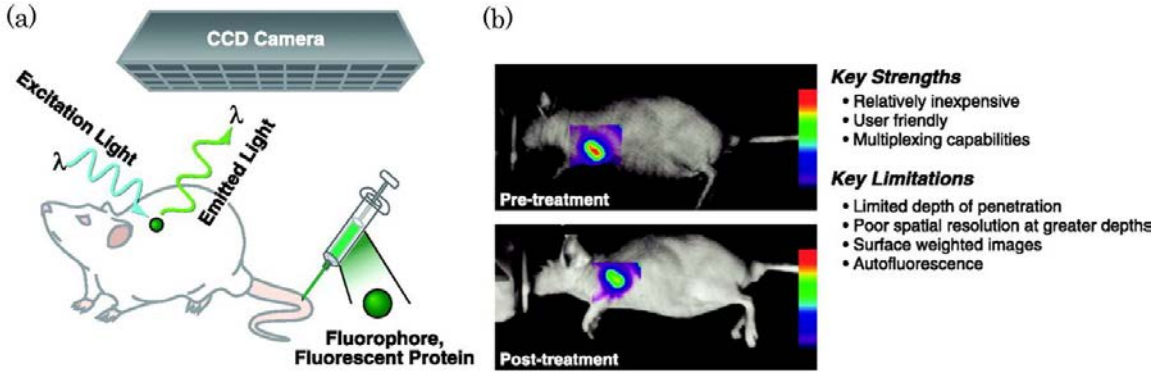

Fig. 2.7. Optical fluorescence molecular imaging: (a) schematic illustrating the principle of molecular imaging using optical fluorescence, (b) fluorescence images. (Figure reprinted from [2.7]).

Figure 2.8 shows an example of optical bioluminescence molecular imaging. First a small animal model needs to inject with cells that can express luciferase. Then an appropriate substrate needs to be administered to the animal. The enzymatic oxidation reaction of luciferase with its substrate will emit the light. The emitted light propagated throughout the tissue and then detected by a camera. Figure 2.8(b) shows the bioluminescence images in the example.

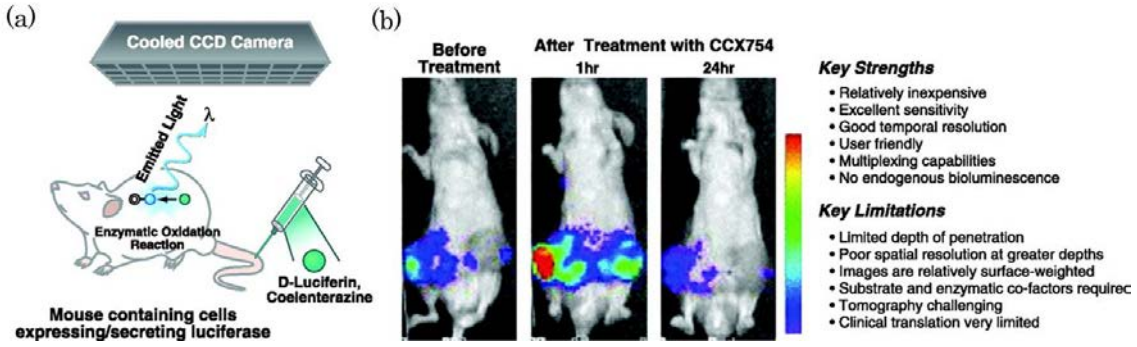

Fig. 2.8. Optical bioluminescence molecular imaging: (a) schematic illustrating the principle of molecular imaging using optical bioluminescence, (b) bioluminescence images. (Figure reprinted from [2.7]).

However, the technique has not been used widely due to the strong scattering in tissues. To overcome this problem, great effort has been undertaken to develop optical computed tomography (optical CT) techniques. For macroscopic optical imaging, the diffuse optical tomography (DOT) [2.23–2.34] and fluorescence tomography [2.7–2.22] are well known. The near-infrared light is injected into the tissue at the surface and the emerging light is detected at other interspersed points. Solution of the optical diffusion equation can be used to spatially map the optical characteristics of the tissue at several wavelengths so that spectral characteristics are measured. Using this technique, cross-sectional imaging of the human breasts and the human heads was achieved [2.23–2.33]. Once the cross-sectional images become available, 3D imaging is possible. The model of light propagation employed in DOT can be extended to simulate a secondary light source within the tissue, and the location and concentration of the fluorescent source can be reconstructed by following the same general principles of optical tomography. However, they commonly require sophisticated hardware such as numerous fiber bundles around the object body, and great computational effort such as finite element method calculation. Figure 2.9 shows an example of small animal imaging using diffuse optical tomography.

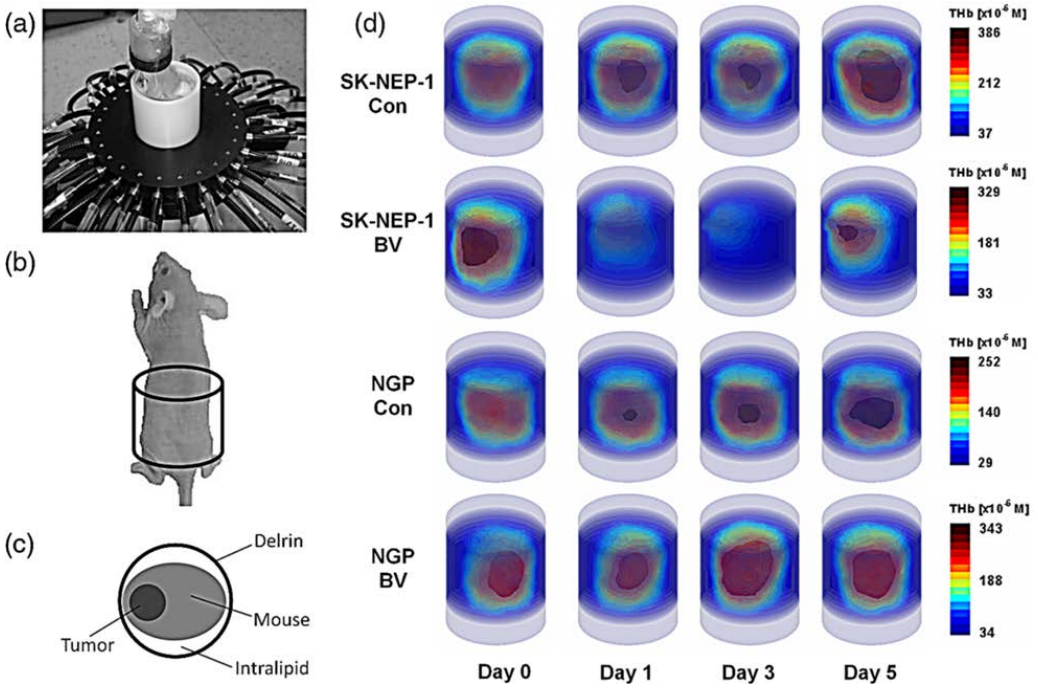

Fig. 2.9. Small animal imaging using diffuse optical tomography. (Figure reprinted from [2.34]).

2.2.1 Optical properties of biological tissue [2.35–2.43]

The interaction of photons with tissue is governed by the two physical phenomena: the absorption and the scattering. The extent of absorption and scattering by tissue are respectively described by the absorption coefficient μ_a and the scattering coefficient μ_s. In this thesis, they have the unit of mm^{-1}. Although both are important, the scattering is the dominant mechanism [2.37]. The optical properties of the biological tissue are not uniform due to the heterogeneous property of the tissue. The average refractive index of tissue is higher than the refractive index of air and considered to be around 1.4 for most tissue types [2.36].

Absorption coefficient

When a photon interacts with a single particle in tissue, some of the photon energy may be absorbed and converted into heat. The absorption coefficient μ_a is defined as the inverse of the distance travelled by a photon in the tissue before it is absorbed. In

considering that only the absorption events occur in a homogeneous medium, the transmitted light intensity I after absorption will follow the Beer-Lambert's law:

$$I = I_0 \exp(-\mu_a l), \qquad (2.1)$$

where I_0, μ_a, and l are respectively stand for the incident intensity, the absorption coefficient, and the optical path length. The absorption of biological tissue is minimal in the near-infrared region wherein the major tissue chromophores are oxy-hemoglobin (HbO_2), deoxy-hemoglobin (Hb). Other substances such as melanin, collagen, elastin, lipo-pigments, water and also lipids may have their contributions but generally not considered significant.

In the near-infrared window, light can transmit through tissues with the thickness of a few centimeters, while for wavelengths in infrared region and ultraviolet region, high attenuation of light results in a small penetration depth of hundredths of micrometers up to a few millimeters. Hence, at these wavelengths, only superficial assessment of tissues is possible, while near-infrared light allows for imaging tissues entirely.

The absorption coefficient of tissue at a specific wavelength can be calculated as a linear combination of each of the components weighted by their relative contribution in the tissue composition. Due to the low absorption of water and lipids in near-infrared region, the absorption coefficient can be calculated by

$$\mu_a^{\lambda} = \varepsilon_{Hb}^{\lambda}[Hb] + \varepsilon_{HbO_2}^{\lambda}[HbO_2], \qquad (2.2)$$

where ε is the extinction coefficient at wavelength λ. The terms $[Hb]$ and $[HbO_2]$denote the concentration of oxy-hemoglobin and deoxy-hemoglobin. This linear relationship can be used to estimate the concentration of $[Hb]$ and $[HbO_2]$ in a tissue by measuring the absorption coefficients at multiple wavelengths. This estimation provides an estimate of the functional state of the tissue. It refers to the functional optical imaging. Figure 2.10 shows the absorption spectra of different chromophores in biological tissues.

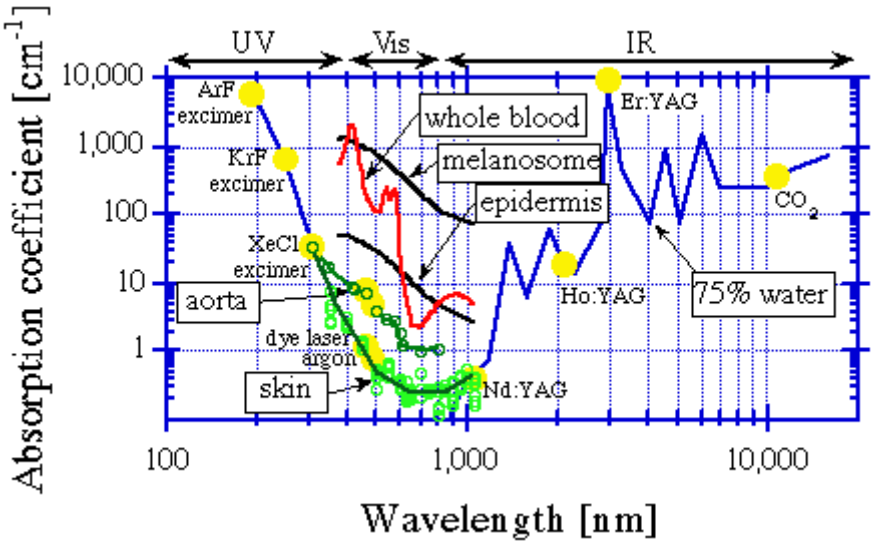

Fig. 2.10. The absorption spectra of major tissue chromophores. (Figure reprinted from [2.39])

Scattering coefficient

Scattering of light is another photon-tissue interaction that occurs that a photon will change its direction from its straight trajectory upon interacting with the particles in the tissue. The scattering coefficient μ_s is defined as the inverse of the distance travelled by a photon in the tissue before it undergoes scattering. This process is considered elastic without energy loss. The scattering coefficient is also wavelength dependent and follows the power law [2.38,2.41,2.43]:

$$\mu_s = A\lambda^{-b}, \qquad (2.3)$$

where A and b respectively stand for the scattering amplitude and the scattering power.

When a scattering event occurs, the direction of the scattered photon has to be determined. The Henyey-Greenstein phase function is commonly used to approximate the probability function of the direction of photon propagation after a scattering event, by introducing a parameter scattering anisotropy g. The value of g approaching 1, 0, and -1 describe extremely forward, isotropic, and highly backward scattering

respectively [2.35,2.37]. In biological tissue, it is typically between 0.69 and 0.99. For diffusion or multi-scattering, the combined effect of both these parameters is defined as the reduced scattering coefficient μ_s' that given by:

$$\mu_s' = (1-g)\mu_s, \qquad (2.4)$$

In this thesis, scattering will defined in terms of reduced scattering coefficient μ_s'.

2.2.2 Imaging geometry [2.44–2.52]

The geometry of imaging system played an important role in the reconstruction image. The two main geometries of imaging systems in small animal imaging are epi-illumination and transillumination as shown in Figure 2.11.

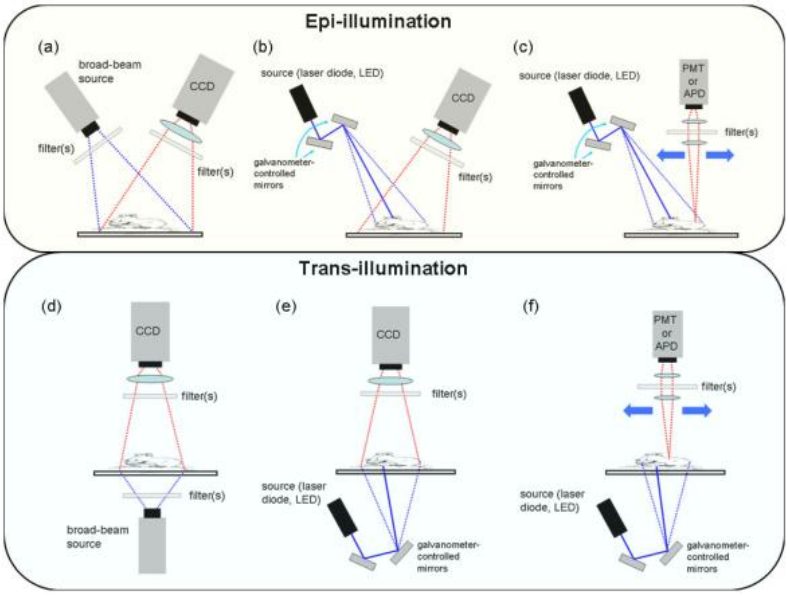

Fig. 2.11. Schematic rendering of different methods that can be used for whole-body fluorescence imaging: (a) broad beam illumination, (b) raster-scan illumination, (c) raster-scan illumination, (d) broad beam transillumination, (e) raster-scan transillumination, (f) raster-scan transillumination. The configurations optimized for tomography imaging and fiber-based planar configurations are not shown in this figure. (Figure reprinted from [2.19]).

Epi-illumination geometry

The epi-illumination refers to as reflectance imaging geometry where the light source and detector are on the same side of the animal model as shown in Fig. 2.11. The technique is referred to as Diffuse Optical Topography [2.47]. The light reflected or emitted off the surface of the animal is detected with fixed interval detectors. With a raster scan across the surface, a data set could be generated for tomographic imaging. The depth resolution is dependent on the source-detector configuration. With this geometry, the whole volume cannot be imaged due to the limited propagation of photons deep into the tissue in the case of high absorption and scattering [2.50]. This configuration can be used for the mapping biological activity in sub-surface tissue in conjunction with a mathematical model.

This geometry is commonly available in commercial systems because of its ease implementation such as Multispectral FX Prp (Kodak Carestream), Maestro (Caliper Life Sciences), IVIS 200 (Caliper Life Sciences), and Optix MX3 (ART Advanced Research Technologies). The research focused on improving the information content obtained by the commercial system by implementing time-resolved or frequency modulated data types [2.45,2.52].

Transillumination geometry

Transillumination geometry refers to the arrangement where the light source and detector are positioned on opposite sides of each others of the animal model as shown in Fig. 2.11. The detection of the photons transmitted through the entire volume provides a larger amount of tomographic information when compared to the epi-illumination geometry since it contained information from deep inside the tissue. Each measurement represents an average of the tissue volume sampled by the bulk of the tissue through which the light has passed [2.19]. The measurement techniques for tomographic imaging of small animals can be classified into two groups: the contact technique (fiber-based technique) and the non-contact technique.

The contact technique is based on the use of optical fibers to couple light into the

animal body, and detect the transmitted light at the surface of an animal body. The contact technique on the animal model surface needed a long acquisition time to measure the entire volume for tomographic measurements. Due to variations in optical properties and mouse thickness, some systems have designed a chamber filled with scattering fluid having optical properties similar to the tissue wherein the animal is submerged to reshape the animal's body shape into a known-shape. This technique is difficult to image the small animal body, which is irregularly shaped surface, and may have insufficient spatial resolution due to the limitation of the amount of fibers can practically be used for illumination and detection.

The non-contact transillumination technology is found to be more robust and accurate than the previous implementation of contact system [2.13]. It requires less acquisition time, simpler optical setup and much less computation effort. This technique is based on the use of CCD or CMOS camera for detection the transmitted light. This technique allowed to perform the illumination and detection of animal body in free-space without using the matching fluids. Furthermore, the projection data can be obtained in full-angle (360^{o}) of the animal body by using this system as it is done in X-ray CT. However, the tranillumination image is blurred due to the strong scattering effect in the tissue. The work for developing scattering suppression technique is crucial. There are a few commercially available imaging systems employing this imaging geometry such as IVIS Spectrum series (Caliper Life Sciences, USA) and the FMT2500 (Perkin Elmer, USA) [2.46,2.48, 2.49, 2.51].

Transillumination images contain more information and more sensitive to deeply seated fluorophores than those obtained with epi-illumination imaging. In addition, the transillumination image is weakly affected by the depth of fluorophores while the epi-illumination image decreases exponentially with depth [2.19]. Furthermore, transillumination measurements obtained significantly lower autofluorescence signals as compared to epi-illumination measurements [2.13]. Another possibility consists of incorporating tomographic image reconstruction technique such as the common filtered back-projection based on the model of light propagation in tissue [2.19].

2.2.3 Imaging domain [2.53–2.83]

Imaging domain refers to the illumination-detection technology used in the device which determines the type of data that is acquired by the measurement system. The optical tomographic measurement system can be classified into three groups that use continuous wave domain (CW), frequency domain (FD), and time domain (TD) instrumentation [2.12,2.44,2.62,2.65,2.69]. Each group requires different hardware that related to its illumination-detection scheme as shown in Fig. 2.12, and offers distinct advantages and disadvantages to the image reconstruction process.

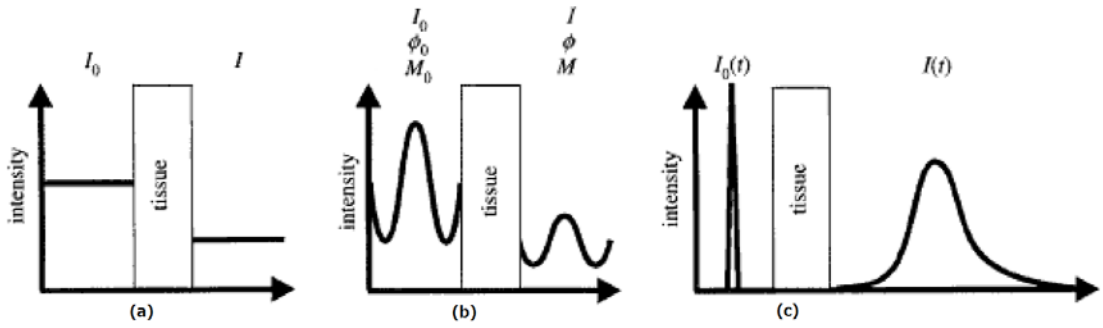

Fig. 2.12. The three imaging domains of optical imaging system: (a) continuous wave domain, (b) frequency domain, (c) time domain. (Figure adapted from [2.44])

Continuous wave imaging systems

The CW systems measure the steady state of the light signals by using a constant intensity illumination source with the detector for measuring the change in absolute intensity at the tissue boundary. The CW optical imaging system is the most widely used technique in experimental research and preclinical applications. They can be implemented with relatively simple, low-cost imaging equipment compared to FD and TD instrumentation, and relatively robust measurements with high signal-to-noise ratio (SNR) [2.59]. CW domain imaging is well suited for the sensitive detection of weak fluorescence signals in thick tissue [2.65]. However, the CW measurements provide limited information, content leading to non-unique solution in the inverse problem [2.54]. In addition, CW systems alone are unable to determine fluorescence lifetimes and

distinguish between the attenuation due to scattering and absorption coefficients [2.54]. The spatial resolution is entirely dependent on a tissue's optical properties and geometry and it is typically lower than in FD and TD tomographic imaging [2.65].

Frequency-domain imaging systems

The FD systems apply sinusoidal amplitude-modulated excitation light to the tissue volume and measure the attenuated amplitude and phase-shifted while light transmitted through the tissue [2.12,2.60,2.68,2.70,2.76]. These measurements at the detector positions on the tissue boundary are used to reconstruct information about the contribution of absorption and scattering in the tissue and the fluorescence intensity distribution [2.55,2.57,2.33,2.61,2.67]. However, these advantages can be only achieved by multiple frequency systems [2.55,2.66,2.67], where employing dense source-detectors arrays working at multiple frequencies in the range of a few MHz to 1GHz is extremely challenging [2.53]. FD is less sensitive than these other methods when the tissue thickness is several centimeters. FD methods are limited in their application in small animal imaging due to the small volumes which necessitates the modulation of the source for robust contrast in the phase function for high resolution reconstruction [2.73,2.75,2.80,2.82].

Time-domain imaging systems

The TD systems use short laser pulses in conjunction with time-resolved detection mechanisms [2.63,2.64,2.71,2.77]. These measurements are referred as the temporal point spread function (TPSF). A short laser pulse is injected into the tissue. While the pulse propagating through the tissue, the injected light pulse broadens and its peak intensity becomes smaller according to the tissue optical properties. The optical characteristics of the tissue can be reconstructed by evaluating the arrival and the decay time of the detected light pulse [2.75]. This method provides the most comprehensive data of all three imaging domains, as it allows acquiring the information contained in all frequencies simultaneously [2.62,2.71]. The TPSF measurement data can be easily converted by integration and Fourier transform of the TPSF to respectively generate the CW system data type and FD system data type [2.71,2.72,2.74,2.78]. However, the imaging

instrumentation is very complex and extremely expensive [2.12,2.62]. This technique is low signal-to-noise ratio (SNR) due to the time domain detection mechanism where only the photons arriving within a specific time window are collected. Thus, the measurements tend to have a long acquisition time. The measurement data is extremely sensitive to system noise and need a careful calibration of the system parameters [2.58]. In addition, the small tissue volumes such as small animals require an especially high temporal resolution, which poses added technological challenges [2.26].

2.3 Aims of the thesis

With a view toward the realization of 3D reconstruction from transillumination images of the animal body, this thesis will describe the development of a non-contact 3D optical tomography technique for small animal optical tomography using NIR transillumination images with completely absent of matching fluids.

The transillumination geometry was selected because the whole-body cannot be imaged due to the limited propagation of photons deep into the tissue in the case of high absorption and scattering by the epi-transillumination geometry. As the nature of transillumination imaging, the detection of the transmitted light through the entire volume provides more tomographic information than those obtained by epi-illumination imaging. In spite of lower spatial resolution than in FD and TD tomographic imaging and the difficulty to distinguish between the tissue's absorption and scattering properties, the CW imaging was selected based on its stability, the better noise characteristic, and the high sensitive detection capacity. In addition, this technique is relatively simple and low-cost imaging equipment. A CCD or CMOS camera can be used to obtain the transmitted light. The non-contact technique was selected to obtain the transillumination images over the full-angle (360^{o}) of the object as it is done with X-ray CT. It is possible to reconstruct 3D image using the common filtered back-projection [2.19,2.26].

Although it is known that light is strongly scattered in biological tissue and does not travel in a straight line between the source and the detector, the filtered back-projection in X-ray CT can be applied [2.19,2.26]. As the scattering is dominant, a

generalization of this approach is not to back-projected onto a line, but onto the entire volume, assuming that a spatially varying probability exists that a photon has passed a certain place within the tissue [2.19,2.26].

Under these considerations, the system shall be designed in this thesis to operate in the continuous-wave domain with transillumination geometry. The NIR light from a tunable pulsed laser (Ti:Sapphire) through a beam expander for homogeneous illumination will be used as the light source. The transillumination image shall be obtained using a cooled CMOS camera oriented toward the opposite face of the target model to the light-incident side. The illumination and the detection system (camera) shall be designed without any physical contact to the imaging object. The image can be obtained with the full-angle (360°) of the animal similar as it is done in X-ray CT.

For implementation of the 3D reconstruction using transillumination images of light-absorbing structure of the animal body, a new scattering suppression technique shall be developed to suppress the scattering effect in transillumination images by deconvolution with the PSF. This PSF has derived for the light source located in the medium by applying the diffusion approximation to the equation of transfer in previous studies of my research group [2.84]. The light distribution can be recovered clearly through an interstitial tissue by the deconvolution with appropriate PSF. Therefore, realization of the 3D imaging from the transillumination images can be expected if this light-source PSF can be applied to the transillumination image of light-absorbing structure. Once the scattering effect effectively suppressed, 3D image is available by using the common filtered back-projection technique with the improved transillumination images.

This concept essentially reduces the technical complexity of tomographic instrumentation and less experimental preparation as well as much less computational effort.

Chapter 3
Principles

This chapter describes the principles related to this study. In order to reconstruct 3D image from 2D image, the filtered back-projection will be introduced first. Then the derivation of depth-dependent point spread function by applying the diffusion approximation to the radiative transfer equation will be presented. Finally, the selection of deconvolution algorithm will be discussed.

3.1 Computed tomography image reconstruction [3.1–3.11]

The word tomography means a picture of a section or a slice. It refers to the process that generates a cross-sectional image of an object from a series of projections collected by scanning the object from many different directions. The discussion presented in this section pertains to the case of two-dimensional X-ray absorption tomography.

In this type of tomography, projections are obtained by a number of sensors that measure the intensity of X-rays travelling through a slice of the scanned object. One projection is taken for each rotational angle while rotating the radiation source and the sensor array around the object in small increments. The image reconstruction process uses these projections to calculate the average X-ray attenuation coefficient in cross-sections of a scanned slide. If different structures inside the object induce different levels of X-ray attenuation, they are discernible in the reconstructed image.

The most commonly used approach for image reconstruction from many projections is filtered back-projection (FBP). In this thesis, the focus discussion is on parallel-beam back-projection.

3.1.1 Line integrals and projections

A line integral represents the integral of some parameter of the object along a line. In

X-ray CT, the X-rays propagate through biological tissue and a line integral represents the total attenuation suffered by a beam of X-rays as it travels in a straight line through the object.

The intensity of an X-ray beam is dependent on the intensity of the source I_0, the absorption coefficient μ, and length l of the intervening tissue:

$$I(x,y) = I_0 \exp(-\mu l), \tag{3.1}$$

where $I(x,y)$ is the beam intensity (proportional to number of photons) at position (x,y). If the beam passes through tissue components having different absorption coefficients, then, assuming the tissue is divided into equal sections Δl, Eq. (3.1) becomes

$$I(x,y) = I_0 \exp(-\sum_i \mu(x,y)\Delta l). \tag{3.2}$$

The projection $p(x,y)$ is the log of the intensity ratio and is obtained by normalizing Eq. (3.2) by the beam intensity and taking the natural log:

$$p(x,y) = \ln\left[\frac{I_0}{I(x,y)}\right] = \sum_i \mu(x,y)\Delta l. \tag{3.3}$$

Equation 3.3 is also expressed as a continuous equation, where it becomes the line integral of the attenuation coefficients from the source to the detector:

$$p(x,y) = \int_{Source}^{Detector} \mu(x,y)dl. \tag{3.4}$$

The output of each beam at the angle θ with respects to the reference axis is just the projection of absorption characteristics of the intervening tissue, as defined in Eq. (3.4). The projections of the entire individual parallel beam constitute a projection profile of the intervening tissue absorption coefficients.

If the beam is at the angle θ with respects to the reference axis, then the equation for a line passing through the origin at the angle θ is

$$x\cos\theta + y\sin\theta = 0, \tag{3.5}$$

and the projection for that single line at a fixed angle P_θ becomes

$$P_\theta = \int_{-\infty}^{+\infty}\int_{-\infty}^{+\infty} f(x,y)(x\cos\theta + y\sin\theta)dxdy, \tag{3.6}$$

where $f(x,y)$ is the distribution of absorption coefficient, as defined in Eq. (3.2). If the beam is displaced a distance r from the axis in a direction perpendicular to θ, the equation for that path is

$$x\cos\theta + y\sin\theta - r = 0. \tag{3.7}$$

Using Eqs. (3.6) and (3.7) combined with the Dirac delta distribution δ to represent the discrete parallel beams, the equation describing the entire projection profile $P_\theta(r)$ becomes

$$P_\theta(r) = \int_{-\infty}^{+\infty}\int_{-\infty}^{+\infty} f(x,y)\delta(x\cos\theta + y\sin\theta - r)dxdy. \tag{3.8}$$

This equation is known as the Radon transform $\Re$ and can be written succinctly as

$$P_\theta(r) = \Re\left[f(xy)\right]. \tag{3.9}$$

Reconstructing the image from projection profiles is a classic inverse problem. The image should result from the application of an inverse Radon transform to the projection profiles as

$$f(x,y) = \Re^{-1}\left[P_\theta(r)\right]. \tag{3.10}$$

While the Radon transform and inverse Radon transform are expressed in terms of continuous variables, in imaging system the absorption coefficients are given in terms of discrete pixels and the integral in the above equation become summation.

Figure 3.1 illustrates the relationship between the measured views and the corresponding image. Each sample acquired in the X-ray CT system is equal to the sum of the image values along a ray pointing to that sample. For example, view 1 is found by adding all the pixels in each row. Likewise, view 3 is found by adding all the pixels in each column. The other views, such as view 2, sum the pixels along rays that are at an angle.

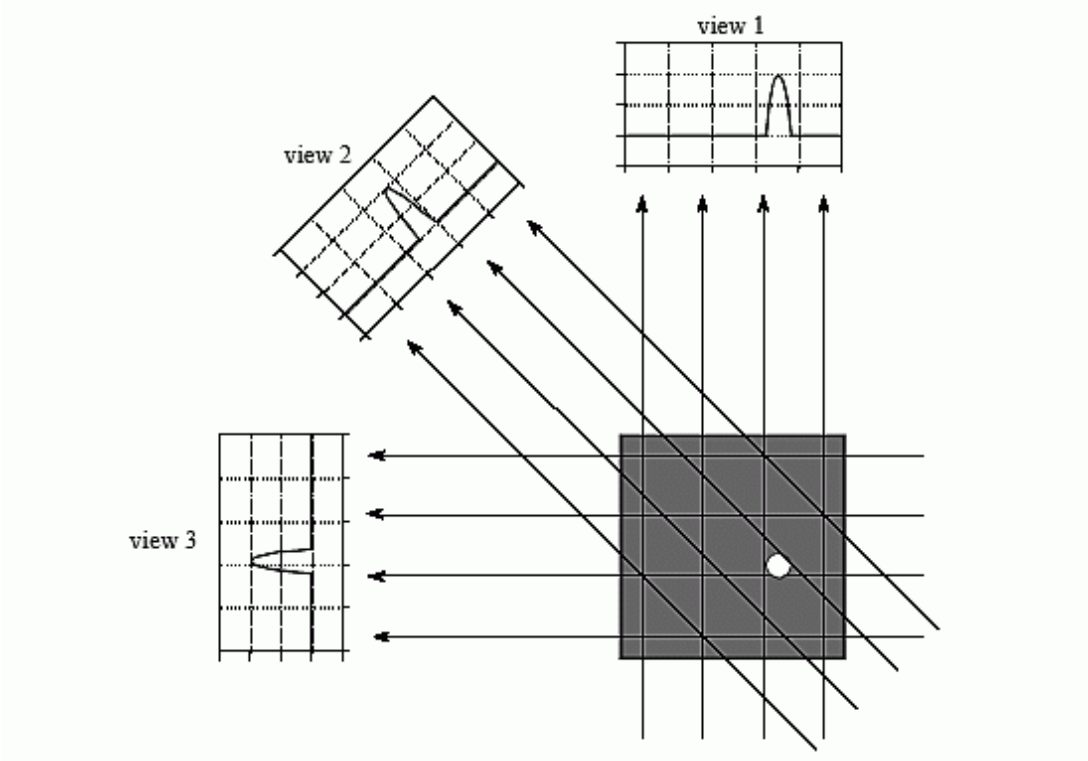

Fig. 3.1. X-ray CT views. Computed tomography acquires a set of views and then reconstructs the corresponding image. Each sample in a view is equal to the sum of the image values along the ray that points to that sample. In this example, the image is a small pillbox surrounded by zeroes. While only three views are shown here, a typical X-ray CT scan uses hundreds of views at slightly different angles. (Figure reprinted from [3.7]).

Figure 3.2 shows that simple back-projection is a common sense approach. An individual sample is back-projected by setting all the image pixels along the ray pointing to the sample to the same value. In less technical terms, a back-projection is formed by smearing each view back through the image in the direction it was originally acquired. The final back-projection image is obtained as the sum of all the back-projected views.

While this example of back-projection is conceptually simple, it does not correctly solve the problem. As shown in Fig. 3.2(b), a back-projection image is very blur. A single point in the true image is reconstructed as a circular region that decreases in intensity away from the center. In more formal terms, the point spread function of back-projection is circularly symmetric, and decreases as the reciprocal of its radius.

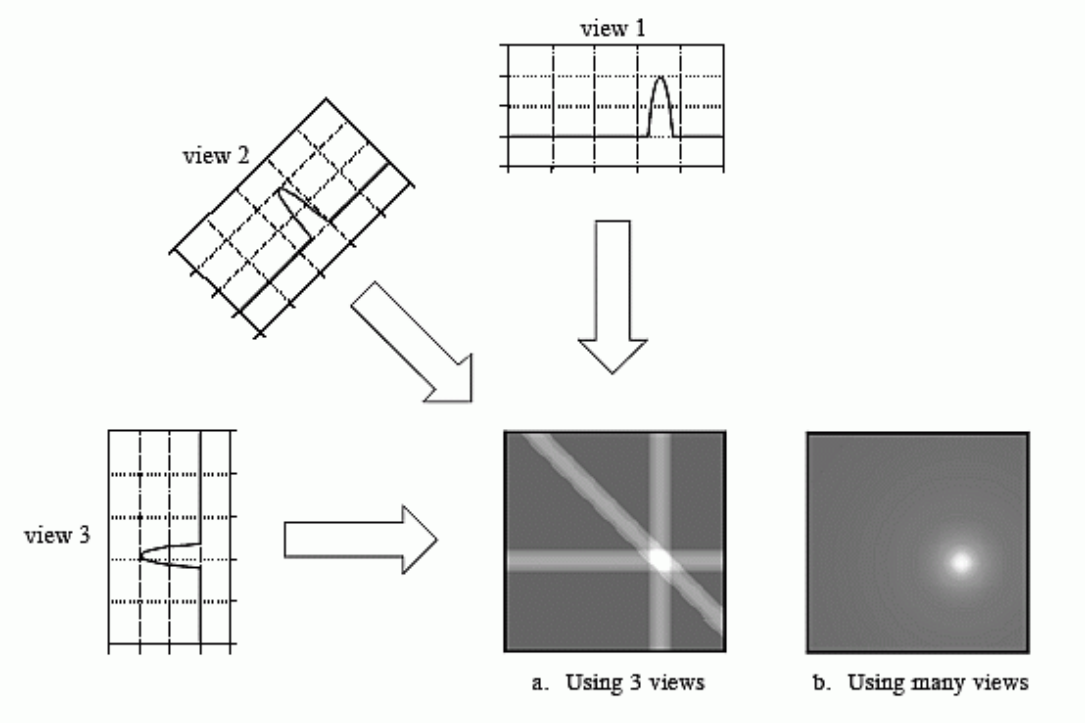

Fig. 3.2. Example of simple back-projection. Back-projection reconstructs an image by taking each view and smearing it along the path it was originally acquired. The resulting image is a blurry version of the correct image. (Figure reprinted from [3.7]).

3.1.2 The Fourier slice theorem

The Fourier slice theorem plays a fundamental role in image reconstruction since it relates the Fourier transform of the projections to the 2D Fourier transform of the object function. With given the projection data, it should be possible to estimate the object by simply performing a 2D inverse Fourier transform.

To derive the Fourier slice theorem, the 2D Fourier transform is defined as:

$$F(u,v) = \int_{-\infty}^{+\infty}\int_{-\infty}^{+\infty} f(x,y)\exp\left[-j2\pi(ux+vy)\right]dxdy, \tag{3.11}$$

where u,v are measured in cycles per unit length and the Fourier Transform of the projection data at any angle as

$$S_\theta(w) = \int_{-\infty}^{+\infty} P_\theta(r)\exp(-j2\pi wr)dr, \tag{3.12}$$

where w is the radians per unit length.

A new coordinate system (r,s) is defined by the rotation of the (x,y) system by the angle of rotation such that

$$\begin{bmatrix} r \\ s \end{bmatrix} = \begin{bmatrix} \cos\theta & \sin\theta \\ -\sin\theta & \cos\theta \end{bmatrix}\begin{bmatrix} x \\ y \end{bmatrix}. \tag{3.13}$$

In the (r,s) coordinate system, a projection would then be defined as

$$P_\theta(r) = \int_{-\infty}^{+\infty} f(r,s)ds, \tag{3.14}$$

From Eqs. (3.12) and (3.13), the projection becomes

$$S_\theta(w) = \int_{-\infty}^{+\infty}\left[\int_{-\infty}^{+\infty} f(r,s)\exp(-j2\pi wr)\right]dr. \tag{3.15}$$

This can be transformed into the (x,y) coordinate system using the result of Eq. (3.13) to get the following result:

$$S_\theta(w) = \int_{-\infty-\infty}^{+\infty+\infty} f(x,y)\exp(-j2\pi wr)dxdy, \tag{3.16}$$

$$r = x\cos\theta + y\sin\theta. \tag{3.17}$$

The right hand side of Eq. (3.16) represents the 2D Fourier transform of the $f(x,y)$ and left hand side is the 1D Fourier transform of the projections. Therefore, taking the 1D Fourier transform of the projections of an object at an angle θ is equivalent to obtaining the 2D Fourier transform of the $f(x,y)$ along the line r inclined at an angle θ. Therefore, if the projections are obtained at many angles, then this 2D Fourier transform of the projections at many such lines inclined at various angles can be obtained. If the number of angles is large enough, many lines of 2D Fourier transforms of the object will be obtained. With the inverse Fourier transform of all these lines, the $f(x,y)$ for all (x,y) in the object's cross-section can be reconstructed. That is,

$$f(x,y) = \int_{-\infty-\infty}^{+\infty+\infty} S_\theta(w)\exp\left[j2\pi(wx+wy)\right]dudv, \tag{3.18}$$

represents the back-projection along the line r,
where,

$$S_\theta(w) = F(w\cos\theta, w\sin\theta) = F(u,v). \tag{3.19}$$

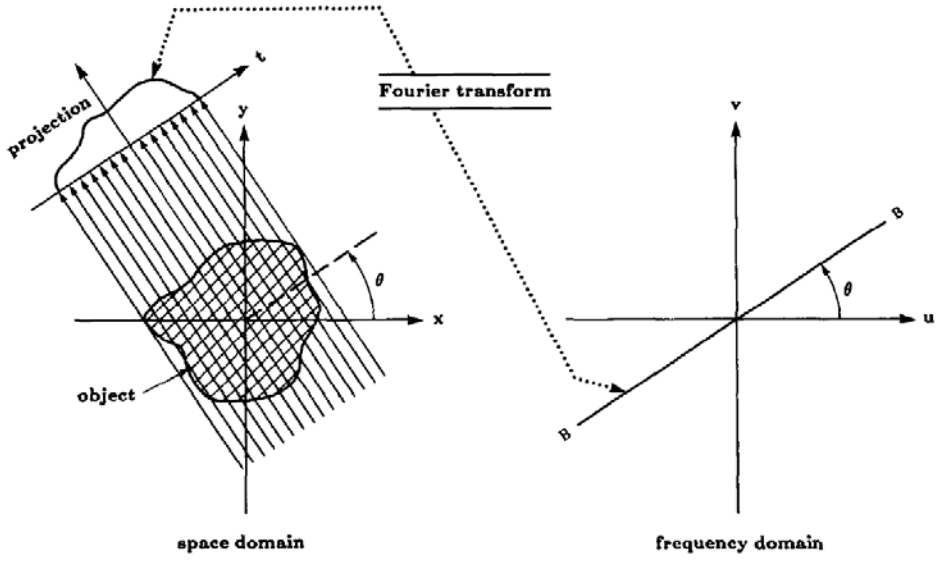

Fig. 3.3. The Fourier slice theorem relates the Fourier transform of a projection to the Fourier transform of the object along a radial line. (Figure reprinted from [3.5]).

The equation (3.19) is known as the Fourier slice theorem or the projection-slice theorem. It states that the Fourier transform of a parallel projection with orientation angle θ is a slice of the 2D Fourier transform of the region from which the projection was obtained. The reason of this terminology can be explained with the aid from Fig. 3.3. As this figure shows, the 1D Fourier transform of an arbitrary projection is obtained by extracting the values from $F(u,v)$ along a line oriented at the same angle as the angle used in generating the projection. In principle, the $f(x,y)$ could be obtained by simply obtaining the inverse Fourier transform of $F(u,v)$. In case of an infinite number of projections, the 2D frequency space of the $f(x,y)$ can be filled completely. A 2D inverse Fourier transform then yields the reconstructed $f(x,y)$.

In practice, only a finite number of projections of an object can be taken. In that case, it is clear that the function $F(u,v)$ is only known along a finite number of radial lines. In order to use inverse Finite Fourier transform, one must then interpolate from these radial points to the points on a square grid. This calculation involves solving a large set of simultaneous equations often leading to unstable solutions and requiring a sophisticated computation effort.

While this provides a simple conceptual model of tomography, practical implementations require a different approach. The FBP algorithm, will be derived in next section, is currently being used in almost all applications of straight ray tomography. Advantage of this method is that the difficult interpolation problem, which was encountered in the Fourier slice reconstruction method will be confined to a linear interpolation in the image domain.

3.1.3 Parallel-beam filtered back-projection

A reformulation of the Fourier slice theorem in polar coordinates yields a 2-step reconstruction method consisting of a projection filtering and a back-projection onto the image domain.

The coordinate system in the frequency domain (u,v), which is rectangular, changes to the polar coordinate system by making the following substitutions:

$$u = w\cos\theta, v = w\sin\theta, \tag{3.20}$$

where w is radius and θ is angle in radians and the differential change as

$$dudv = wdwd\theta, \tag{3.21}$$

$$f(x,y) = \int_0^{2\pi}\int_0^{\infty} F(w,\theta)\exp\left[j2\pi w\left(x\cos\theta + y\sin\theta\right)\right]wdwd\theta, \tag{3.22}$$

The above integral can be split by considering θ from 0 radians to π radians, and then from π radians to 2π radians:

$$\begin{aligned} f(x,y) = &\int_0^{\pi}\int_0^{\infty} F(w,\theta)\exp\left[j2\pi w\left(x\cos\theta + y\sin\theta\right)\right]wdwd\theta + \\ &\int_{\pi}^{2\pi}\int_0^{\infty} F(w,\theta+\pi)\exp\left\{j2\pi w\left[x\cos(\theta+\pi) + y\sin(\theta+\pi)\right]\right\}wdwd\theta, \end{aligned} \tag{3.23}$$

It is known from Fourier theory that

$$F(w,\theta+\pi) = F(-w,\theta). \tag{3.24}$$

Therefore, the Eq. (3.23) can be simplified as

$$f(x,y) = \int_0^{\pi}\int_{-\infty}^{+\infty}\{F(w,\theta)|w|\exp[j2\pi w(x\cos\theta + y\sin\theta)]dw\}d\theta. \tag{3.25}$$

From Eqs. (3.12) and (3.15), in this case, $F(w,\theta)$ inside the integral is the same as $S(\theta)$ of Eq. (3.15). Therefore,

$$f(x,y) = \int_0^{\pi}\left\{\int_{-\infty}^{+\infty}S_\theta(w)|w|\exp[j2\pi w(x\cos\theta + y\sin\theta)]dw\right\}d\theta. \tag{3.26}$$

In the Eq. (3.26), the term inside, which is indicated by the inner integral, represents a filtering operation and evaluate the filtered projections, and the operation being performed by the outer integral evaluate the back-projections, which basically represents a smearing of the filtered projections back onto the object and then finding the mean over all the angles.

The filtered back-projection algorithm can be thought of as a three step process below:

1. Finding the 1D Fourier transform of the projections.

2. Finding the filtered projections. It means multiplying the results of step 1 with a response function whose function looks as shown in Fig. 3.4 in the frequency domain and then finding the inverse Fourier transform. This step is essentially the same as carrying out convolution in the time domain. It can be represented mathematically as

$$Q_\theta(r) = \int_{-\infty}^{+\infty} S_\theta(w)|w|\exp(i2\pi wr)dw. \tag{3.27}$$

3. Finding the back-projections. This step is the smearing of the filtered projections back onto the object, and is mathematically represented by

$$f(x,y) = \int_0^\pi Q_\theta(x\cos\theta + y\sin\theta)d\theta. \tag{3.28}$$

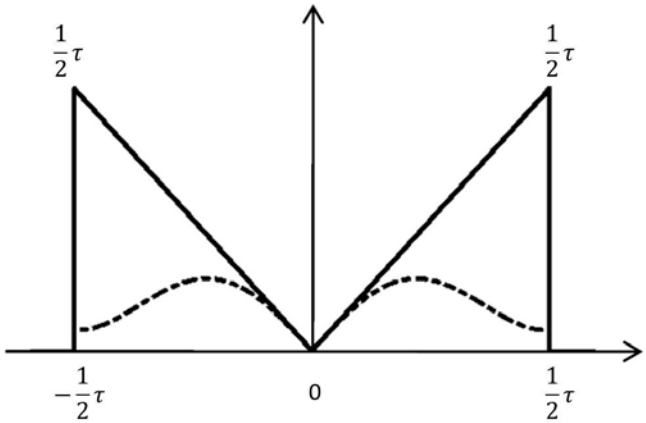

Fig. 3.4. The ideal filter response for filtered back-projection. Solid line: the Ram-Lak filter frequency response. Dashed line: resulting frequency response of the Ram-Lak filter multiplied by the Hamming function. (Figure adapted from [3.5,3.10]).

These three steps represent the filtered back-projection algorithm. In the discrete domain, the algorithm changes only slightly. The important steps are outlined below:

1. Find the 1D Fourier transform of the projections for each angle.

2. Multiply the result of step 1 with the response function in the frequency domain. In the actual example, the response function is simply a ramp with 45-degree slope and with the same length as the final reconstructed image. As shown in Fig. 3.4, the vertical magnitude of the function represents the distance between the rays.

3. Find the inverse Fourier transform of the results in step 2. This gives us the filtered projections in the discrete domain and correspond to $Q(n)$, where they are obtained at the various angles at which the projections were taken, and n is the ray number at which the line projection was taken.

4. Finding the back-projections. The integral of the continuous time system now becomes a summation:

$$f(x,y) = \sum_{i}^{K} Q_{\theta_i}(x\cos\theta_i + y\sin\theta_i), \tag{3.29}$$

where K is number of angles θ_i at which the projections were taken.

The derivations for Fourier slice theorem and the parallel-beam filtered-back-projection above are well noted by R. Rao and R. Kriz in [3.6].

It should be noted here that (x,y) are chosen by the program while back projecting. So the value of $x\cos\theta + y\sin\theta$ may not correspond exactly to a value of n for the filtered projections, which may have been calculated in the previous step. Therefore interpolation has to be done, and usually linear interpolation is quite sufficient [3.5].

The filtering procedure is basically a multiplication of the projections with the kernel in Fourier space. This high-pass filter compensates for the sampling density in the frequency space. For a discrete implementation the "Ram-Lak" filter or the ramp filter is cut off at the Nyquist frequency, as shown in Fig. 3.4. A smoothing window function such as the Hamming window is often used that suppresses the highest spatial frequencies, to reduce the high-frequency noise and aliasing artifacts in the reconstruction image.

In frequency domain, because the zero-frequency term, called as *dc term*, is proportional to the average value of $f(x,y)$, $|F(0,0)|$ has typically been the largest component of the spectrum by a factor that can be several orders of magnitude larger

than other terms. Because frequency component u and v are zero at the origin, $F(0,0)$ sometimes is called the *dc component* of the transform.

Finally, it is noted that, because the ramp filter (even when it is windowed) zeros the dc terms in the frequency domain, each back-projection image will have a zero average value. This means that each back-projection images will have negative and positive pixels. When all the back-projections are added to form the final image, some negative locations may become positive and the average value may not be zero, but typically, the final image will still have negative pixels.

There are several ways to handle this problem. The simplest approach, when there is no knowledge regarding what the average values should be, is to accept the fact that negative values are inherent in the approach and the scaled result using the procedure described below.

Given an image f, an approach that guarantees that the full range of an arithmetic operation between images is "captured" into a fixed number of bits is as follows. First, performing the operation

$$f_m = f - \min(f), \tag{3.30}$$

which creates an image whose minimum value is 0. Then, preforming the operation

$$f_s = K\left[f_m / \max(f_m)\right], \tag{3.31}$$

which creates a scaled image f_s, whose values are in the range $[0, K]$. When working with 8-bit images, setting $K=255$ gives us a scaled image whose intensities span the full 8-bit scale from 0 to 255. Similar comments apply to 16-bit images or higher.

When knowledge about what a "typical average value" should be is available, that value can be added to the filter in the frequency domain, thus offsetting the ramp and preventing zeroing the dc term. When working in the spatial domain with convolution,

the very act of truncating the length of the spatial filter (inverse Fourier transform of the ramp) prevents it from having a zero average value, thus avoiding the zeroing problem altogether.

As illustrated in Fig. 3.5, each view is filtered before the back-projection to counteract the blurring. That is, each of the one-dimensional views is convolved with a one-dimensional filter kernel to create a set of filtered views. These filtered views are then back-projected to provide the reconstructed image, a close approximation to the "correct" image. In fact, the image produced by filtered back-projection is identical to the "correct" image when there are an infinite number of views and an infinite number of points per view.

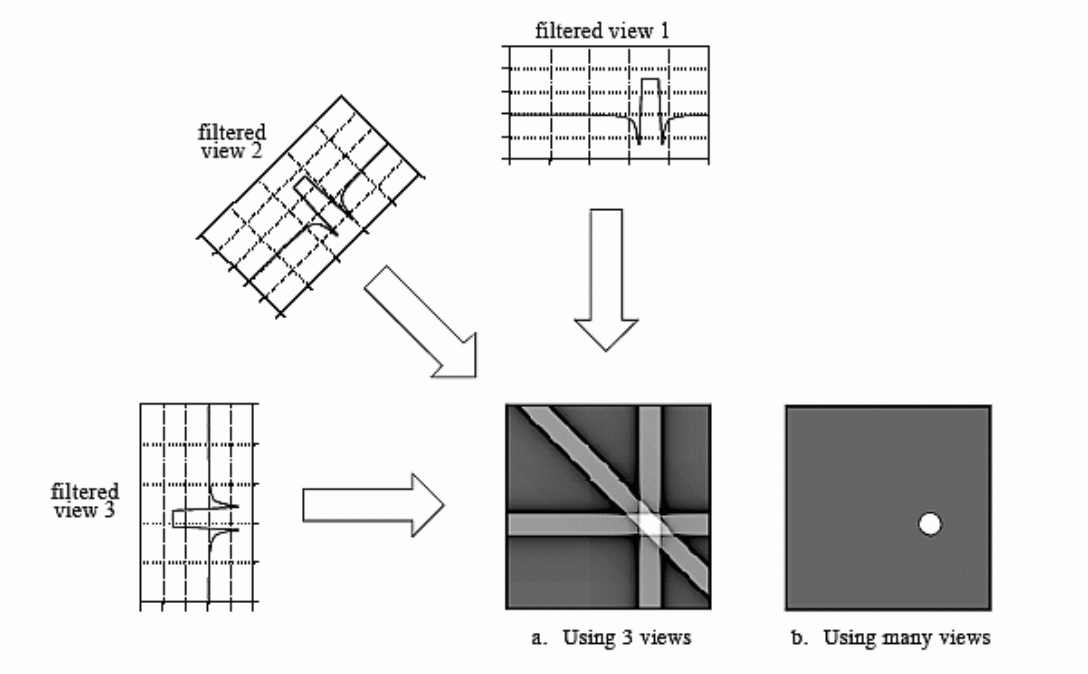

Fig. 3.5. Example of using filtered back-projection technique. Filtered back-projection is reconstructing an image by filtering each view before back-projection. This removes the blurring seen in the simple back-projection as shown in Fig. 3.2, and results in a mathematically exact reconstruction of the image. (Figure reprinted from [3.7])

3.2 Radiative transport equation and diffusion equation [3.12–3.24]

There are two distinct theories have been developed to deal with multiple-scattering problems as noted by A. Ishimaru [3.14,3.18]. One is called the analytical theory or multiple-scattering theory and is based on Maxwell's equations; the other is the radiative transport theory. The analytical theory is mathematically rigorous since, in principle, one can account for all the effects of multiple scattering, diffraction, and interference. However, it has not yet produced practical models of general use to describe multiple-scattering problems.

The radiative transfer equation (RTE) is a phenomenological and a heuristic theory describing the transport of energy through a scattering medium that lacks a rigorous mathematical formulation able to account all the physical effects involved in light propagation. This theory only considers transport of power and wave phenomenon like polarization, interference and diffraction are neglected. Despite the fact that the RTE has been derived under certain simplifying assumptions, it led to useful models for many practical problems.

3.2.1 The radiative transfer equation

In transport theory the light is considered to be a collection of independently moving classical particles – photons, which do not interact with each other. The derivation presented in this section is well noted by A. Ishimaru *et al.* in [3.14,3.18] and K. Shimizu *et al.* in [3.22].

The basic quantity used in transport theory to describe energy propagation are defined starting from the spectral radiance or spectral specific intensity $I_s(\bar{r},\hat{s},t,\nu)$. It has a unit of $Wm^{-2}sr^{-1}Hz^{-1}$, and is defined as the average power that at position $\bar{r}$ and time t flows through the unit area oriented in the direction of the unit vector $\hat{s}$, due to photons within a unit frequency band centered at ν, moving within the unit solid angle around $\hat{s}$.

The media, which will be discussed in this thesis, refer to the one in which the frequency of the radiation does not change during propagation, and then the term radiance or specific intensity $I_s(\bar{r},\hat{s})$ ($Wm^{-2}sr^{-1}$) defined as the integral of $I_s(\bar{r},\hat{s},t,v)$ over a narrow range of frequency within a unit frequency interval. The amount of power dP flows within the solid angle dw through the elementary area da (oriented along the direction $\hat{s}_0$) placed at $\bar{r}$ in the frequency interval $(v, v+dv)$ is given by

$$dP = I_s(\bar{r},\hat{s})\cos\theta da dw dv, \tag{3.32}$$

where $\hat{s}\cdot\hat{s}_0 = \cos\theta$ as shown in Fig. 3.6.

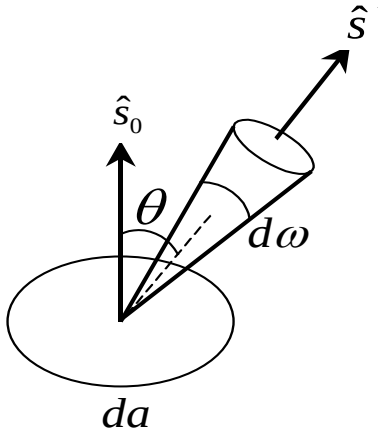

Fig. 3.6. Specific intensity and the power dP given in Eq. (3.32). (Figure adapted from [3.13]).

The flux-density vector $\overline{F}(\bar{r})$ represents the amount and the direction of the net flow of power and is given by

$$\overline{F}(\bar{r}) = \int_{4\pi} I(\bar{r},\hat{s})\hat{s}dw, \tag{3.33}$$

where the integration is taken over a complete solid angle 4π. When the flux is incident on a surface, this is called the irradiance.

The energy density $u(\bar{r})$ ($Wsm^{-3}Hz$) in a unit frequency interval is given by

$$u(\bar{r}) = \frac{1}{c}\int_{4\pi} I(\bar{r},\hat{s})dw, \tag{3.34}$$

where c is the velocity of wave propagation.

Sometimes, it is convenient to use the average intensity $U(\bar{r})$ defined by

$$U(\bar{r}) = \frac{1}{4\pi}\int_{4\pi} I(\bar{r},\hat{s})dw. \tag{3.35}$$

The average intensity does not in general represent the power flow, but it is proportional to the energy density.

The particles scatter and absorb the wave energy, and these characteristics should be included in a differential equation to be satisfied by the specific intensity. This equation is called the radiative transfer equation in radiative transfer theory. It is identical to, the Boltzmann equation used in neutron transport theory.

In consideration that a specific intensity $I_s(\bar{r},\hat{s})$ incident upon a cylindrical elementary volume with a unit cross section and length ds. The volume ds contains ρds particles where ρ is the number of particles in unit volume and is called the number density. Each particle absorbs the power $\sigma_a I$ and scatters the power $\sigma_s I$, and therefore, the decrease of the specific intensity $dI(\bar{r},\hat{s})$ for the volume ds is expressed as $(-\rho ds\sigma_t I)$.

At the same time the specific intensity increase because a portion of the specific intensity $I(\bar{r},\hat{s}')$ incident on this volume from another direction $\hat{s}'$ is scattered into the direction $\hat{s}$ and should be added to the intensity $I(\bar{r},\hat{s})$.

The specific intensity also may increase due to the emission from within the volume ds. Denoting by $\varepsilon(\bar{r},\hat{s})$ the power radiation per unit volume per unit solid angle in the direction $\hat{s}$, the increase of the specific intensity is given by $ds\varepsilon(\bar{r},\hat{s})$.

Finally, the radiative transfer equation is expressed by

$$\frac{\partial}{\partial s} I(\bar{r},\hat{s}) = -\rho\sigma_t I(\bar{r},\hat{s}) + \frac{\rho\sigma_t}{4\pi}\int_{4\pi} p(\hat{s},\hat{s}') I(\bar{r},\bar{s}') d\omega' + \varepsilon(\bar{r},\hat{s}), \tag{3.36}$$

where the phase function $p(\hat{s},\hat{s}')$ is a function of the difference $\hat{s} - \hat{s}'$, and $\sigma_t = \sigma_a + \sigma_s$ is a total scattering cross section.

The first term in the right hand side of Eq. (3.36) describes the intensity decays of the light, that propagated in the direction $\hat{s}$, is affected by the absorption and scattering. The second term describes the specific intensity increase because a portion of the specific intensity $I(\bar{r},\hat{s}')$ incident on this volume from another direction $\hat{s}'$ is scattered into the direction $\hat{s}$. The third term is the intensity increase due to the emission from within the volume ds. In the case generally, by considering that the scattering is dominated in the biological tissue, and there is nothing that could be the source in the body except in special cases such as fluorescent, the third item could be ignored.

The RTE has no analytical solution in three dimensions. Under certain assumptions the RTE can be reduced to a diffusion-type equation, which is mathematically less complex. The diffusion approximation does not yield a full solution since it is an approximation. The basic idea is to expand the RTE into spherical harmonics.

If the following assumptions are made:

1. scatter is the dominant interaction: $\mu_s' >> \mu_a$,
2. phase function $p(\hat{s},\hat{s}')$ is independent of the absolute angle,
3. photon flux $\bar{F}(\bar{r})$ changes slowly $d\bar{F}(\bar{r})/dt = 0$,
4. all sources are isotropic, the result is the time-dependent diffusion equation:

$$\frac{1}{c}\frac{\partial}{\partial t}\phi(\bar{r},t) - D\nabla^2\phi(\bar{r},t) + \mu_a\phi(\bar{r},t) = S(\bar{r},t), \tag{3.37}$$

where D, c, ϕ, and S are respectively stand for the diffusion coefficient, the speed of light in the medium, the light fluence rate, and the light source.

The diffusion coefficient is defined as

$$D = \frac{1}{3[\mu_a + (1-g)\mu_s]} = \frac{1}{3(\mu_a + \mu_s')}. \tag{3.38}$$

The depth-dependent point spread function (PSF) for describing the scattering effect of light source located in the scattering medium will be derived by using the diffusion approximation in next section.

3.2.2 Depth-dependent point spread function for transcutaneous imaging

Figure 3.7 shows the principle of transcutaneous fluorescent imaging. The excitation light was illuminated from outside to an object located inside the body. The fluorescent light is excited in the body and is transmitted through the surface tissue. The wavelength of the fluorescent light is generally different from that of the excitation light. Therefore, the scattered light at the surface can be eliminated with an optical filter. In this way, transcutaneous fluorescent imaging can be attained using reflection measurement geometry.

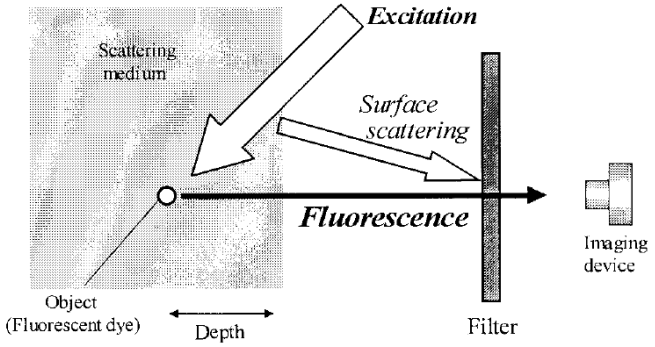

Fig. 3.7. Principle of transcutaneous fluorescent imaging. (Figure reprinted from [3.22]).

Images obtained through transcutaneous imaging are blurred because of the light

scattering by tissue between the fluorescent source and the skin surface. Even with this blurred image, the existence of the fluorescent source and its crude localization can be recognized. However, better spatial resolution is crucial required to distinguish organs or to understand the shape of the fluorescent distribution.

Degraded images obtained by camera can be described using the following equation

$$y = h \times x + n, \tag{3.39}$$

where y, h, x, and n are respectively stand for the original image, the degraded point spread function, the original image, and the noise component of the measurement system. $\times$ denotes the convolution operation.

The scattering effect can be suppressed by deconvolving the blurred image with the PSF if the degree of blurring as a PSF was known. The PSF can be obtained in the measurement, but it is not easy to measure all PSFs for every possible condition. Therefore, the PSF must be derived theoretically.

In biological tissue, the diffusion approximation can be applied to solve the RTE since the dominant effect is the scattering in comparison with the absorption. The specific intensity is given by

$$I_d(\bar{r}, \hat{s}) = U_d(\bar{r}) + \frac{3}{4\pi} \bar{F}_d(\bar{r}) \hat{s}, \tag{3.40}$$

where $U_d(\bar{r})$ and $\bar{F}_d(\bar{r})$ are respectively stand for the average intensity and the flux.

Figure 3.8 illustrates the geometry of the theoretical model. A point light source is placed at the origin of the circularly symmetrical cylindrical coordinate system (ρ, z). The scattering medium fills the half space $(z \le d)$. The PSF is defined as the spatial distribution of light intensity at the surface of the scattering medium $(z = d)$. In this derivation the scattering medium is assumed as homogenous. The point source radiating total power P_0 uniformly in all directions is expressed as

$$\varepsilon(\bar{r}) = \frac{P_0}{4\pi}\delta(\bar{r}), \tag{3.41}$$

where $\bar{r}$ is the position vector.

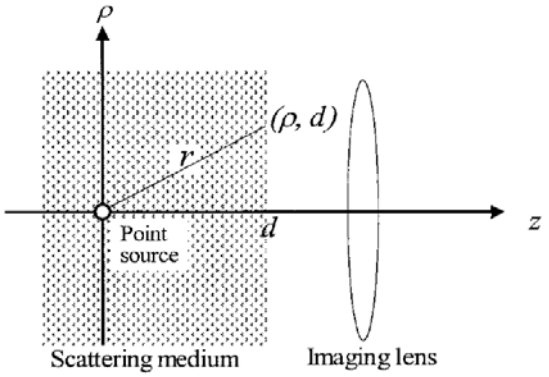

Fig. 3.8. Geometry of the theoretical model. (Figure reprinted from [3.22]).

The light intensity at the surface can be divided into two parts. They are the direct light component attenuated by the scattering and the absorption of the scattering medium, and the diffuse light component. The flux of the reduced direct light is given as

$$\bar{F}_n\bar{r} = P_0\frac{\exp\left[-(\mu_s+\mu_a)r\right]}{4\pi r^2}\hat{r}, \tag{3.42}$$

where μ_s, μ_a, and $\hat{r}$ are the scattering coefficient, the absorption coefficient, and the unit vector in the direction of $\bar{r}$, respectively. The scattering coefficient of surface tissue is typically in range 15–30 mm^{-1} in the near-infrared wavelength. Therefore this component reduces rapidly in the practical range of the distance from the source to the surface ($r > 0.2$ mm).

The diffuse component is obtained by applying the diffusion approximation to the RTE. The diffusion equation for the point source located in the scattering medium is

$$\nabla^2 U_d(\bar{r}) - {\kappa_d}^2 U_d(\bar{r}) = -\frac{3}{4\pi} P_0(\mu_s' + \mu_a)\delta(\bar{r}), \tag{3.43}$$

where ${\kappa_d}^2 = 3\mu_a(\mu_s' + \mu_a)$ and $\mu_s' = (1-g)\mu_s$. $U_d(\bar{r})$, μ_s', μ_a, and g are the average diffuse intensity, the reduced scattering coefficient, the absorption coefficient, and the scattering anisotropy, respectively. Solving this equation, $U_d(\bar{r})$ and the diffuse flux $\overline{F}_d(\bar{r})$ are given as

$$U_d(\bar{r}) = \frac{3P_0}{(4\pi)^2}(\mu_s' + \mu_a)\frac{\exp(-\kappa_d r)}{r}, \tag{3.44}$$

$$\overline{F}_d(\bar{r}) = \frac{P_0}{4\pi}\left(\kappa_d + \frac{1}{r}\right)\frac{\exp(-\kappa_d r)}{r}\hat{r}. \tag{3.45}$$

Using these results, the point spread function is obtained by

$$PSF(\rho) = \frac{3P_0}{(4\pi)^2}\left\{(\mu_s' + \mu_a) + \left[\kappa_d + \frac{1}{(\rho^2 + d^2)^{1/2}}\right]\frac{d}{(\rho^2 + d^2)^{1/2}}\right\}\frac{\exp\left[-\kappa_d(\rho^2 + d^2)^{1/2}\right]}{(\rho^2 + d^2)^{1/2}}, \tag{3.46}$$

where ρ and d are respectively stand for the radial distance from the z axis and the depth of the point source from the surface of the scattering medium. $\hat{r}\cdot\hat{s} = d/(\rho^2 + d^2)^{\frac{1}{2}}$.

Diffusion approximation is valid when the thickness of the scattering medium is much greater than the average mean-free-path length or $1/\mu_s'$. Thus Eq. (3.46) should be applied carefully when $(\rho^2 + d^2)^{\frac{1}{2}}$ is not much larger than $1/\mu_s'$.

In previous study of my research group, this theoretical PSF was validated and confirmed in good agreement with the measured PSF in experiment [3.22]. Figure 3.9

shows the result of the comparison of these two PSFs in terms of full-width-at-half-maximum (FWHM) of the spread. At the same depth d, both PSFs were in good agreement.

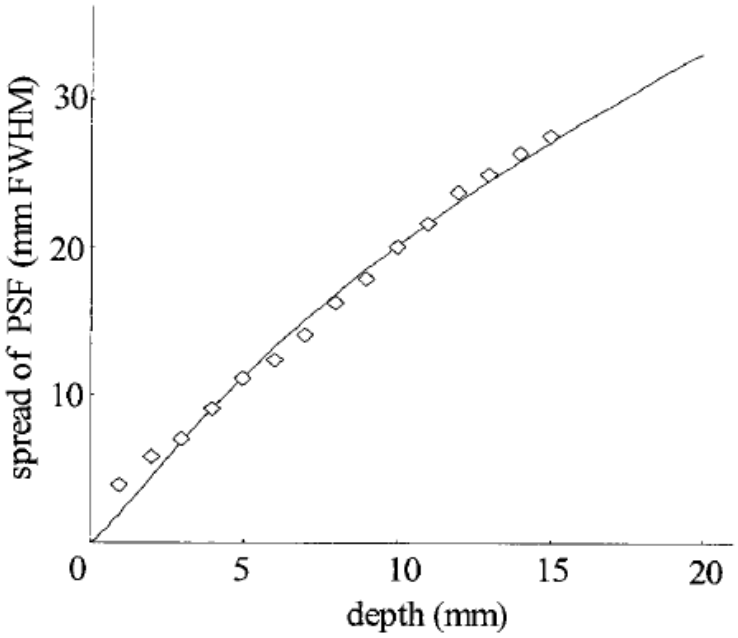

Fig. 3.9. Depth dependence of measured PSF spread. Diamonds and curve are the measurement and the theoretical calculation, respectively. (Figure reprinted from [3.22]).

The scattering effect can be effectively suppressed using this theoretical PSF. Figure 3.10 shows an example with transcutaneous fluorescence animal imaging that was conducted in previous study [3.22]. Figure 3.10(a) shows the observed image of a rat that was injected with ICG by intravenous injection. The observed image blurred due to the strong scattering effect in the tissue. Figure 3.10(c) shows the restored image. The scattering effect could be efficiently suppressed by performing deconvolution using the depth dependent PSF as shown in Fig. 3.10(b).

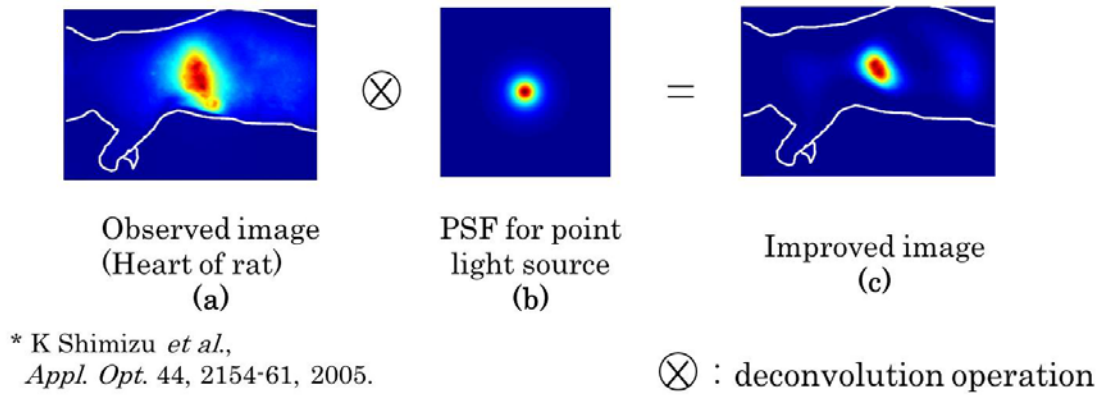

Fig. 3.10. Example of the improvement of transcutaneous fluorescence image using depth-dependent PSF: (a) observed image, (b) depth-dependent PSF, (c) improved image. ⊗ denotes the deconvolution operation. (Figure adapted from [3.22]).

In this study, this PSF will be applied to the transillumination image of light-absrobing structure. The applicability to a transillumination image of light-absorbing structure will be described in chapter 4. In the next section, the deconvolution method will be introduced.

3.3 Lucy-Richardson deconvolution [3.25–3.36]

In this section, the image formation model for fluorescence imaging or transillumination imaging will be presented first. Then the deconvolution algorithm will be discussed.

3.3.1 Photon noise and image formation model

As mentioned in previous section, images obtained by camera are described by combining a PSF convolution and noise degradation on a perfect un-degraded image as in Eq. (3.39). In fluorescence imaging and also transillumination imaging, the noises are always present in the observed image since the image was obtained by camera or camera accompanied with other devices. The most dominant contributor is the photon noise, also known as Poisson noise. Due to the nature of the measurement of light, the

photon counted process behaves as a Poisson process whose variance is equal to the mean of counted photons. The independence of random individual photon arrivals leads to photon noise not only in the case using digital sensors but also in the case using film-based sensor. The Poisson noise has no parameters to be calibrated, and is independent of other noise sources.

Assuming that the noise is of Poisson nature in fluorescence imaging and transillumination imaging, Eq. (3.39) can be re-written as

$$y = \wp(h \times x + n), \tag{3.47}$$

where y, $\wp$, h, x, and n are respectively stand for the observed image, the Poisson noise, the point spread function, the original image, and the background noise. $\times$ denotes convolution operation. This model is under the assumption of a translation invariant PSF, incoherent imaging and monochromatic light (excitation and emission). The fluorescence imaging and the transillumination imaging are the low-photon imagery technique; therefore the noise obeys a Poisson multiplicative law.

As a first approximation in the model, I omit the background noise component. It is well noted by Dey in [3.31] that there is no improvement on the result of accounting the background noise.

Therefore, the image formation model becomes

$$y = \wp(h \times x). \tag{3.48}$$

The distribution of y at the point p, $y(p)$, knowing $(h \times x)(p)$, is a Poisson distribution of the parameter $(h \times x)(p)$:

$$P(y(p) \mid (h \times x)(p)) = \frac{\left[(h \times x)(p)\right]^{y(p)} \exp\left[-(h \times x)(p)\right]}{y(p)!}. \tag{3.49}$$

Assuming that the noise is spatially uncorrelated, the statistics of the observed

image y, knowing the object x, and the PSF h that considered here as a parameter, is the likelihood distribution given by:

$$P(y \mid x) = \prod_{p \in S} \left(\frac{[(h \times x)(p)]^{y(p)} \exp[-(h \times x)(p)]}{y(p)!} \right), \tag{3.50}$$

where p is the coordinate of a pixel (or a 3D voxel) and S is the total set of pixel coordinates in the image (or the imaged volume).

It is suited for use with the Lucy-Richardson deconvolution algorithm that will be introduced in next section.

3.3.2 Lucy-Richardson deconvolution

Deconvolution is a mathematical operation used in image restoration to recover an image that is degraded by blurring and noise. Many deconvolution algorithms have been proposed. They can be divided into two categories: non-iterative (linear) and iterative (nonlinear). Direct inverse filtering, Weiner filtering, constrained least square (regularized) filtering are these simplest non-iterative algorithms for restoring images. These methods usually do not provide optimal image quality and acceptably restored images for fluorescence images and transillumination images. The non-iterative algorithms amplify noise, which is always present, and alter signal amplitudes. In addition, other limitations still have such as the Wiener filtering assumes known signal-to-noise ratio for every frequency. Even though signal-to-noise ratio was assumed uniform, it is typically unknown.

For these reasons non-iterative are replaced by nonlinear iterative deconvolution algorithms. Nowadays, nonlinear iterative techniques become powerful restoration tools that often yield results superior to those obtained with linear non-iterative methods. In this study, the Lucy-Richardson iterative algorithm was selected because this technique was optimized for Poisson distributed data.

This algorithm owns some positive properties such as it can function well in the

event of noise existence, prior information about the original image is not required and the repetition (iterative) feature.

The Lucy-Richardson algorithm finds x from the observed image y, knowing the PSF h, by maximizing the likelihood distribution (Eq. (3.50)) with respect to x base on a Bayesian framework. The likelihood probability Eq. (3.50) is maximized by minimizing the negative log likelihood. Thus it is enough to minimize the functional $J(x)$ defined as

$$J(x) = \int_p (h \times x)(p) - y(p) \log\left[(h \times x)(p)\right] dp. \tag{3.51}$$

As a result the following iteration procedure is derived:

$$\hat{x}^{n+1}(p) = \hat{x}^n(p) \underbrace{\left(h(-p) \times \frac{y}{h \times \hat{x}^n} \right)(p)}_{correction}, \tag{3.52}$$

where $\hat{x}^{n+1}$ is the new estimate from a previous estimate $\hat{x}^n$ at iteration n whereby $\hat{x}^0 = y$ and $h(-p)$ is the adjoint of h. Thus, each iteration step n the former estimate of the original $\hat{x}$ is multiplied by the correction factor.

The Lucy-Richardson has been never negative as long as the initial estimate was not negative. For noisy images, the Lucy-Richardson algorithm amplifies the noise and it does not always converge to a suitable solution in the presence of noise. When $n \to +\infty$ the result will only comprise of noise.

The algorithm converges slowly to the optimal solution and then diverges again. As with most nonlinear method, the question of when to stop the Lucy-Richardson algorithm is difficult to answer in general. The approach often followed is to observe the output and stop the algorithm when a result acceptable in a given application has been obtained. In practical, the stop criterion can either be a fixed number of iteration steps or the difference between two estimates $\hat{x}^{n+1}$ and $\hat{x}^n$.

Chapter 4
Application of light source PSF to transillumination images

It would be able to realize the 3D reconstruction image of light-absorbing structure from transillumination image if the scattering effect can be suppressed. In this chapter, a novel the scattering suppression technique in transillumination image using the light-source point spread function will be described. The theory of the proposed technique will be introduced first. Then the applicability and the effectiveness of the proposed technique will be examined in simulation and experiments.

4.1 Theory of proposed technique

For scattering suppression, the deconvolution technique using the point spread function (PSF) for fluorescence transcutaneous images is effective as mentioned in previous chapter. This PSF have derived for the fluorescence light source located in a slab scattering medium by applying the diffusion approximation to the radiative transfer equation [4.1]. With the known depth of the light source in a diffuse medium, the fluorescent distribution can be recovered clearly through an interstitial tissue by the deconvolution with this PSF. Therefore, the 3D imaging from the transillumination images could be expected to realize if this light-source PSF could be applied to the transillumination images of light-absorbing structure. The theory of proposed technique will be described in this section.

In transillumination imaging of light-absorbing structure, the homogeneous light is irradiated from outside the scattering medium. The scattered light goes through the absorbing structure and projects the shadow on the surface of the scattering object as shown in Fig. 4.1(b).

Figure 4.1 shows a schematic diagram of the observed light intensity distribution at

the scattering medium surface. In Fig. 4.1(a), the point source located in scattering medium while its location was replaced by an light-absorbing object in the Fig 4.1(b). As shown in Fig. 4.1, the scattering medium was considered as an infinite-wide slab, the dashed lines show the light distributions in infinity.

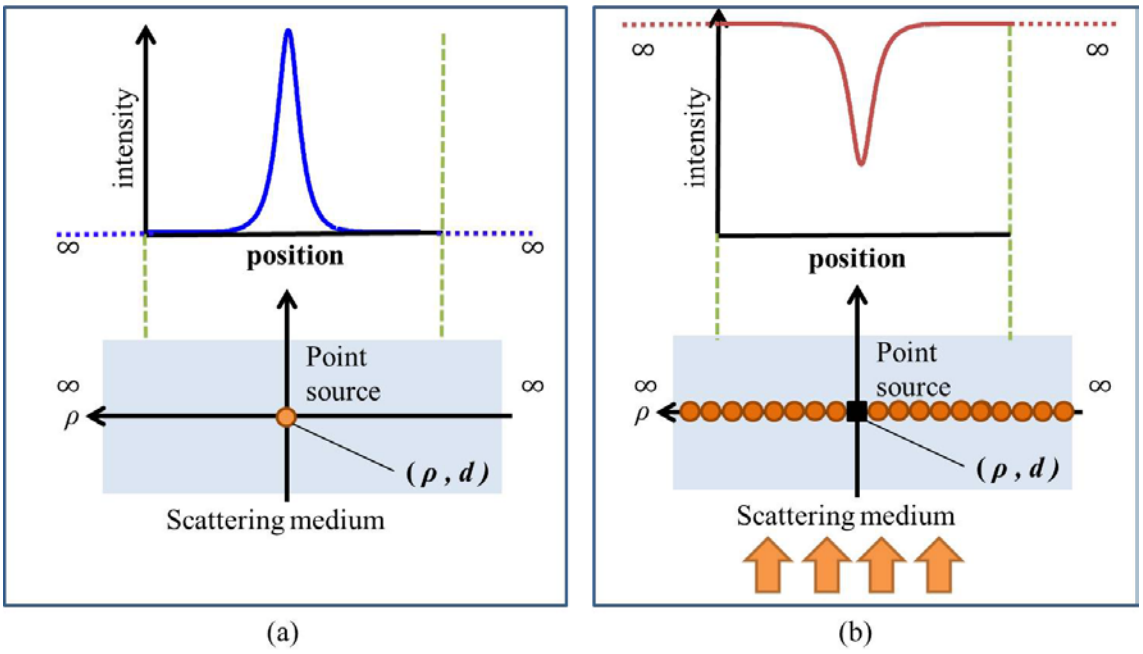

Fig. 4.1. Geometry for PSF as light distribution observed at the scattering medium surface: (a) for fluorescence transcutaneous imaging, (b) for transillumination imaging. The orange circle denotes the light point sources in both cases.

The light-absorbing object (absorber) can be considered as a collection of light-missing points if the light is diffused well at the depth of the absorber. Then the light-absorbing image observed at the surface is the collection of the spread light-missing distributions which are the PSFs obtained by Eq. (3.46). The PSF from Eq. (3.46) can be applied to the transillumination image of light-absorbing structure if this assumption is correct.

This process can be written as

$$x = y \otimes h, \tag{4.1}$$

where x, y, and h are respectively stand for the original image, the observed image, and the light-source PSF. $\otimes$ denotes the deconvolution operation.

In reality, due to limitation of the observed image, the light distribution was cut out as shown in Fig. 4.2. In fluorescence transcutaneous imaging, the light distribution was same as in infinity case. However, in transillumination imaging, the light distribution was cut out and dropped as shown by the orange dashed lines in Fig. 4.2(b). It is no longer correct as in infinity case. Thus, if the PSF, which was originally derived for a light source, cannot be applied directly to the transillumination images using deconvolution process.

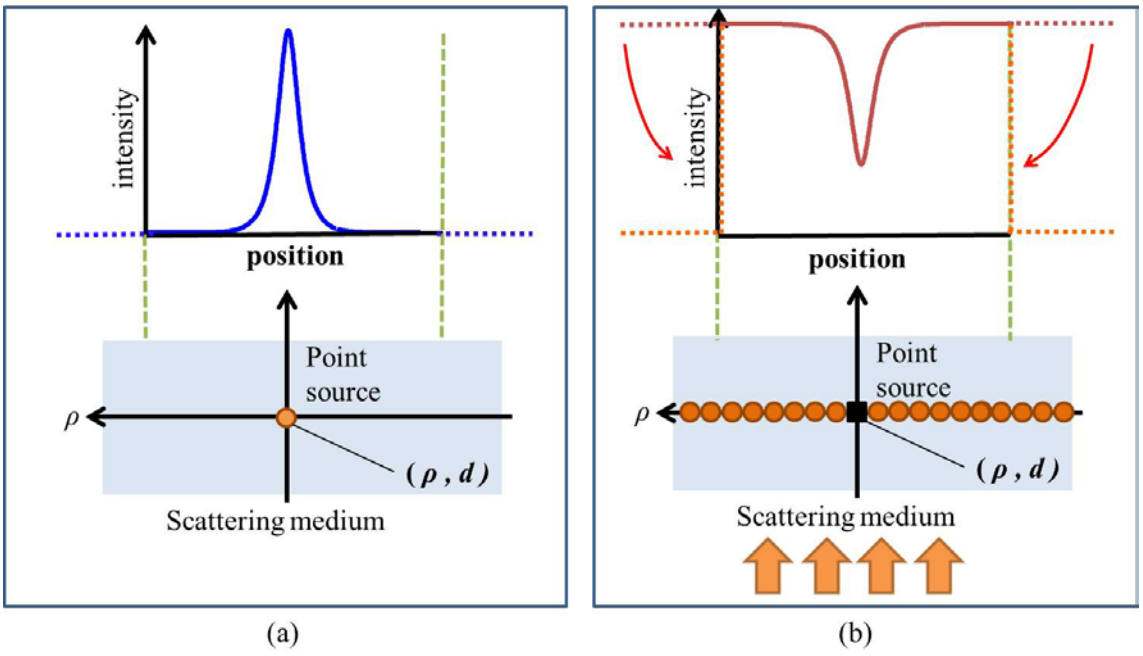

Fig. 4.2. Geometry for PSF as light distribution observed at the scattering medium surface in reality: (a) for fluorescence transcutaneous imaging, (b) for transillumination imaging. The orange circle denotes the light point sources in both cases.

To overcome this problem, the light distribution in the observed transillumination image will be inverted. The light distribution in the observed image becomes the

absorption distribution in the inverted image. Then the light-source PSF can be expected to apply correctly on the inverted transillumination image.

Therefore, the scattering suppression process in transillumination images by deconvolving with a light-source can be written as

$$x = y \otimes h = 1 - \left[(1 - y) \otimes h \right], \tag{4.2}$$

where x, y, and h are respectively stand for the original image, the observed image, and the light-source PSF. In this process, the observed image y were normalized to be from 0 to 1 using the same process as mentioned with Eqs. (3.30) and (3.31). $\otimes$ denotes the deconvolution operation. The applicability of light-source PSF to transillumination image was assessed in experiments, which are described in the next sections. Figure 4.3 shows a procedure of the proposed technique for transillumination image. The effectiveness of this proposed technique will be discussed in sections 4.3, 4.4, and 4.5.

It is noted that the width of light-source PSF becomes larger, when the depth from the scattering medium to the light source is increased. Then, the deconvolution with Lucy-Richardson algorithm requires much iterative calculation and result tends to be unstable. To overcome this difficulty, a technique was devised to divide the light-source PSF in Eq. (3.46) into n pieces, i.e.

$$PSF(\rho) = PSF_{part}(\rho) \times PSF_{part}(\rho) \times \ldots \times PSF_{part}(\rho), \tag{4.3}$$

in which is given by

$$PSF_{part}(\rho) = F^{-1}\left\{ \sqrt[n]{F\left[PSF(\rho) \right]} \right\}, \tag{4.4}$$

where F denotes Fourier transform. $\times$ denotes the convolution operation.

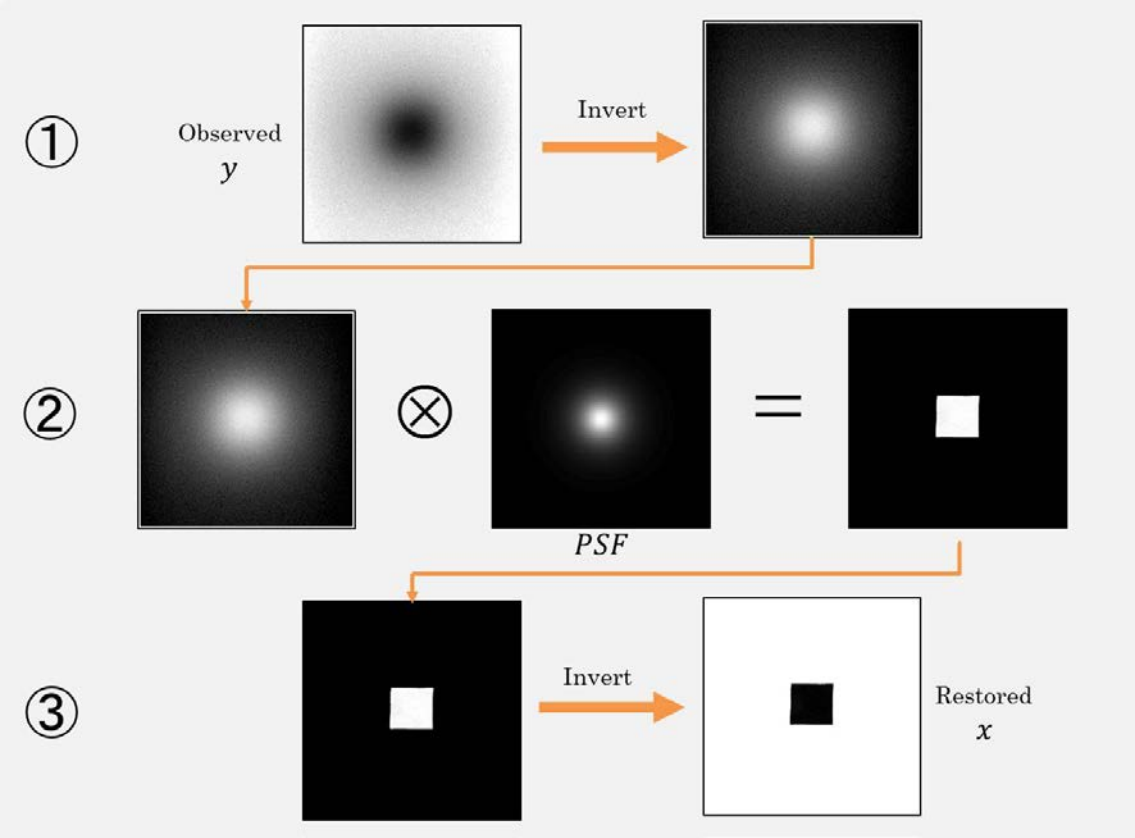

Fig. 4.3. Procedure of proposed technique for transillumination image using light-source PSF. ⊗ denotes the deconvolution operation.

In this way, the n times deconvolution with the partial $PSF_{part}(\rho)$ becomes equivalent to the one time deconvolution with $PSF(\rho)$. As the division number n increases, the width of $PSF(\rho)$ becomes less, and the deconvolution process becomes stable. However, the division number n should not be too large and n =3 was empirically optimized.

In this thesis, the deconvolution operation will be performed by that way. The effectiveness of this technique will be discussed in section 4.5.

The effectiveness of the light-source PSF from Eq. (3.46) to suppress the scattering effect in a transillumination image of the absorbing structure was examined in simulation and experiment. The results will be presented in the next sections. In the

deconvolution process, the Lucy–Richardson algorithm with iteration number up to 10 was used.

4.2 Applicability of light-source PSF to transillumination images of light-absorbing structure

The applicability described above was assessed in an experiment. Figure 4.4 shows the experimental system. As a scattering medium, an Intralipid suspension (Fresenius Kabi AG) was mixed with distilled water and black ink (INK-30-B; Pilot Corp.) to produce a tissue-equivalent medium (μ_s' = 1.00 /mm, μ_a = 0.01 /mm). As an absorbing structure, a square black-painted metal plate (10.0 × 10.0 × 1.00 mm^3) was used. This absorber was placed in an acrylic container (40.0 × 100 × 100 mm^3) filled with scattering medium. The depth of the absorber from the observation surface was variable from 4.00 to 14.0 mm. This phantom was irradiated with the NIR light from a laser (Ti:Sapphire, 800 nm wavelength) through a beam expander for homogeneous illumination. An image is obtained using a cooled CMOS camera (C11440-10C; Hamamatsu Photonics K.K.) oriented toward the opposite face of the phantom to the light-incident side.

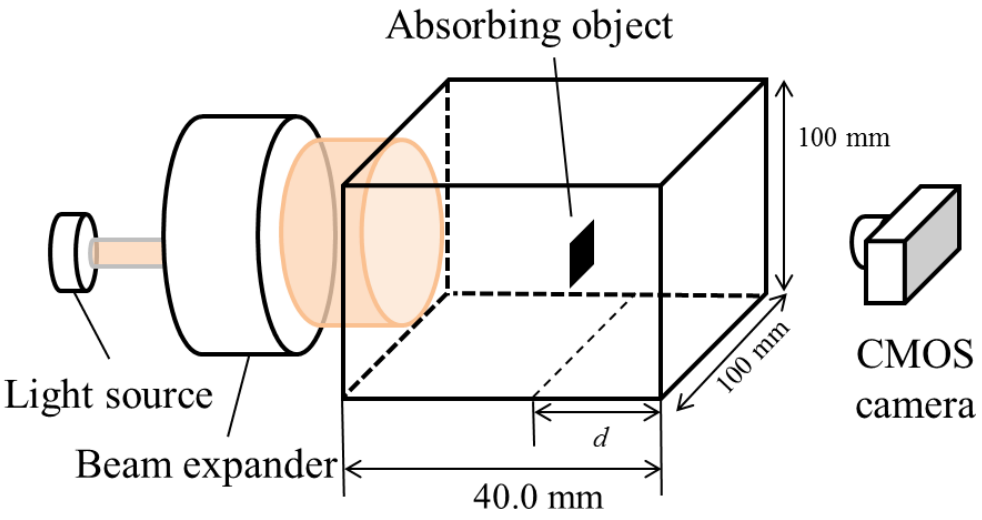

Fig. 4.4. Experimental setup for transillumination imaging: d = 4.00–14.0 mm.

The transillumination image x of the absorbing object was obtained as the original with transparent medium or clear water. Subsequently, the transparent medium was replaced by the scattering medium. Then the transillumination image y was obtained.

The measured PSF for the absorbing structure h_{abs} was calculated as

$$h_{abs} = y \otimes x, \tag{4.5}$$

where $\otimes$ denotes the deconvolution operation.

The measured h_{abs} was compared with the theoretical light-source PSF h obtained by Eq. (3.46) using the same conditions as those of the experiment. Figure 4.5 shows the comparison of PSF at depth d = 8.00 mm. Figures 4.5(a), 4.5(b), 4.5(c), and 4.5(d) respectively show the observed transillumination image with the scattering medium y, with the transparent medium x, measured PSF for absorbing structure h_{abs} calculated from Eq. (4.5), and light-source PSF h calculated from Eq. (3.46). Figure 4.6 shows the intensity profiles along the centerlines of Figs. 4.5(c) and 4.5(d). Figures 4.5(c), 4.5(d), and 4.6 show good agreement between the measured PSF from Eq. (4.5) and the light-source PSF from Eq. (3.46).

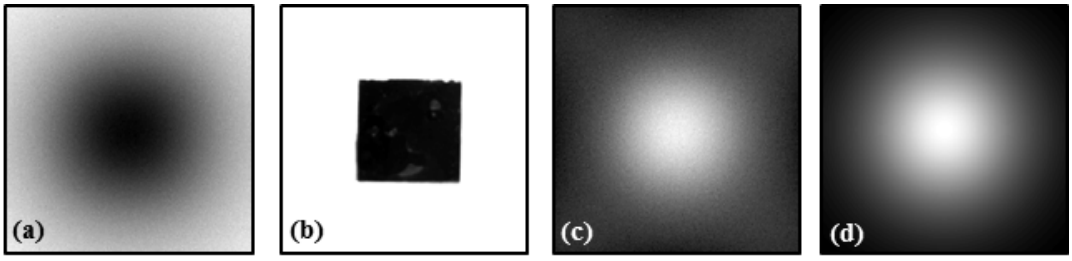

Fig. 4.5. Comparison of point spread function at depth d = 8.00 mm: (a) observed image with scattering medium, (b) observed image with transparent medium, (c) measured PSF from Eq. (4.5), (d) light-source PSF from Eq. (3.46).

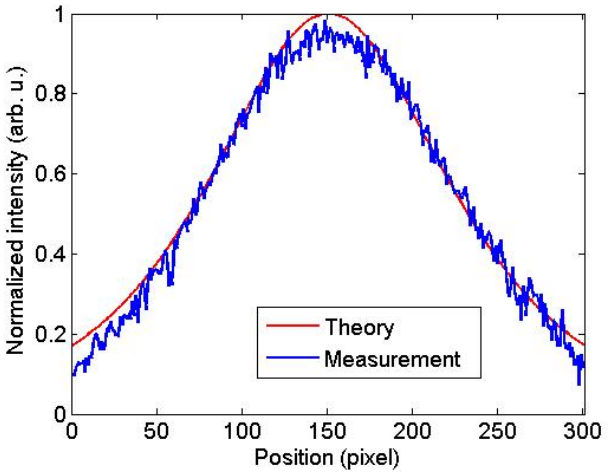

Fig. 4.6. Intensity profiles along the centerlines of Figs. 4.5(c) and 4.5(d).

Figure 4.7 shows the result of the comparison in terms of the spread (FWHM) of these two PSFs. At the same depth d, both PSFs were in good agreement.

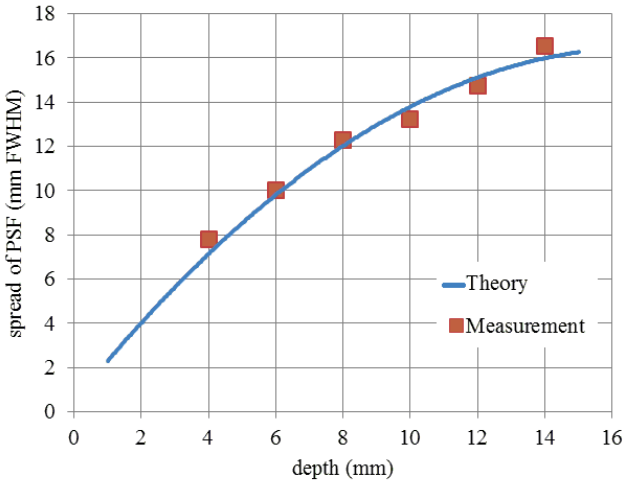

Fig. 4.7. Comparison between theoretical PSF for light source and measured PSF for absorber.

Through this analysis, it was confirmed that the depth-dependent PSF for the light source is applicable to the transillumination images of the absorbing structure.

4.3 Validation by simulation

In order to verify the validity of the proposed technique to transillumination image of light-absorbing structure with the light-source PSF, a simulation was performed. The proposed technique as given by Eq. (4.2) will be also compared with non-invert transillumination image as given by Eq. (4.1). A square light-absorbing object (15.0 × 15.0 mm^2) was simulated to be placed in the scattering medium (μ_s' = 1.00 /mm, μ_a = 0.01 /mm). The light source was assumed that was uniform and irradiated from outside the scattering medium. The depth from the observation surface of the scattering medium to the absorber was simulated from 2 to 10 mm by interval step 2 mm. The simulated transillumination images were obtained by convolving the original image with the light-source PSF from Eq. (3.46) at different depths. Figure 4.8 shows an example of the process flow of this simulation. Figures 4.9–4.13 show the results of the simulations. In these figures, the restored images obtained by performing the proposed technique and the non-invert technique were shown. And the intensity profiles along the dashed line show the comparison between the original image, the simulated image, the improvement by Eq. (4.1), and the improvement by Eq. (4.2).

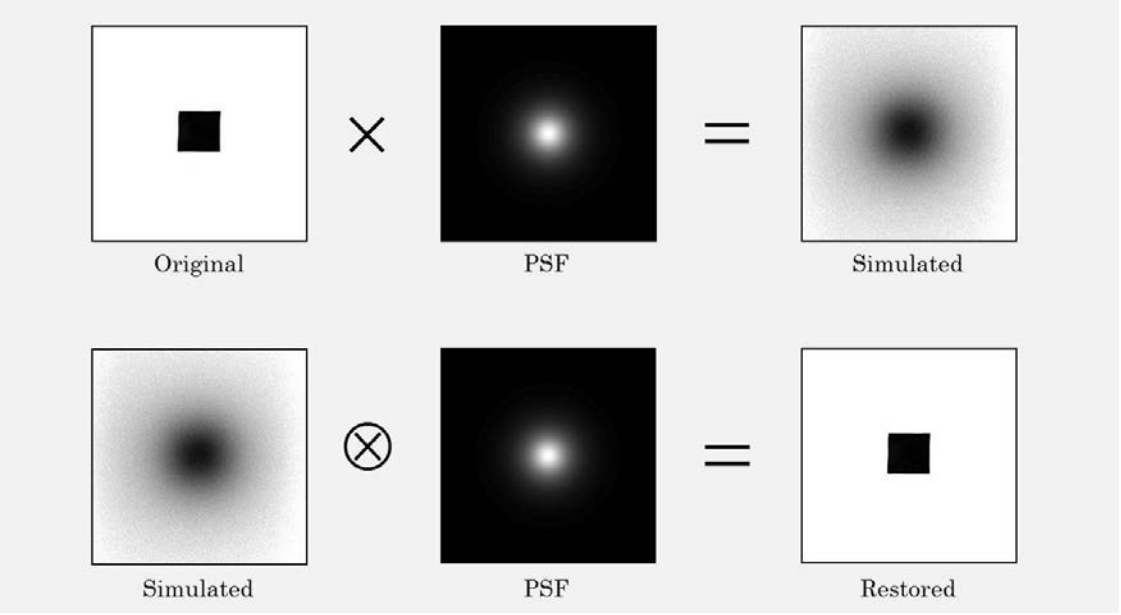

Fig. 4.8. Example of simulation process. × denotes the convolution operation. ⊗ denotes the deconvolution operation.

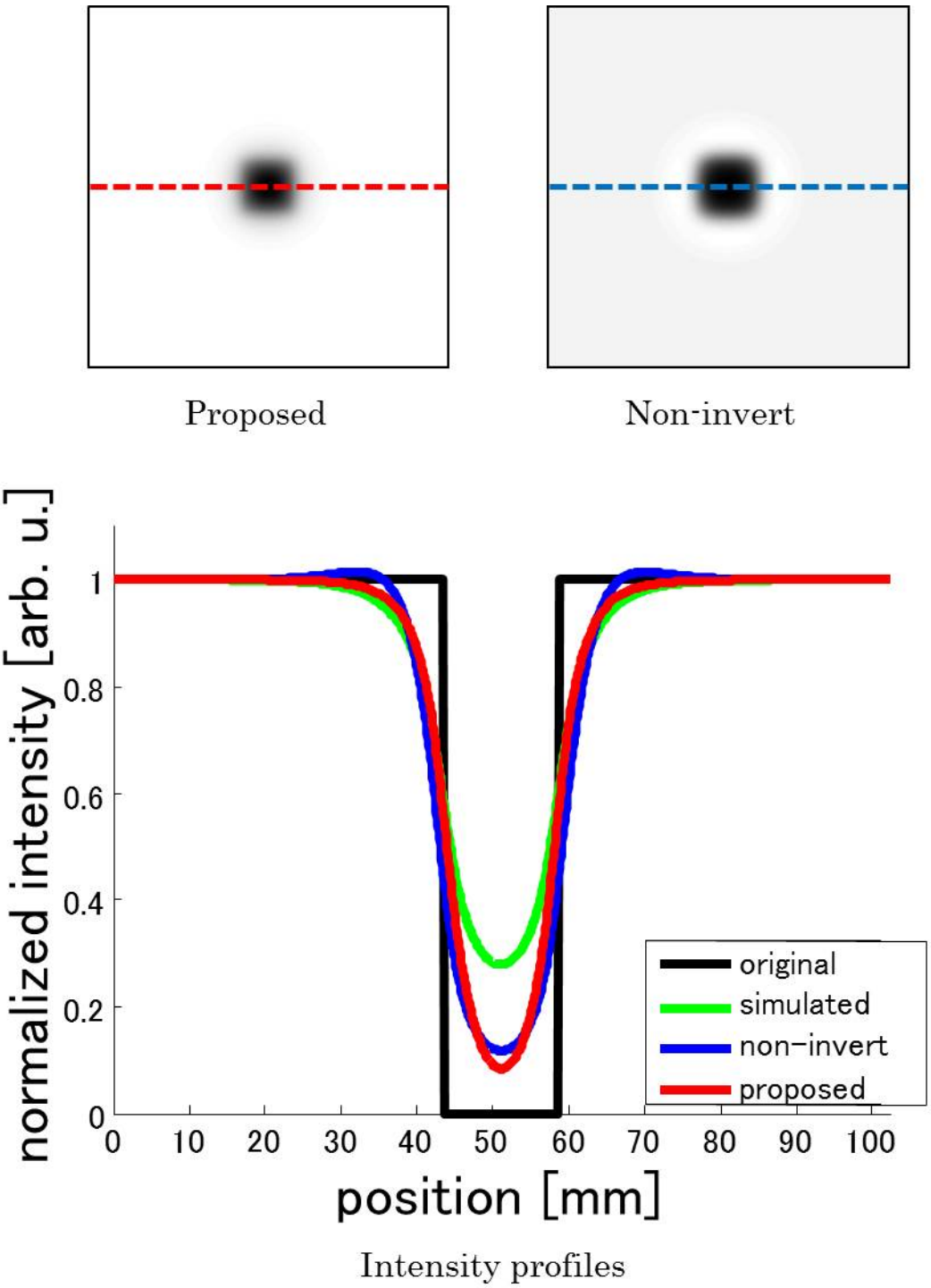

Fig. 4.9. Result of the scattering suppression technique using light-source PSF at depth d = 2 mm.

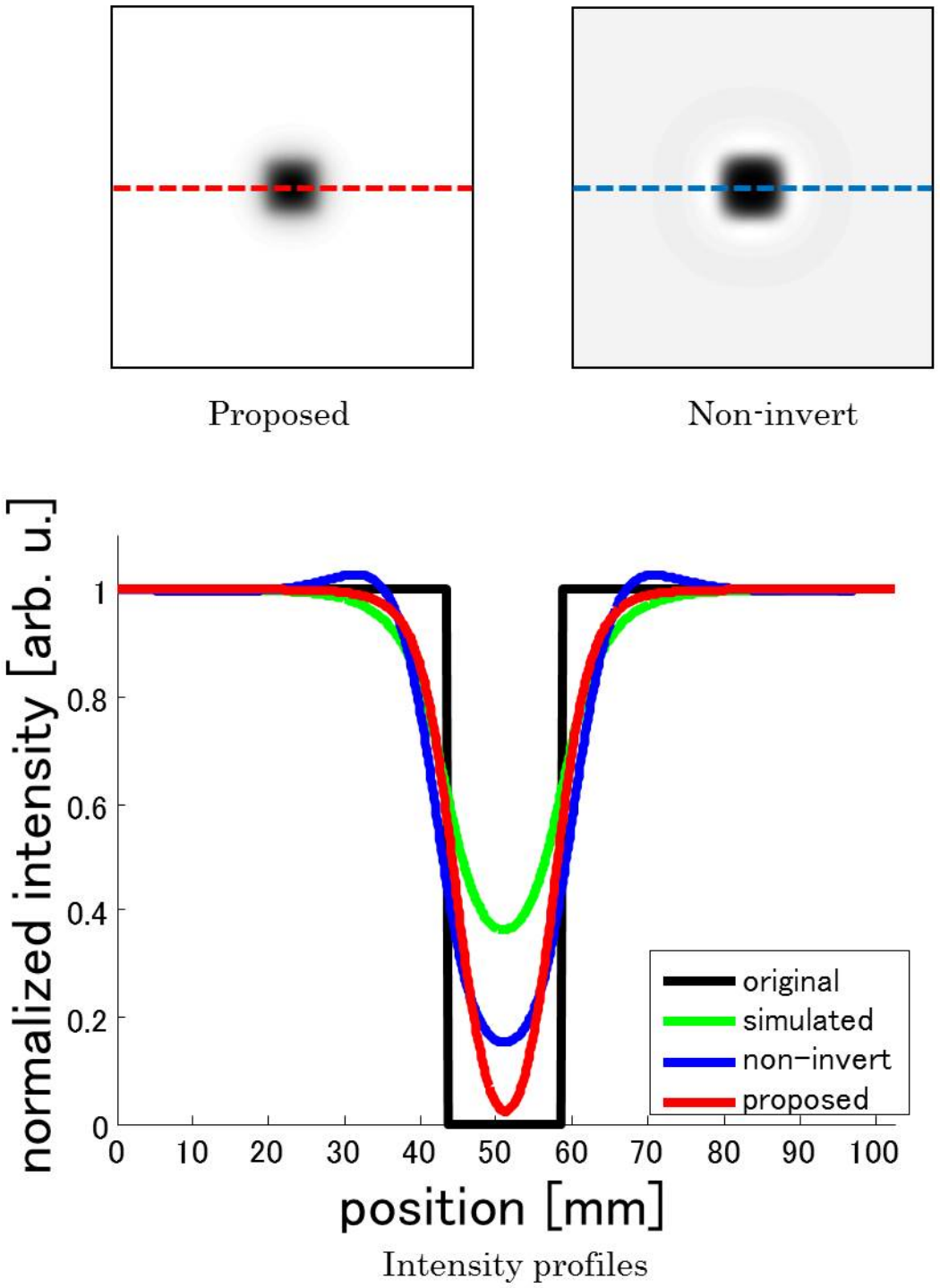

Fig. 4.10. Result of the scattering suppression technique using light-source PSF at depth d = 4 mm.

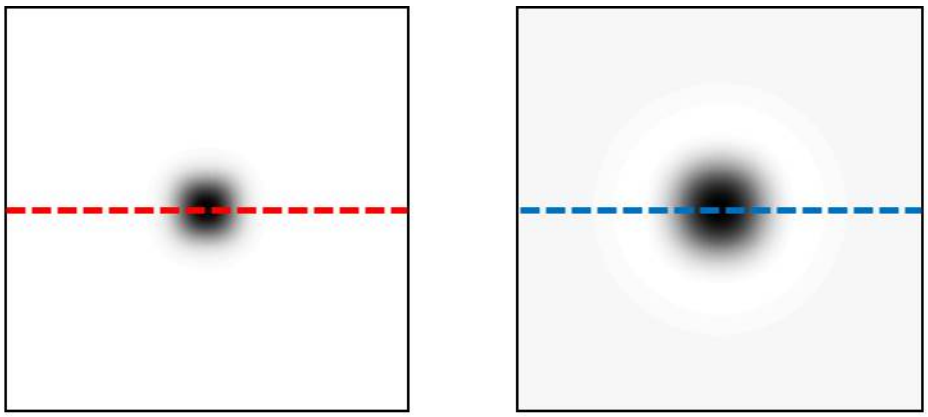

Proposed Non-invert

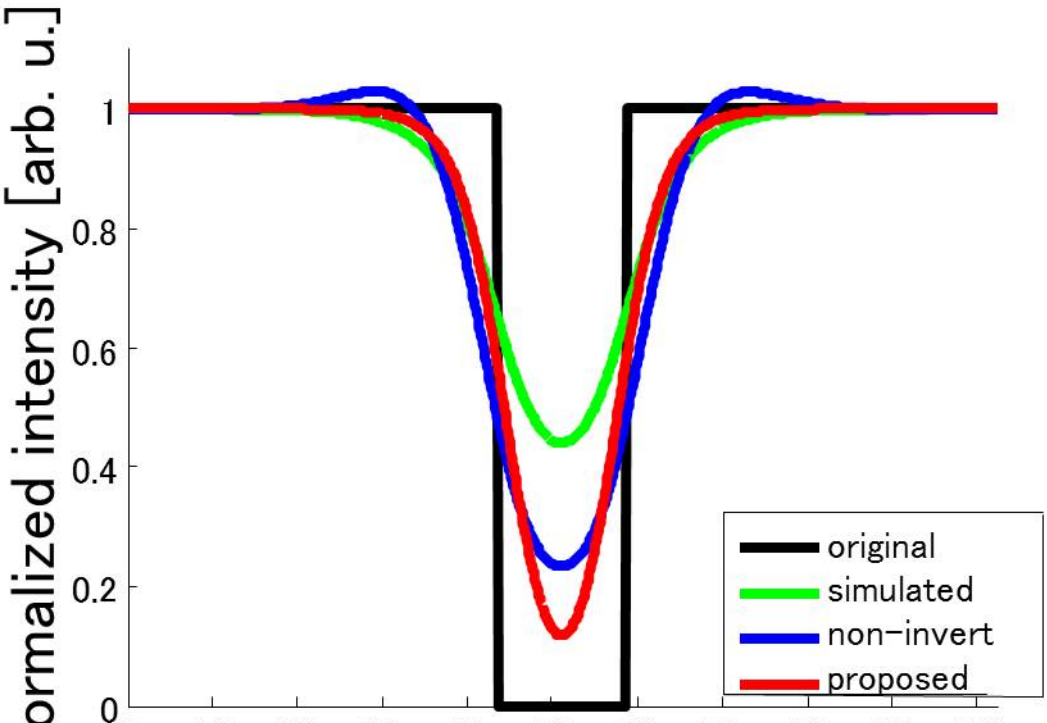

Intensity profiles

Fig. 4.11. Result of the scattering suppression technique using light-source PSF at depth d = 6 mm.

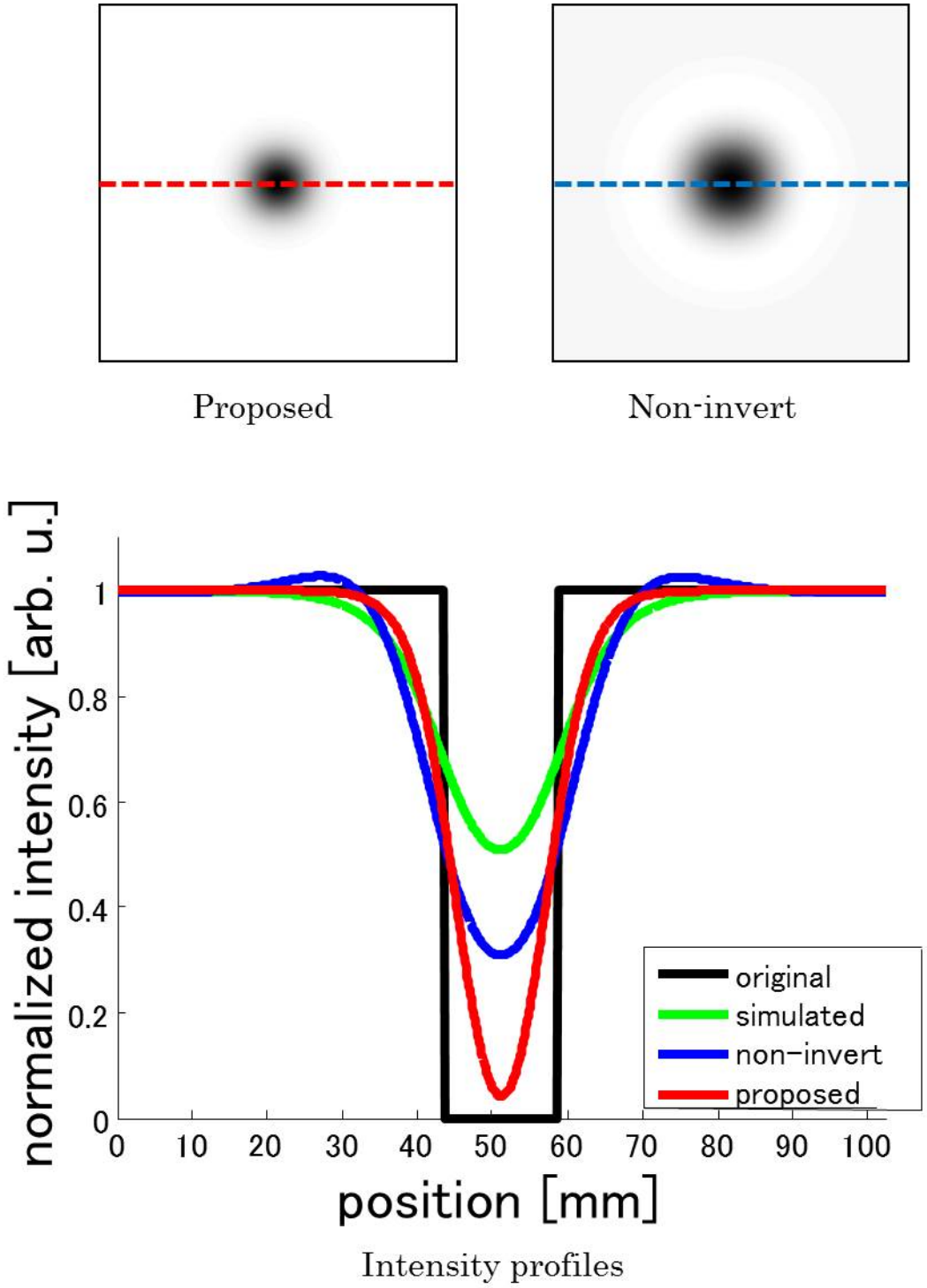

Fig. 4.12. Result of the scattering suppression technique using light-source PSF at depth d = 8 mm.

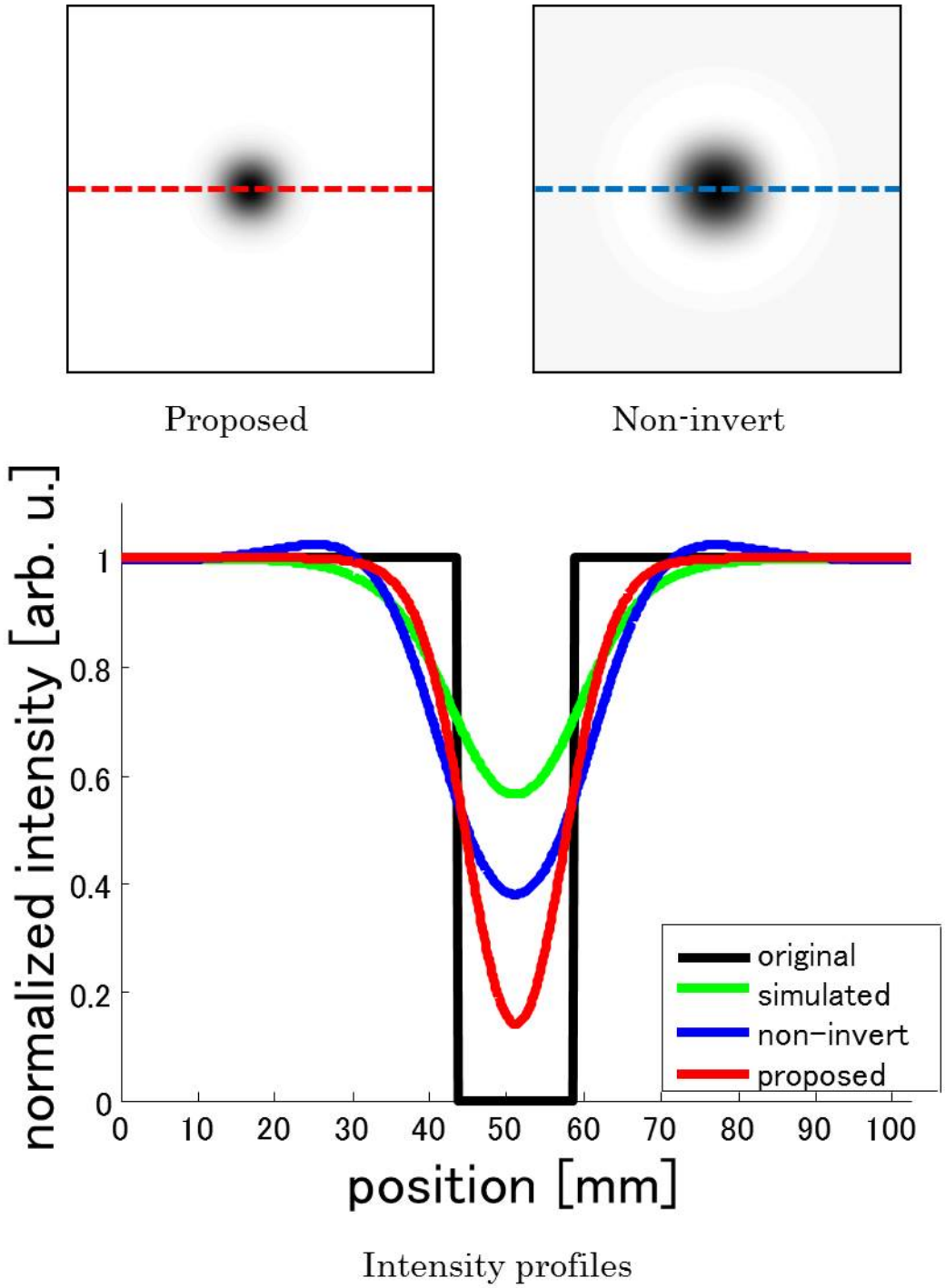

Fig. 4.13. Result of the scattering suppression technique using light-source PSF at depth d = 10 mm.

As shown in the Figs. 4.9–4.13, the scattering effect was effectively suppressed by deconvolution using the light-source PSF. From these intensity profiles, the sharpness and contrast in these restored images were improved. At each depth, the proposed technique using Eq. (4.2) gave better results than the non-invert technique using Eq. (4.1). It can be seen from the Figs. 4.9–4.13 that the restored shapes by the non-invert technique were insufficient. Figure 4.14 shows the result of the comparison in terms of the spead (FWHM) of the absorber. In addition, the restored images by using the proposed technique are substantially coinciding with the absorber. Through this analysis, it was confirmed that the scattering effect in the transillumination image can be effectively suppressed using the depth-dependent PSF for the light source. The effectiveness of proposed technique was confirmed in simulation. In the next section, the proposed technique will be examined in experiment with tissue-equivalent phantom.

Results presented in this section were equally contributed by Mr. Kohei Yamamoto, who was a master course student of my laboratory.

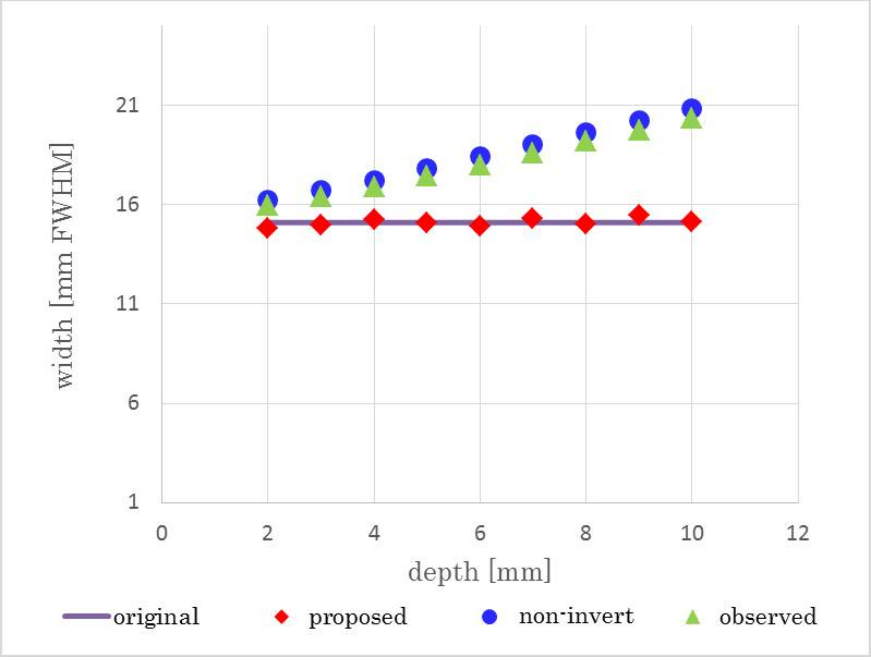

Fig. 4.14. Comparison between the improved images by using proposed technique and using non-invert technique in terms of the spread (FWHM) of the absorber.

4.4 Validation by experiment with tissue-equivalent phantom

This experiment was performed same as the experiment mentioned in section 4.2. The observed images y at the depth d =2.00, 6.00, 10.0, 14.0 mm were used to examine the effectiveness of the proposed technique. Figure 4.15 shows the original image x of the absorbing object obtained with transparent medium or clear water. The effectiveness of the proposed technique and non-invert technique was examined and compared. The results are presented in Figs. 4.16–4.19. As shown in the Figs. 4.16–4.19, the scattering effect was effectively suppressed by deconvolution using the light-source PSF. From these intensity profiles, the sharpness and contrast in these restored images were improved. At each depth, the proposed technique using Eq. (4.2) gave better results than the non-invert technique using Eq. (4.1). It can be seen from the Figs. 4.16–4.19 that the restored shapes by the non-invert technique were insufficient. Figure 4.20 shows the result of the comparison in terms of the spread (FWHM) of the absorber. In addition, the restored images by using the proposed technique are substantially coinciding with the absorber. Through this analysis, it was confirmed that the scattering effect in the transillumination image can be effectively suppressed using the depth-dependent PSF for the light source. The effectiveness of proposed technique was confirmed in experiments.

Results presented in this section were equally contributed by Mr. Kohei Yamamoto, who was a master course student of my laboratory.

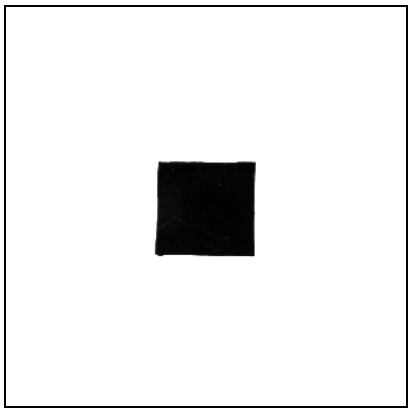

Fig. 4.15. Original image x of the absorbing object obtained with transparent medium.

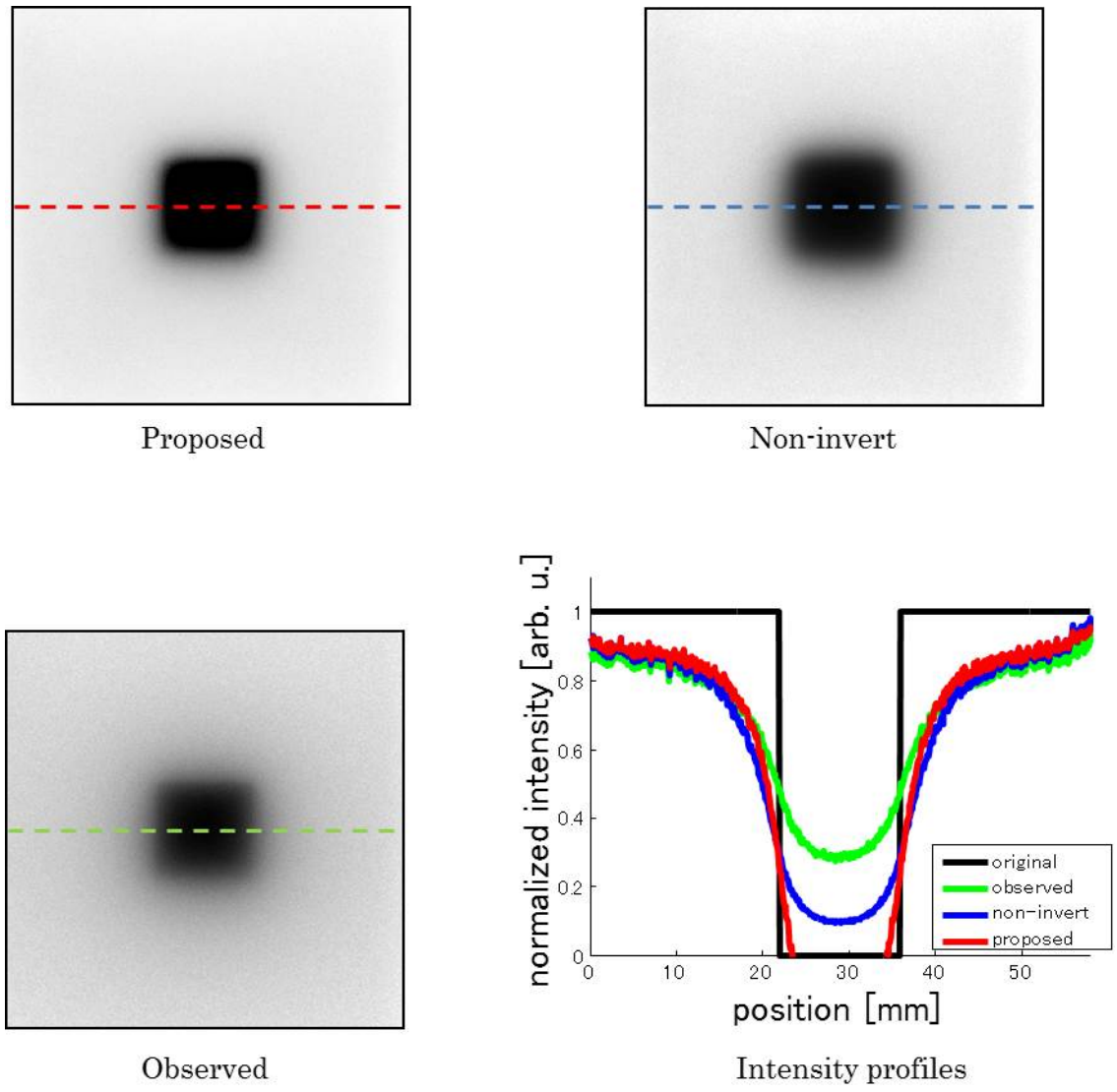

Fig. 4.16. Result with transillumination image of the absorber at d =2.00 mm. The intensity profiles show the distribution of light intensity along the dashed lines.

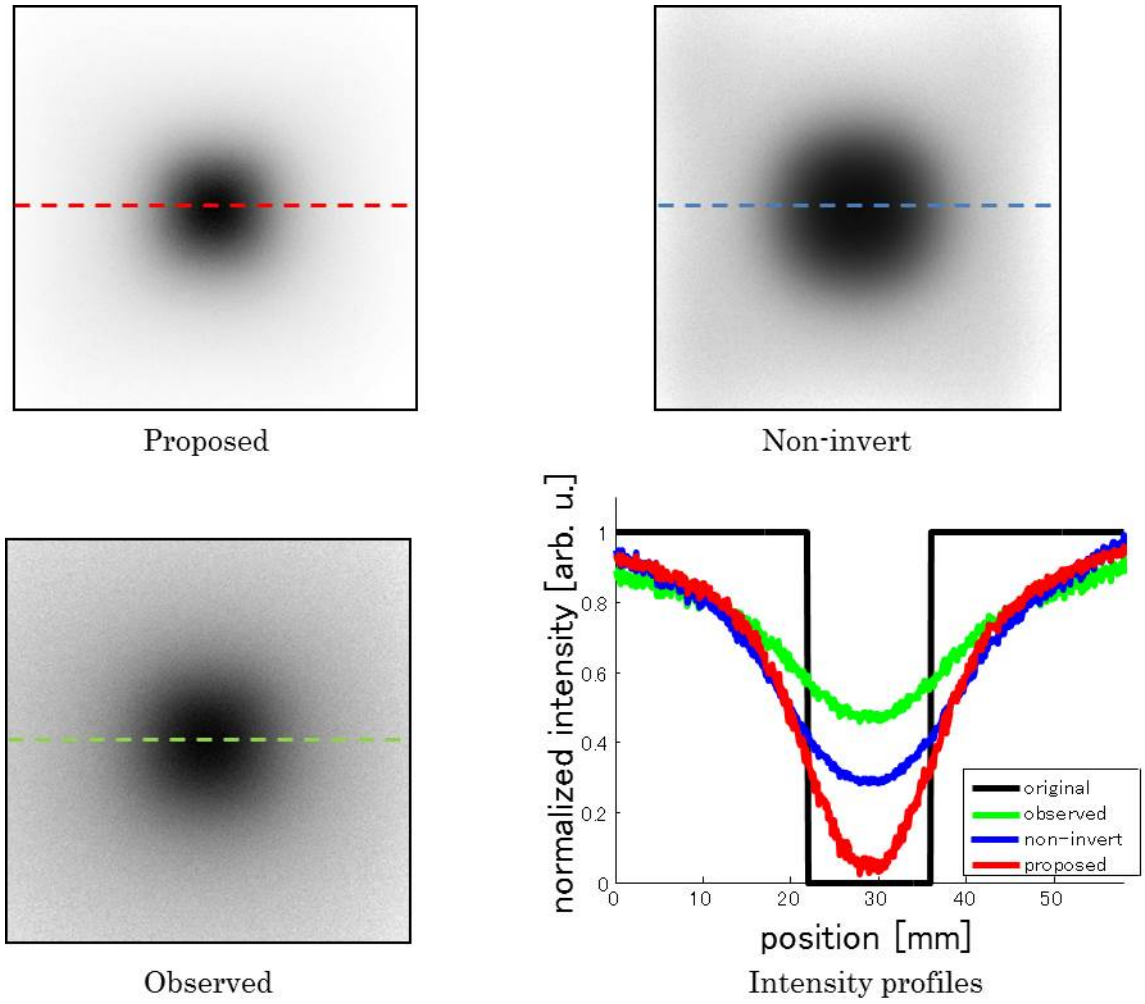

Fig. 4.17. Result with transillumination image of the absorber at d =6.00 mm. The intensity profiles show the distribution of light intensity along the dashed lines.

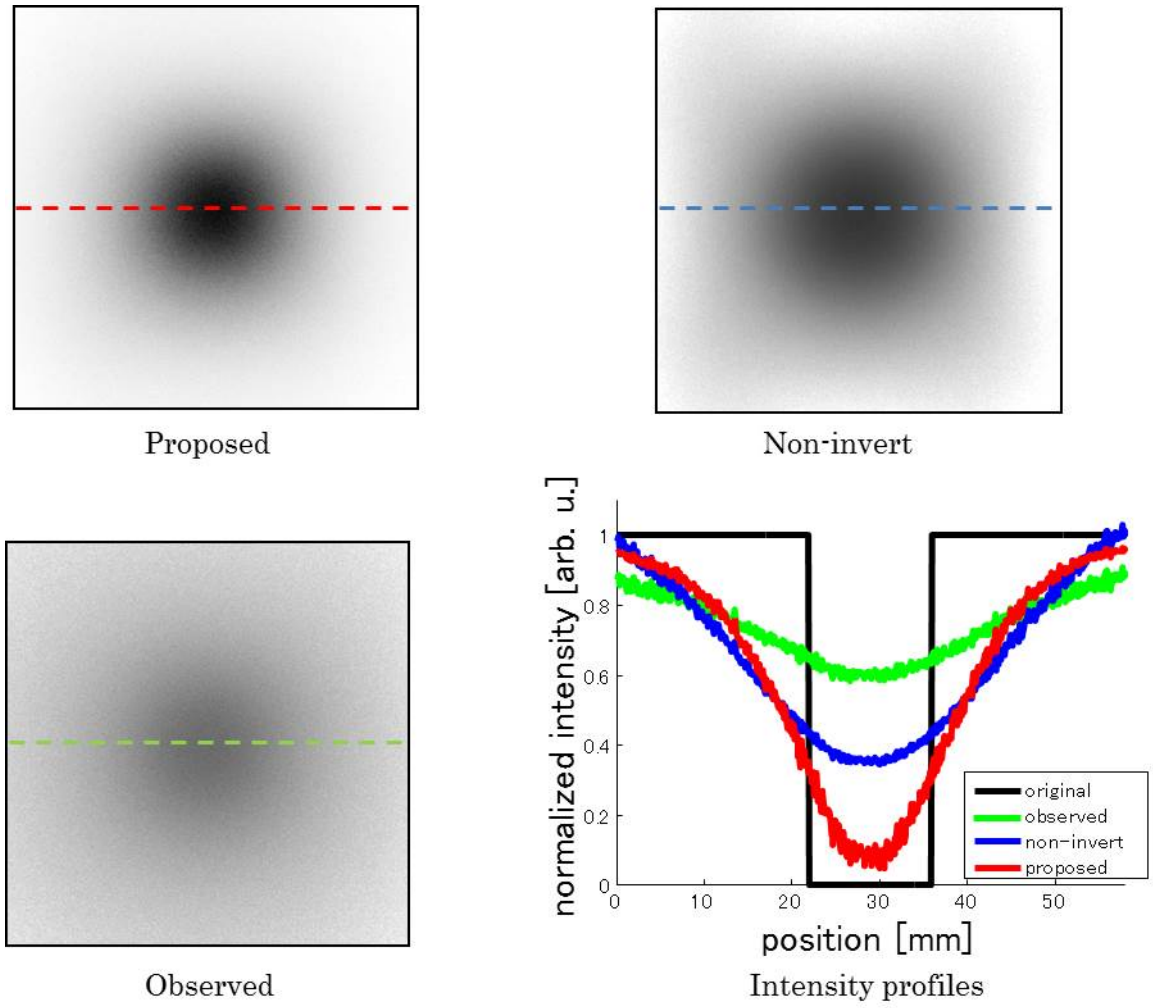

Fig. 4.18. Result with transillumination image of the absorber at d =10.0 mm. The intensity profiles show the distribution of light intensity along the dashed lines.

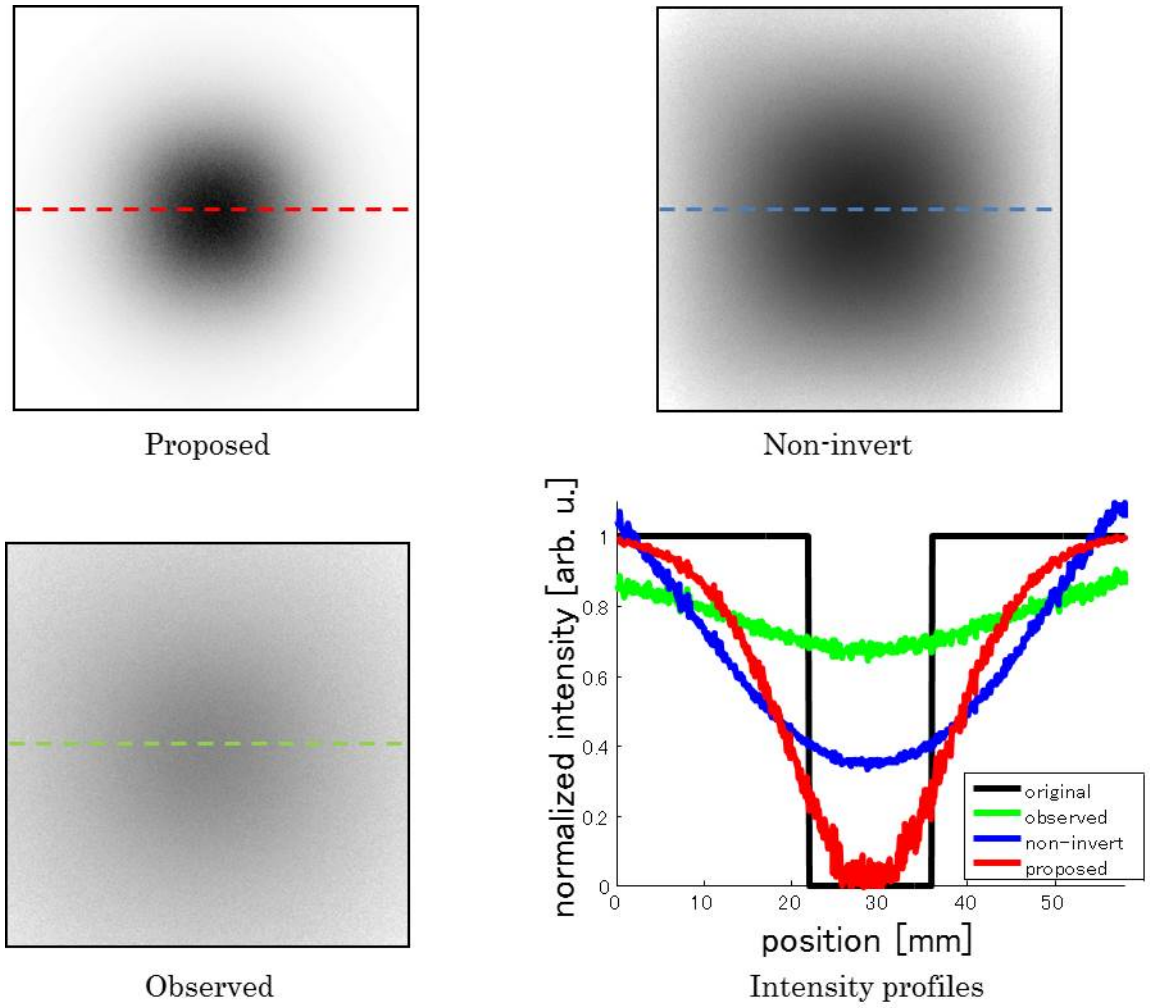

Fig. 4.19. Result with transillumination image of the absorber at d =14.0 mm. The intensity profiles show the distribution of light intensity along the dashed lines.

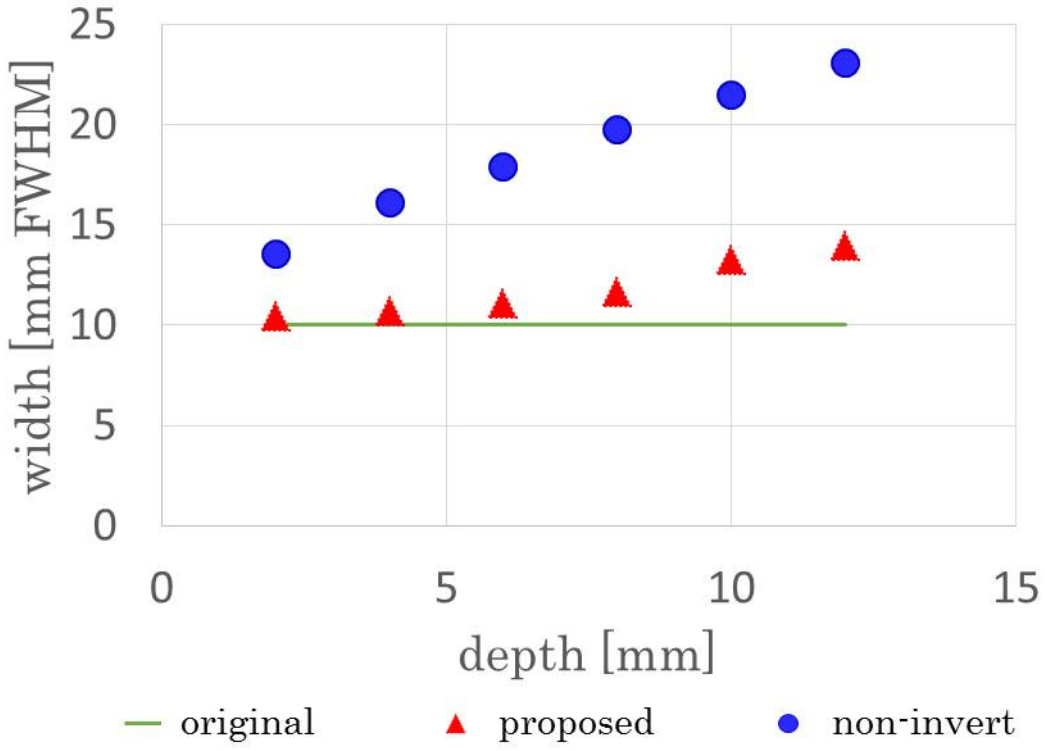

Fig. 4.20. Comparison between the improved images by using proposed technique and using non-invert technique in terms of the spread (FWHM) of the absorber.

4.5 Verification of scattering suppression with vessel model in tissue-equivalent medium using the n times deconvolution [4.2]

The effectiveness of the PSF from Eq. (3.46) to suppress the scattering effect in a transillumination image of the absorbing structure was examined in another experiment. Figure 4.21 shows the experimental system. This experiment was performed same as the experiment mentioned in section 4.2. A Y-shaped black tube (4.00 mm diameter) was placed in an acrylic container (40.0 × 100 × 100 mm^3) filled with scattering medium. The depth of the absorber from the observation surface was variable from 4.00 to 14.0 mm. Figure 4.22 shows the original image x of the absorbing object obtained with transparent medium.

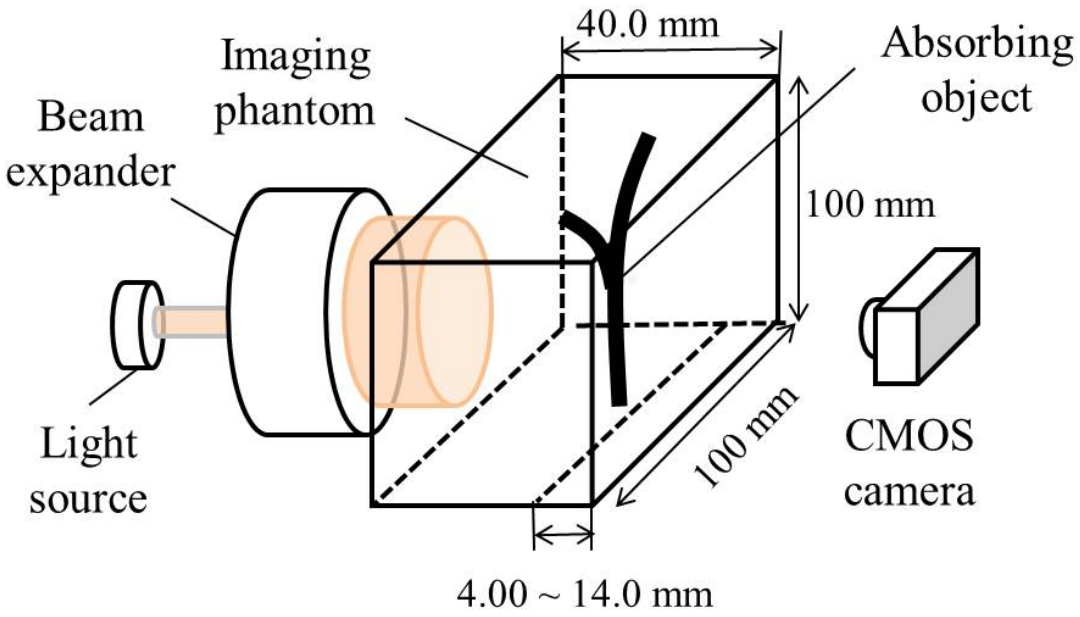

Fig. 4.21. Experimental setup for transillumination imaging: d = 4.00–14.0 mm.

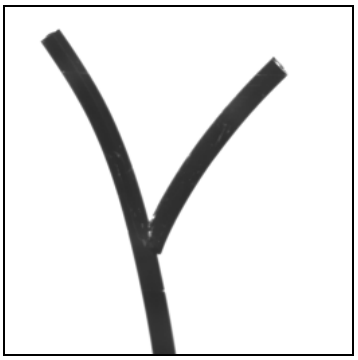

Fig. 4.22. Original image x of the absorbing object obtained with transparent medium.

In addition, the effectiveness of the n times deconvolution with $PSF_{part}(\rho)$ that obtained by Eqs. (4.3) and (4.4) will be also discussed in this section.

Figures. 4.23(a) and 4.23(c) show the observed transillumination image at d = 4.00 mm and the result of deconvolution with PSF using Eqs. (3.46) and (4.2). The separation of Y-shaped arms became clear by the deconvolution with an appropriate PSF as shown in Fig. 4.23(b). The scattering effect was effectively suppressed. The

effectiveness is apparent in the intensity profiles shown in Fig. 4.24, as well. The average Michelson contrasts were, respectively, 0.31 and 0.77 for observed and deconvoluted images. The sharpness parameters of these images were respectively, 0.18 and 0.54 for observed and deconvoluted images.

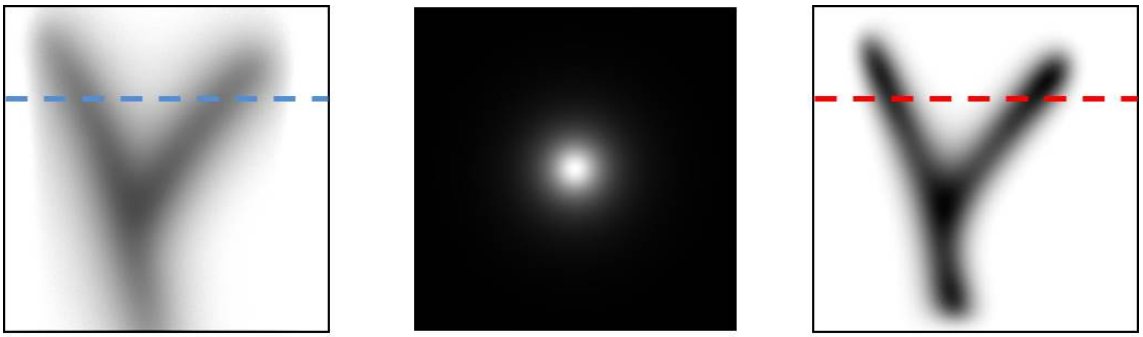

Fig. 4.23. Transillumination image at d = 4.00 mm: (a) observed image, (b) PSF from Eq. (3.46) at d = 4.00 mm, (c) deconvoluted image using Eq. (4.2) with PSF from Eq. (3.46).

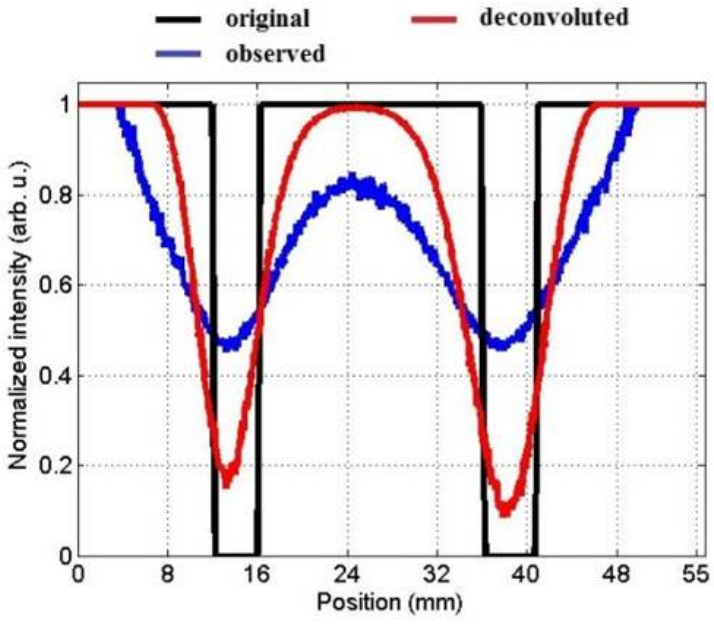

Fig. 4.24. Intensity profiles along the dashed lines in Fig. 4.23.

Through this experimental analysis, it was confirmed again that the PSF derived for a light source by Eq. (3.46) is applicable and effective to suppress the scattering effect in transillumination images.

Figures. 4.25(a) and 4.25(b) show the observed transillumination image at d = 10.0 mm and the result of deconvolution with PSF using Eqs. (3.46) and (4.2). Due to the strong scattering effect, the shape of the absorber was difficult to discern.

As mentioned in section 4.1, the width of light-source PSF becomes larger, when the depth from the scattering medium to the light source is increased as shown in the example in Fig. 4.7. Then, the deconvolution with Lucy-Richardson algorithm requires much iterative calculation and result tends to be unstable.

Fig. 4.25(c) shows the result of three-time piece-wise deconvolution with $PSF_{part}(\rho)$ that obtained by Eqs. (3.46), (4.3), and (4.4). The Y-shape structure became recognizable by the deconvolution. The better performance with the $PSF_{part}(\rho)$ could be seen in these figures in Fig. 4.25 and the intensity profiles in Fig. 4.26, as well. Figure 4.27 shows the calculated $PSF(\rho)$ from Eq. (3.46) at d = 10.0 mm and the $PSF_{part}(\rho)$ obtained by Eqs. (4.3) and (4.4). As shown in Fig. 4.27, the re-convolved PSF from three $PSF_{part}(\rho)$ was show good agreement with the calculated PSF from Eq. (3.46).

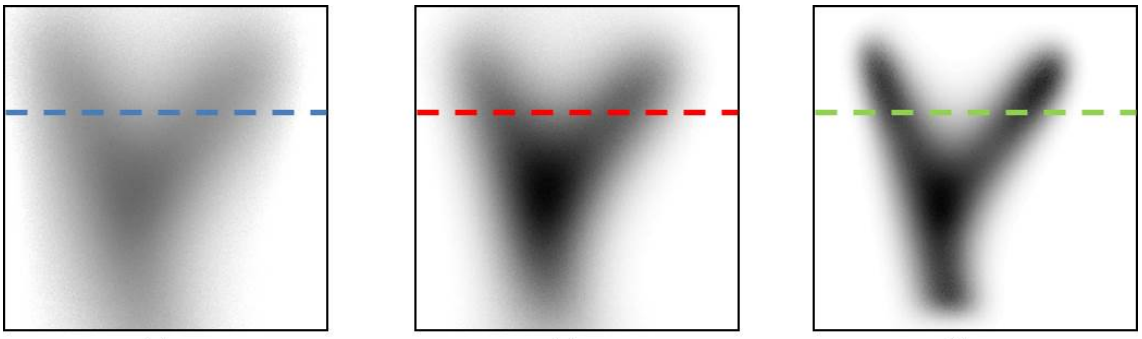

Fig. 4.25. Transillumination image at d = 10.0 mm: (a) observed image, (b) deconvoluted image using Eq. (4.2) with PSF from Eq. (3.46), (c) three-time piece-wise deconvolution with $PSF_{part}(\rho)$ that obtained by Eqs. (3.46), (4.3), and (4.4).

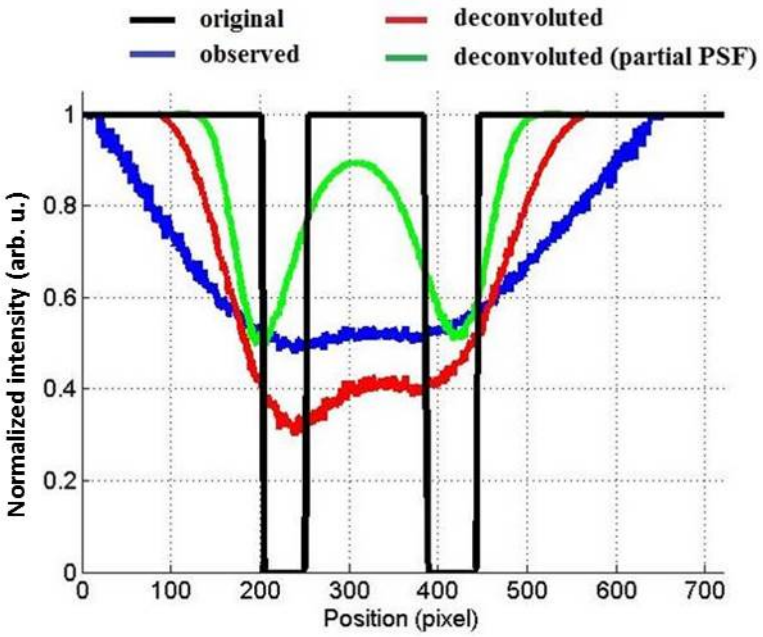

Fig. 4.26. Intensity profiles along the dashed lines in Fig. 4.25.

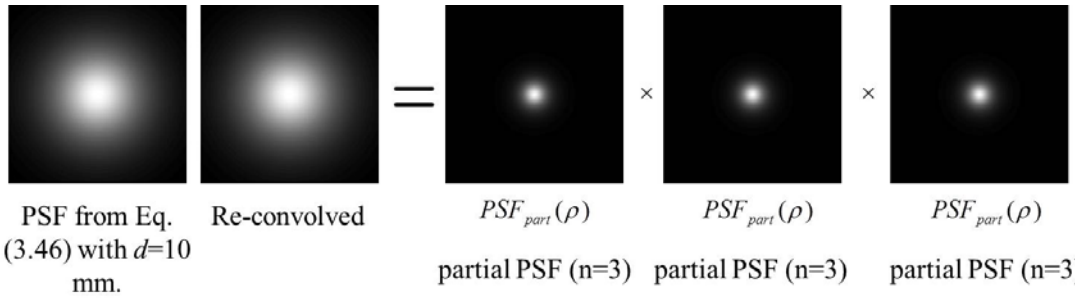

Fig. 4.27. The PSF calculated from Eq. (3.46) at d = 10.0 mm and $PSF_{part}(\rho)$ calculated from Eq. (4.3) and (4.4).

The scattering effect was effectively suppressed. The effectiveness is apparent in the intensity profiles shown in Fig. 4.26, as well. The average Michelson contrasts were, respectively, 0.06, 0.11 and 0.28 for observed, deconvoluted and three-time piece-wise deconvoluted images. The sharpness parameters of these images were respectively, 0.05, 0.17 and 0.30 for observed, deconvoluted and three-time piece-wise deconvoluted images.

Through this experimental analysis, it was confirmed that the proposed technique is applicable and effective to suppress the scattering effect in transillumination images not only for the shallow absorbing structure, but also for the deep absorbing structure. With the three-time piece-wise deconvolution technique, the deconvolution operation using Lucy-Richardson algorithm becomes stable and fast convergent.

4.6 Verification of the proposed technique with animal-tissue phantom

In this section, the applicability of the proposed technique will be examined in experiment with avian skeletal muscle (i.e. chicken-breast meat). Figure 4.28 shows experimental setup. As an absorbing structure, a black-painted metal plate (10.0 × 100 × 1.00 mm^3) was used. This absorber was placed at d =6.00 mm from the observation surface in an acrylic container (40.0 × 100 × 100 mm^3) filled with chicken-breast meat. This phantom was irradiated with the NIR light from a laser (Ti:Sapphire, 800 nm wavelength) through a beam expander for homogeneous illumination. An image is obtained using a cooled CMOS camera (C11440-10C; Hamamatsu Photonics K.K.) oriented toward the opposite face of the phantom to the light-incident side.

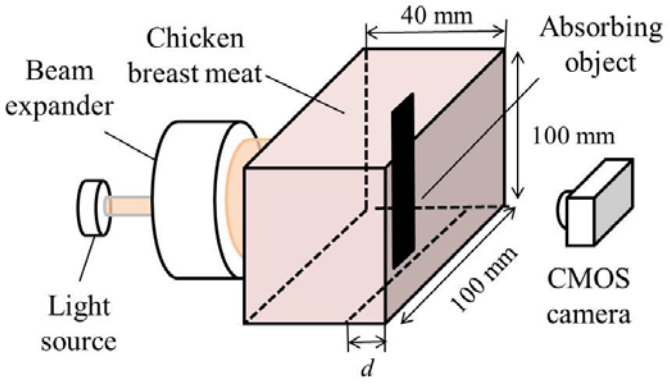

Fig. 4.28. Experimental setup for transillumination imaging: d = 6.00 mm.

Figures 4.29(a) and 4.29(b) show the restored images by using the proposed technique and the non-invert technique, respectively. Figure 4.29(c) shows the observed image. Figure 4.29(d) shows the intensity profiles along the dashed lines of the images

shown in Figs. 4.29(a), 4.29(b), and 4.29(c).

The measured widths of the absorber in the restored images of the proposed technique and the non-invert technique in terms of the spread (FWHM) of the absorbers are 11.8 mm and 16.5 mm, respectively. As shown in the Fig. 4.29, the effectiveness of the proposed technique was confirmed.

Results presented in this section were equally contributed by Mr. Kohei Yamamoto, who was a master course student of my laboratory.

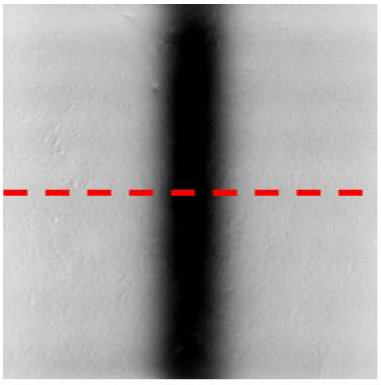

(a) Proposed

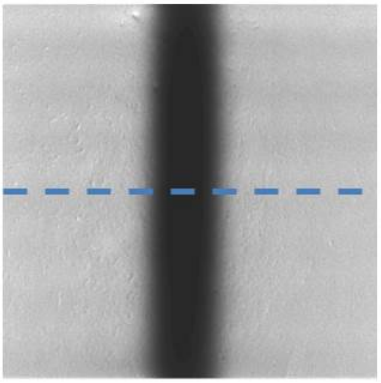

(b) Non-invert

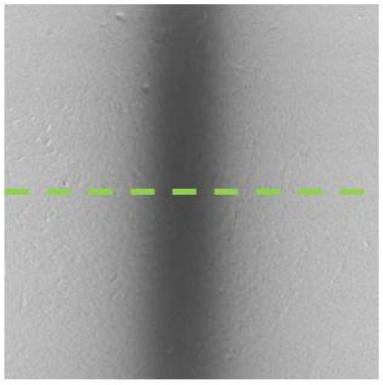

(c) Observed

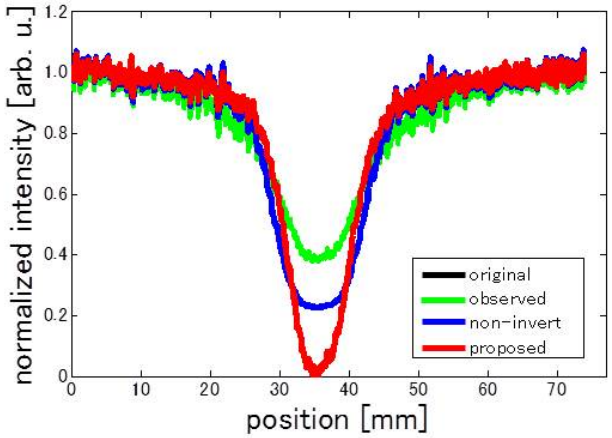

(d) Intensity profiles

Fig. 4.29. Result with transillumination image of the absorber at d =6.00 mm. The intensity profiles show the distribution of light intensity along the dashed lines. (μ_s' =1.00 /mm, μ_a =0.01 /mm).

4.7 Conclusion

For suppression the strong scattering effect in transillumination image of light-absorbing structure, a novel scattering suppression technique has devised by deconvolution with the light-source PSF. The effectiveness of the proposed technique was verified and confirmed in simulation and experiment.

In summary, the proposed scattering suppression process for transillumination image consists of 4 steps:

1. Calculate the appropriate PSF from Eq. (3.46), then calculate the $PSF_{part}(\rho)$,
2. Invert the transillumination image to obtain the absorption image,
3. Suppress the scattering effect in the absorption image by three-time piece-wise deconvolution with $PSF_{part}(\rho)$,
4. Invert the improved image from step 3 to obtain the recovered image.

The deconvolution operation in this thesis will be performed using Lucy-Richardson algorithm with the iteration number is up to 10. With the three-time piece-wise deconvolution technique, the Lucy-Richardson algorithm becomes stable and fast convergent.

Using this proposed technique, it would be able to recover the light-absorbing structure in transillumination image with the appropriate PSF. It is useful to provide appropriate projection images for the reconstruction of the 3D image reconstruction of light-absorbing structure from transillumination image.

The applicability of 3D image reconstruction will be described in the next chapter.

Chapter 5
3D reconstruction of the known-structure transillumination images

In previous chapter, the scattering effect in transillumination images can be suppressed using the proposed technique. Considering a transillumination image as a projection in the computed tomography, one can reconstruct the 3D structure of the internal absorption distribution of a turbid medium. In this chapter, the feasibility of this 3D reconstruction was examined in experiment.

5.1 3D reconstruction from transillumination images with tissue-equivalent phantom [5.2]

Figures 5.1 and 5.2 show the experimental setup and the target structure of this experiment. A slant cylindrical post (3.00 mm diameter, 30.6 mm length) was fixed in the acrylic container (35.0 × 100 × 100 mm^3) filled with a scattering medium. Intralipid suspension (Fresenius Kabi AG) was mixed with distilled water to produce tissue-equivalent medium (μ_s' =1.00 /mm, μ_a = 0.00536 /mm).

Laser light (Ti:Sapphire, 850 nm wavelength) was illuminated from one side of the container and the transillumination image was recorded using a cooled CMOS camera (C11440-10C; Hamamatsu Photonics K.K.) from another side of the container. This recording was repeated while rotating the absorber post around the rotation axis shown in Fig. 5.2 using a mechanical rotary motion system.

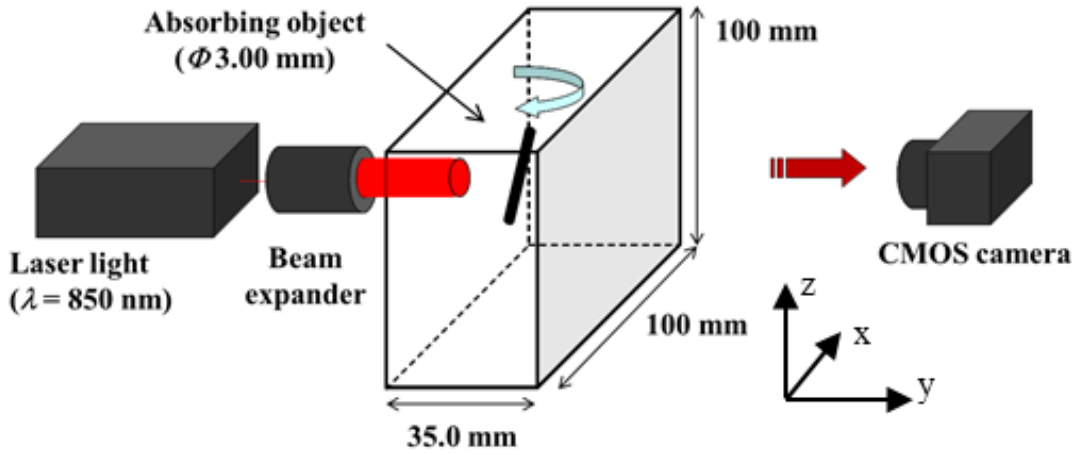

Fig. 5.1. Experimental setup.

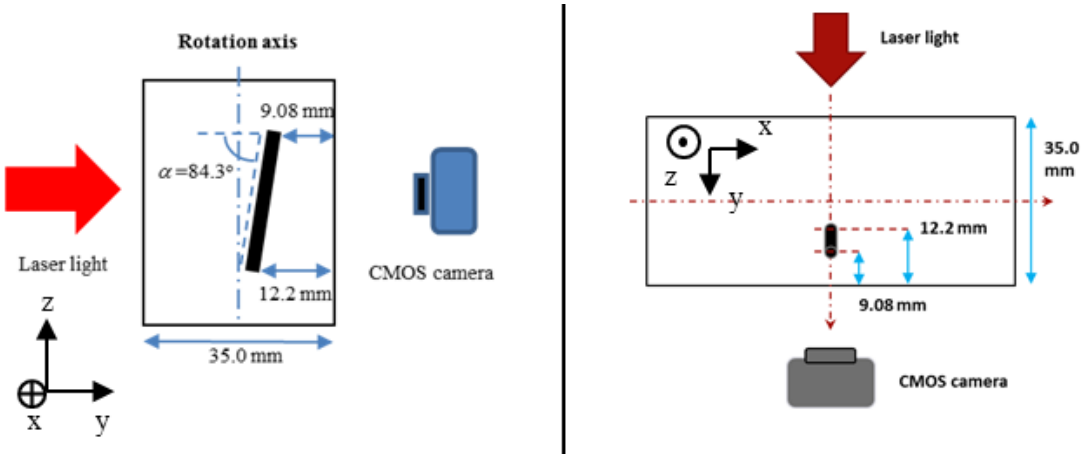

Fig. 5.2. Side view and top view of phantom model.

In this case, the depth of the absorber from the observing surface of the scattering medium was not constant along the vertical axis of rotation. Therefore, the PSFs with known different depths were applied to a transillumination image, and horizontal intensity profiles were extracted at the proper vertical heights in the improved image obtained by the proper PSF with the correct depth. These horizontal intensity profiles were obtained from different circumferential orientations. The cross-sectional image was reconstructed using the filtered back-projection algorithm. Finally, the cross-sectional images were piled up along the vertical axis and reconstructed the 3D structure.

Figure 5.3 shows the observed transillumination image and the result of the PSF deconvolution. In this case, the absorbing post was parallel to the observation surface, and it is able to use the PSF with a single depth. The observed image was degraded severely by the effect of strong scattering. Its effect was greatly suppressed when using the proposed technique. Figures 5.4 and 5.5 show the cross-sectional images reconstructed from the observed and deconvoluted transillumination images. With the observed images, the position of the absorber was difficult to identify in cross-sectional images. They became clearly identifiable using the proposed technique. The accuracy of the cross-sectional image was analyzed at 10 different heights. The reconstruction error in the estimated depth $\hat{d}$ in the improved cross-sectional images varied 0.25–2.97% along the vertical axis.

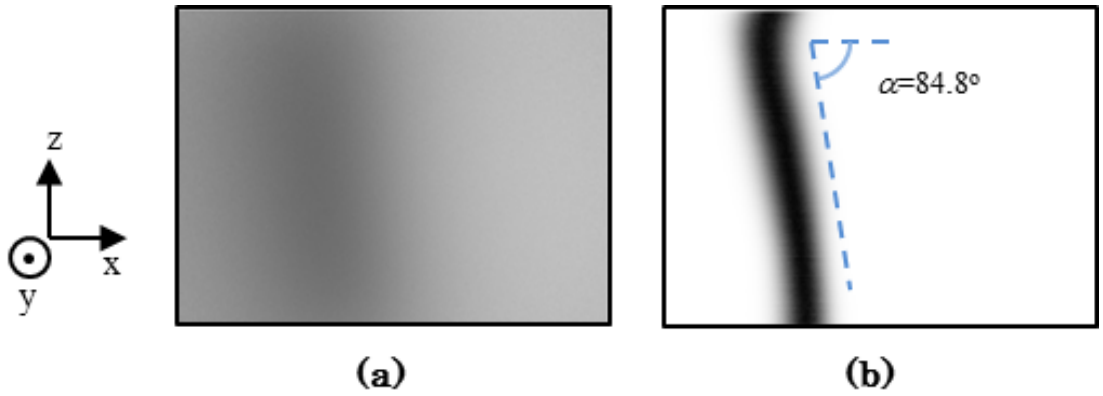

Fig. 5.3. Observed and deconvoluted images of absorber: (a) observed image (contrast and sharpness are 0.71 and 0.050), (b) deconvoluted image (contrast and sharpness are 0.90 and 0.71).

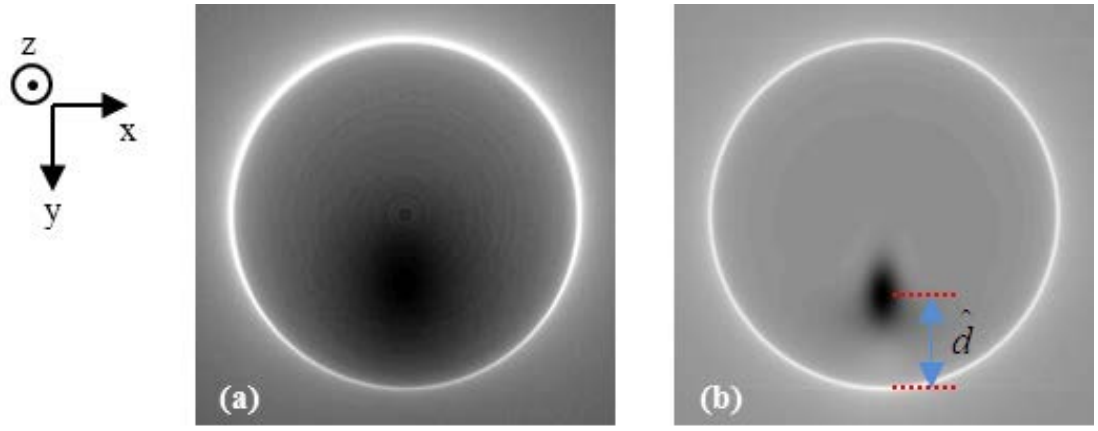

Fig. 5.4. CT image at the top of the absorber: (a) from observed images, (b) from deconvoluted images. Depth of estimated absorber center ($\hat{d}$) was 9.35 mm for true depth 9.08 mm.

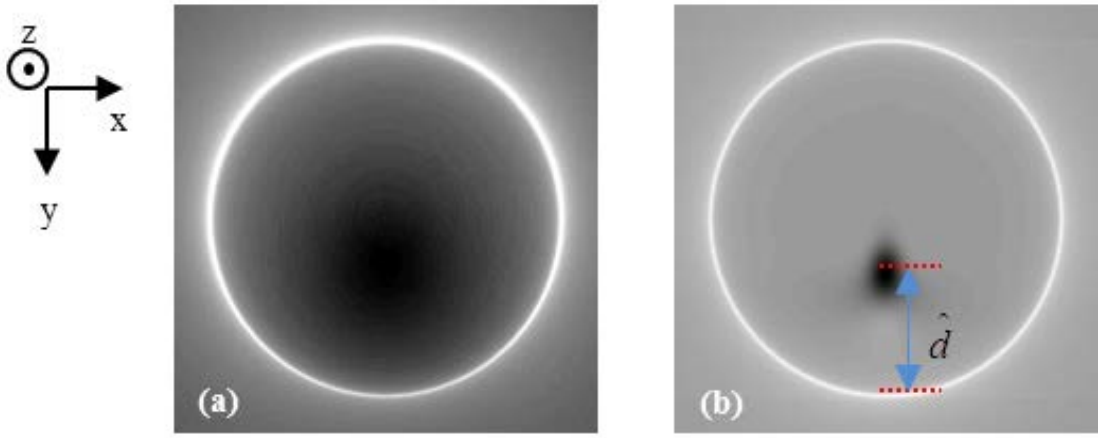

Fig. 5.5. CT image at the bottom of the absorber: (a) from observed images, (b) from deconvoluted images. Depth of estimated absorber center ($\hat{d}$) was 12.1 mm for true depth 12.2 mm.

Figure 5.6 shows the result of the 3D reconstruction. The absorbing structure in tissue-equivalent medium was reconstructed clearly using the proposed technique.

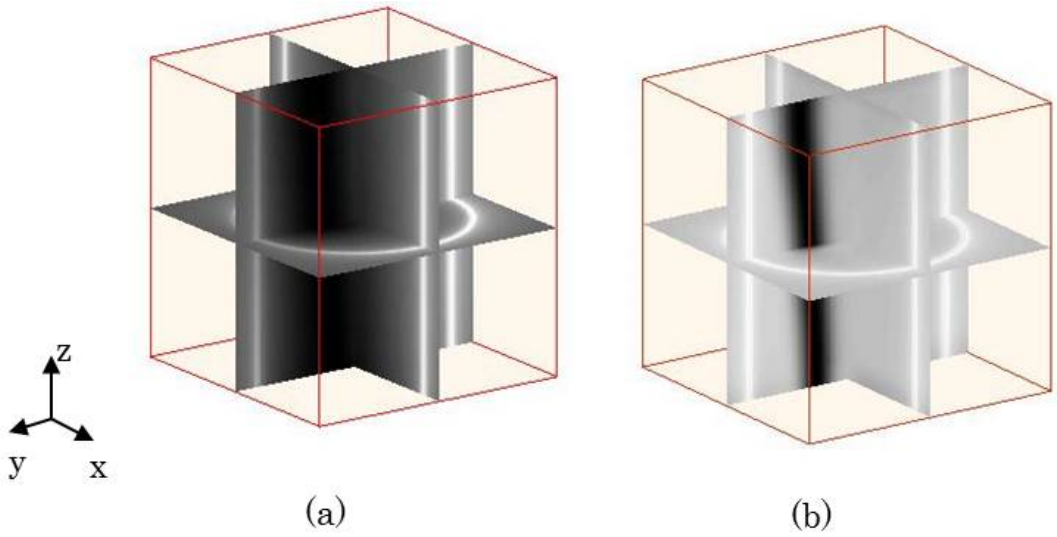

Fig. 5.6. 3D Reconstruction of absorber in turbid medium: (a) from observed images, (b) from deconvoluted images.

For rendering the 3D structure from these cross-sectional images using the iso-surface rendering technique, the average histogram of intensity distribution was used. The histogram was made for each cross-sectional image, then summation with other histograms to produce the histogram of the volume data set. From this histogram, the isolate value or threshold value for rendering the structure can be selected. Figure 5.7 shows the histogram of volume data from observed data and from deconvoluted data. The isovalue was common and empirically selected.

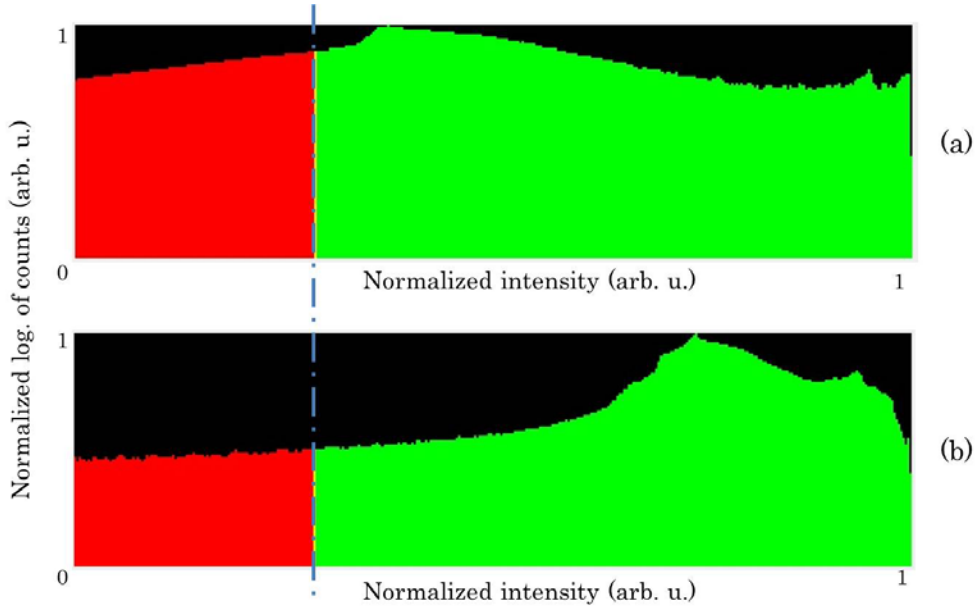

Fig. 5.7. Histogram of volume data: (a) from observed images, (b) from deconvoluted images. The dashed line indicates the threshold value. The histogram created by using showvol isosurface render [5.1].

Figure 5.8 shows the rendering images of the observed data and the deconvoluted data with common threshold value. The scattering effect was suppressed efficiently, and the absorbing objects were visualized.

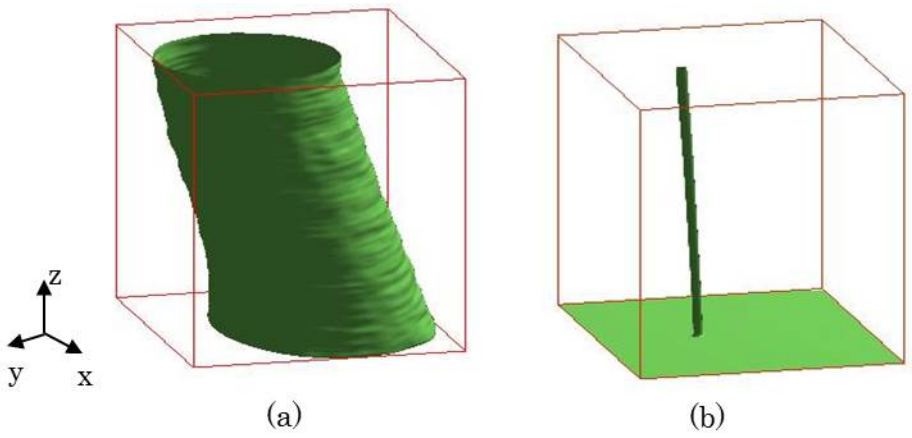

Fig. 5.8. 3D Reconstruction of absorber in turbid medium using iso-surface rendering technique with a common single threshold value: (a) result of thresholding on image Fig. 5.6(a), (b) result of thresholding on image Fig. 5.6(b).

5.2 3D reconstruction from transillumination images with animal-tissue phantom

To validate the accuracy of the result in heterogeneous animal tissue, 3D imaging was attempted with known absorbing structure. The method of the experiment was the same as that with the tissue-equivalent phantom mentioned above. Figure 5.9 shows the experimental setup. A black-painted slant cylindrical post (3.00 mm diameter, 30.1 mm length) was fixed in the rectangular container filled with avian skeletal muscle (i.e. chicken breast meat). A transparent acrylic cylindrical tube (30.0 mm diameter, 2.00 mm wall thickness) rotated the post around the rotation axis as shown in Fig. 5.10.

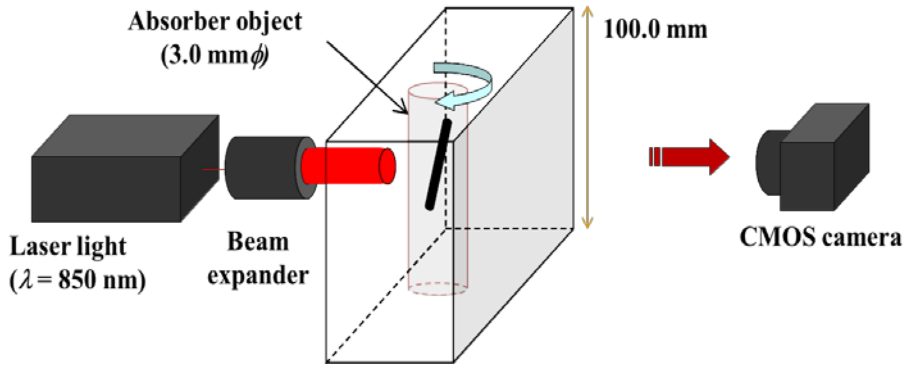

Fig. 5.9. Experimental setup.

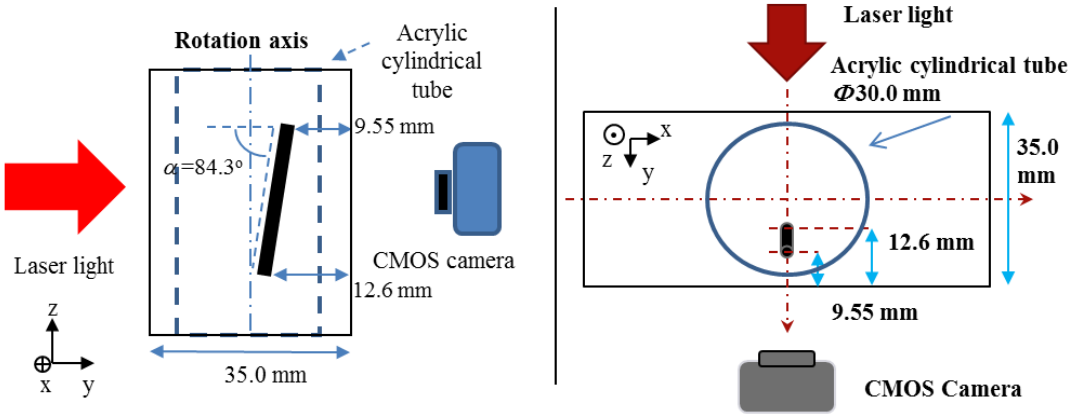

Fig. 5.10. Side view and top view of phantom model.

Figure 5.11 shows an example of the transillumination image at 0 degree and the

result of the proposed technique. The scattering effect was suppressed efficiently, and the absorbing objects were visualized.

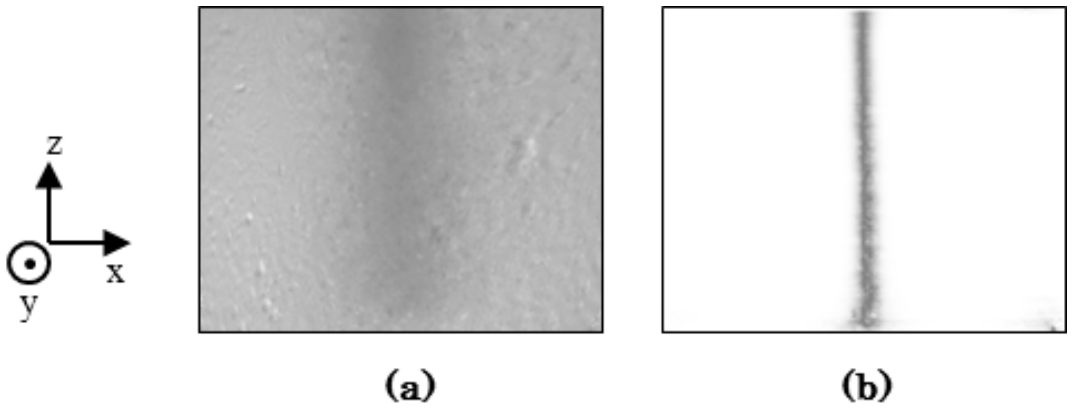

Fig. 5.11. Observed and deconvoluted images of absorber at 0-deg orientation: (a) observed image (b) result using the proposed technique.

Figure 5.12 shows the observed transillumination image and the result of the PSF deconvolution. In this case, the absorbing post was parallel to the observation surface, and it is able to use the PSF with a single depth. The observed image was degraded severely by the effect of strong scattering. Its effect was greatly suppressed when using the proposed technique.

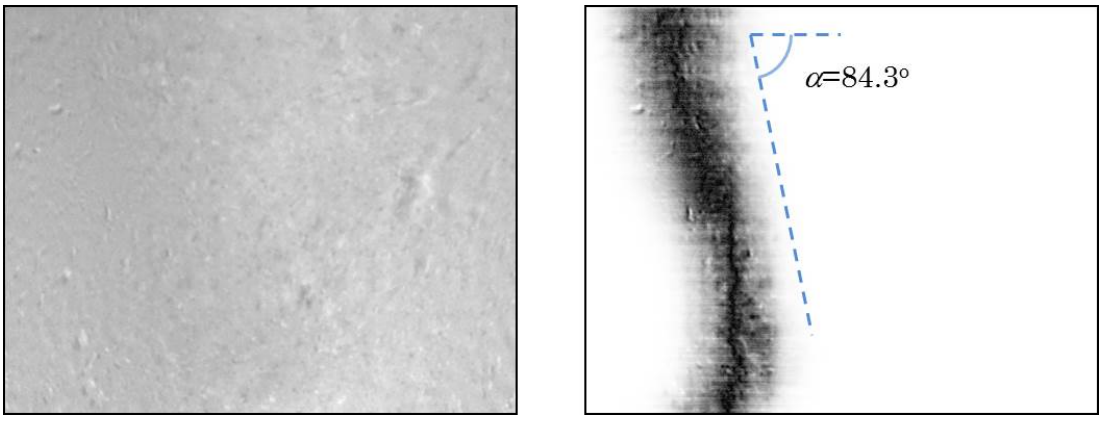

Fig. 5.12. Observed and deconvoluted images of absorber: (a) observed image (contrast and sharpness are 0.33 and 0.030), (b) deconvoluted image (contrast and sharpness are 0.82 and 0.61).

Figures 5.13 and 5.14 show the cross-sectional images reconstructed from the observed and deconvoluted transillumination images. With the observed images, the position of the absorber was difficult to identify in cross-sectional images. They became clearly identifiable using the proposed technique. The center of the absorber was estimated in the cross-sectional images at 10 different heights. The estimation errors of the center varied 1.35–2.72% along the vertical axis.

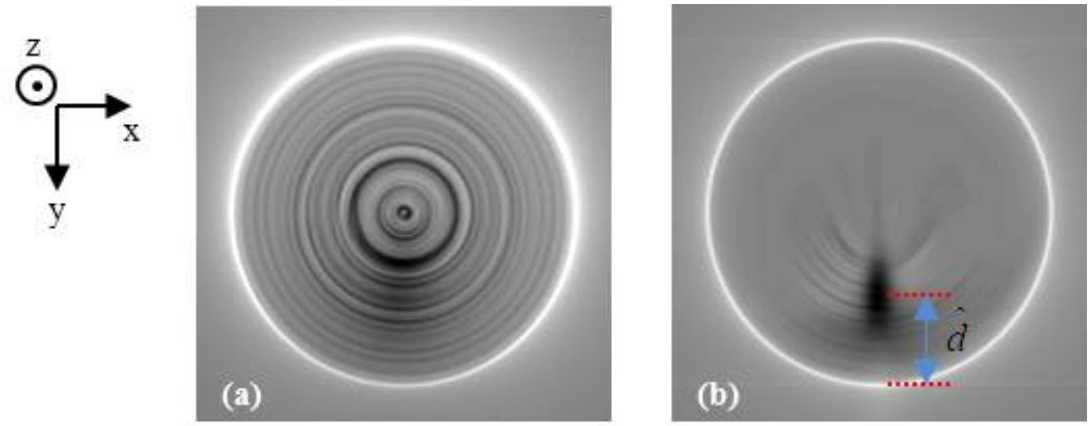

Fig. 5.13. CT image at the top of the absorber: (a) from observed images, (b) from deconvoluted images. Depth of estimated absorber center ($\hat{d}$) was 9.29 mm for true depth 9.55 mm.

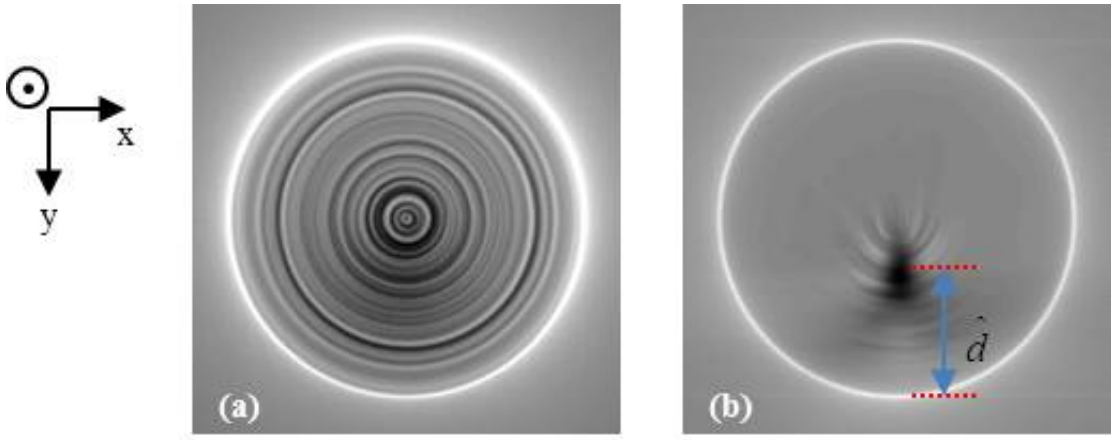

Fig. 5.14. CT image at the bottom of the absorber: (a) from observed images, (b) from deconvoluted images. Depth of estimated absorber center ($\hat{d}$) was 12.4 mm for true depth 12.6 mm.

Figure 5.15 shows the result of 3D reconstruction. Using the proposed technique, the absorbing structure was reconstructed clearly in the heterogeneous animal tissue

(chicken breast meat), as well.

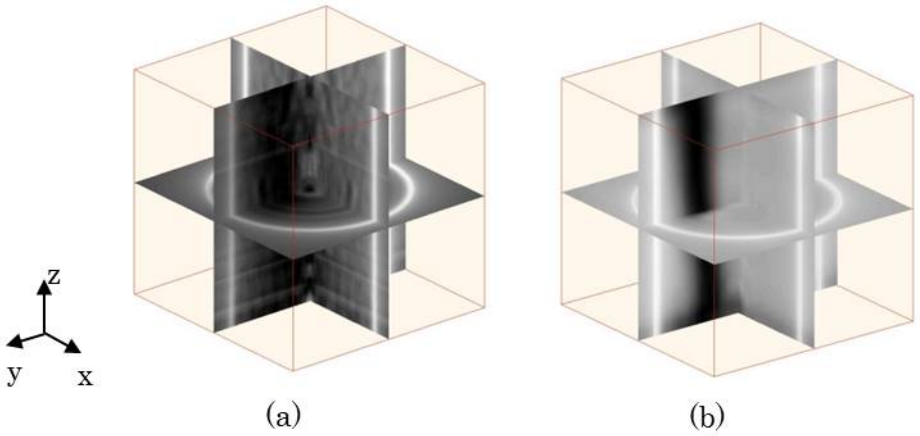

Fig. 5.15. 3D Reconstruction of absorber in animal tissue: (a) from observed images, (b) from deconvoluted images.

Figure 5.16 shows the rendering images of the observed data and the deconvoluted data with common threshold value. The scattering effect was suppressed efficiently, and the absorbing objects were visualized.

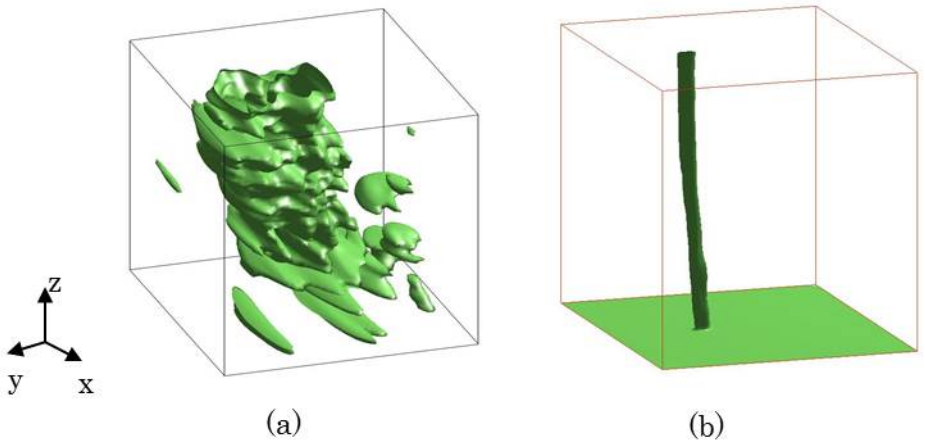

Fig. 5.16. 3D Reconstruction of absorber in animal tissue using iso-surface rendering technique with a common single threshold value: (a) from observed images, (b) from deconvoluted images.

5.3 Conclusion

In order to verify the applicability of 3D reconstruction from transillumination images, the experiments with known-structure in tissue-equivalent phantom and animal-tissue were performed and evaluated.

The scattering effect in transillumination images was effectively suppressed using the proposed scattering suppression technique. The PSFs with known different depths were applied to a transillumination image, and horizontal intensity profiles were extracted at the proper vertical heights in the improved image obtained by the proper PSF with the correct depth. These horizontal intensity profiles were obtained from different circumferential orientations. The cross-sectional image was reconstructed using the filtered back-projection algorithm. Finally, the cross-sectional images were piled up along the vertical axis and reconstructed the 3D structure.

The applicability and the effectiveness were confirmed in both experiments. The structure can be reconstructed properly in 3D image. The reconstruction error was less than 3% came from the random error.

Chapter 6
3D reconstruction of the unknown-structure transillumination images [6.1]

As shown in the previous chapter, the blurring effect of scattering in transillumination images can be effectively suppressed and the 3D image of absorbing structure in a turbid medium can be reconstructed. Therefore, this technique is powerful when examining a known discrete structure such as that described in the preceding chapter. However, the structure is often unknown and not as simple as described above. The transillumination image is the integration of all the absorbing distribution in different depths with different blurring. Therefore, the scattering suppression with the PSF at a single depth is not effective for such a case. The usefulness of the proposed method would be expanded greatly if this technique were able to apply to the object with unknown structure. To overcome this problem, a novel technique to reconstruct 3D image for unknown-structure was developed and will be described in this chapter. The effectiveness of this technique was examined in simulation and experiment.

6.1 3D reconstruction for unknown-structure transillumination images

To overcome the problem mentioned above, a new technique was developed to reconstruct 3D image of unknown-structure from the blurred transillumination images using the depth-dependent PSF. Figure 6.1 shows the condition of a transillumination image of two absorbing objects at different depth in a turbid medium. The observed image appears as shown in Fig. 6.1(b). The absorption profile in the observed intensity is shown in the lower part of Fig. 6.1(b).

The developed technique consists of two processes. The principle is shown in one dimension for simplicity instead of two dimensions. The first process is the

deconvolution of a transillumination image with the PSFs at varying depths. Figure 6.2 presents this process. All the deconvoluted data are summed to produce the projection data for the filtered back-projection process in the optical CT reconstruction. In this way, the true profile of the absorbing object is included in the projection data. In practice, two-dimensional PSFs at different depths are applied to a 2D transillumination image. The deconvoluted images are summed up to produce a projection image for 3D-optical CT reconstruction.

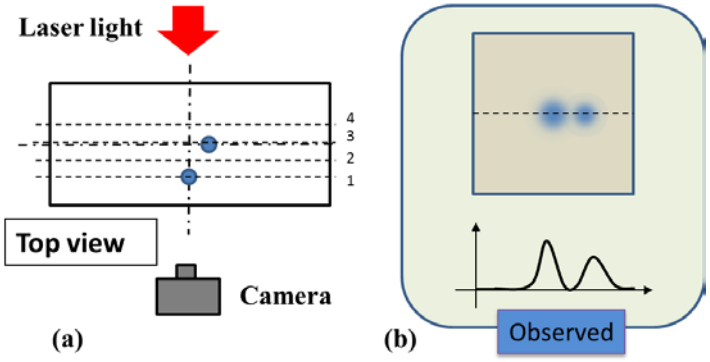

Fig. 6.1. Two absorbing objects in turbid medium: (a) top view of observing condition, (b) observed transillumination image and absorption profile along the dashed line.

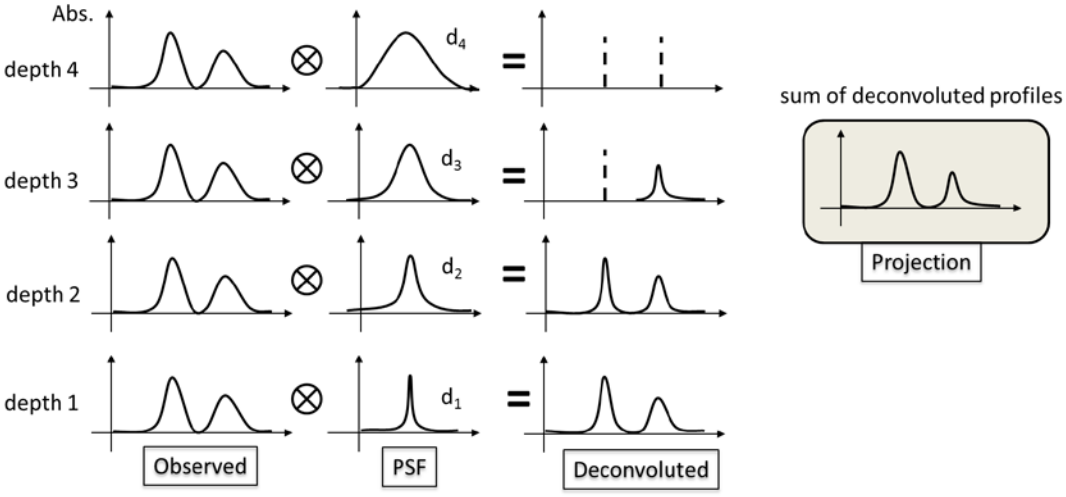

Fig. 6.2. Absorption profiles before and after the deconvolution with PSFs at different depths. The projection is obtained as a sum of the deconvoluted data with the PSFs at different depths. Profile of projection for cross-sectional reconstruction is shown in upper right corner. ⊗ denotes the deconvolution operation.

This process can be written as

$$P(x,z\,|\,\theta)=\sum_{i=1}^{n}\int A(x,y,z\,|\,\theta)dy\otimes PSF(x,z\,|\,d_i), \qquad (6.1)$$

where P, A, and PSF respectively represent the functions of projection, blurred absorption distribution and point spread function. $\otimes$ denotes the deconvolution operation. (x,y,z), θ and d_i respectively represent the Cartesian coordinates, orientation of observation, and the i-th depth, respectively. i = 1, 2 …. n, and n is the number of different depths.

As shown in Fig. 6.2, the sum of the deconvoluted profiles includes erroneous profiles as well as the true profile. They are the results of the deconvolution with the PSFs at shallower depths than the true depths of the absorbing object. The effects of the erroneous profiles are suppressed in the second process of the developed technique.

In the second process, a cross-sectional image was reconstructed first from the projection data or the sum of the deconvoluted profiles. This cross-sectional image from the deconvoluted profiles is better than that from the observed profiles, because the profiles at the deeper depths than the true depth were effectively erased by the deconvolution operation as shown in Fig. 6.3. In this improved cross-sectional image, the absorption profiles were sampled at the same depths as those of the PSFs used in the first process. This profile was called an erasing template, $E(x,z\,|\,\theta,d_i)$. Then, these profiles as the templates were multiplied to erase the unnecessary parts of the deconvoluted profiles. Figure 6.3 portrays this operation. Consequently, the profiles only at the true depths were emphasized. Then they are summed up to make a new improved projection. This process can be written as

$$P_{new}(x,z\,|\,\theta)=\sum_{i=1}^{n}\sqrt{\left[\int A(x,y,z\,|\,\theta)dy\otimes PSF(x,z\,|\,d_i)\right]E(x,z\,|\,\theta,d_i)}, \quad (6.2)$$

where P_{new}, A, PSF, and E respectively show the functions of new projection, blurred absorption distribution, point spread function, and the erasing template.

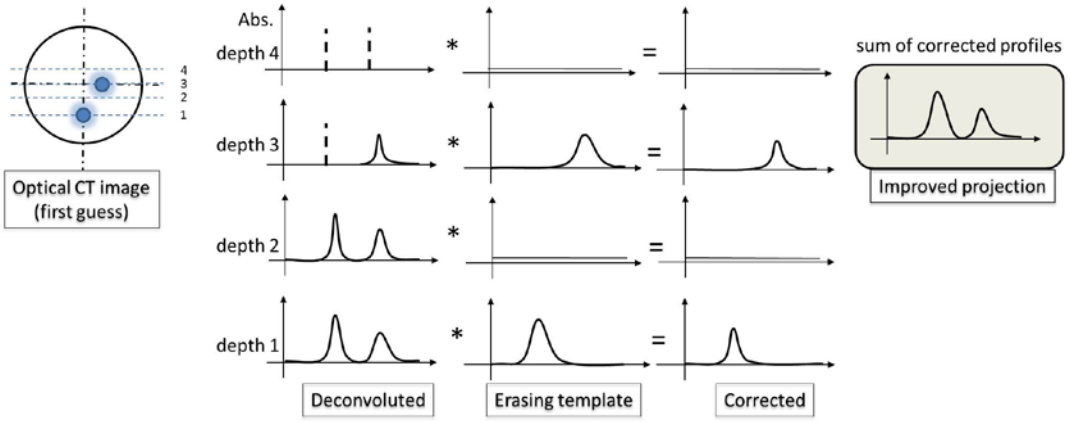

Fig. 6.3. Principle to suppress erroneous absorption distribution. Erroneous parts are suppressed by multiplying erasing templates obtained from the original cross-sectional image. New projection image is constructed as a sum of the corrected images. * denotes the multiplication operation.

Using the new projection image $P_{new}(x,z|\theta)$, the improved 3D image could be reconstructed with the filtered back-projection algorithm. This process can be repeated until a satisfactory result is obtained.

The effectiveness of the proposed technique was verified in computer simulation with the model shown in Fig. 6.4(a). The effect of scattering was suppressed by the proposed technique (number of different depths, $n = 300$) with a single step of the template erasure process as shown in Figs. 6.4(b)–(d).

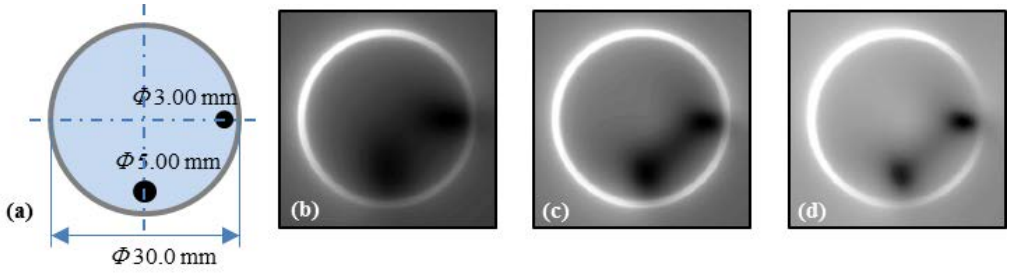

Fig. 6.4. Result of proposed technique in simulation: (a) simulation model ($\mu_s' = 1.00$ /mm, $\mu_a = 0.00536$ /mm), (b) cross-sectional image of two objects in scattering medium, (c) result from projection of Eq. (6.1), (d) result from projection of Eq. (6.2).

6.2 Validation of the proposed technique in experiment

The feasibility of the proposed technique, described in previous chapter, was examined in an experiment. Figure 6.5 presents a schematic of the experimental system to obtain transillumination images of a tissue-equivalent phantom. As scattering medium, Intralipid suspension (Fresenius Kabi AG) and black ink (INK-30-B; Pilot Corp.) were mixed with distilled water to produce a tissue-equivalent medium (μ_s' =1.00 /mm, μ_a = 0.01 /mm). As an absorbing structure, three black-painted objects as shown in Figures 6.6(a) and 6.7(a) were used to simulate the high-absorbing structure in mouse body, such as kidneys and a spleen.

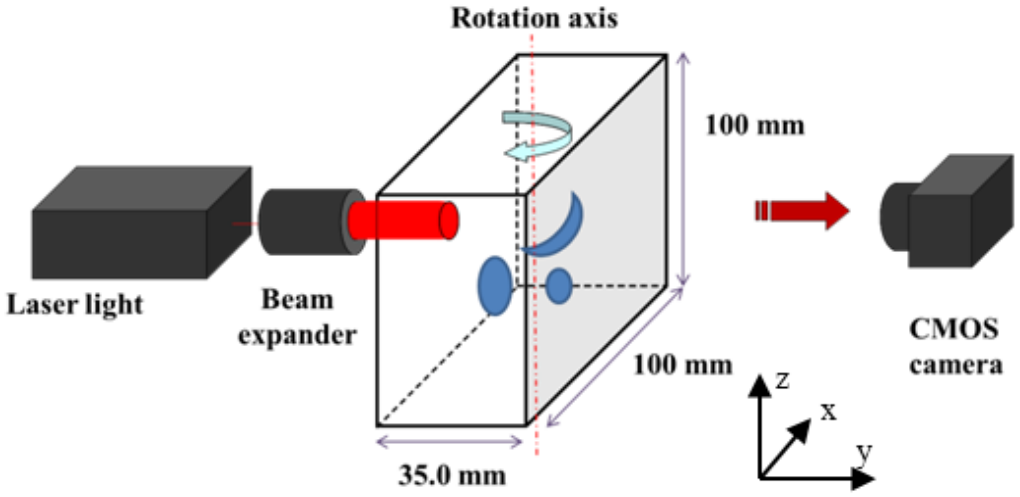

Fig. 6.5. Experimental setup with phantom.

The absorbing structure was placed at the center of an acrylic container (35.0 × 100 × 100 mm^3) filled with scattering medium. The phantom was irradiated with the NIR light from a laser (Ti:Sapphire, 850 nm wavelength) through a beam expander for homogeneous illumination. The image was captured using a cooled CMOS camera (C11440-10C; Hamamatsu Photonics K.K.) oriented toward the opposite face of the phantom to the light incident side. This recording was repeated while rotating the absorbing structure around the rotation axis using a mechanical rotation system.

Figures 6.6(a) and 6.7(a) respectively show the observed image of the absorbing structure in clear medium at 0 degree and 90 degree. Figures 6.6(b) and 6.7(b) show the observed image of the absorbing structure in scattering medium. Figures 6.6(c) and 6.7(c) show the result of the process described in section 6.1. The proposed technique was applied with the number of different depths $n = 350$ and with a single step of the template erasure process. The scattering effect was suppressed efficiently, and the absorbing objects were visualized.

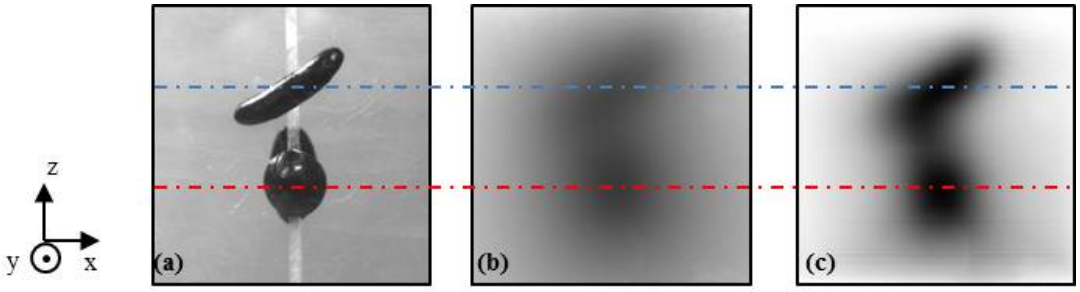

Fig. 6.6. Scattering suppression in transillumination imaging at 0-deg orientation: (a) observed image in clear medium, (b) observed image in scattering medium, (c) result using the proposed technique.

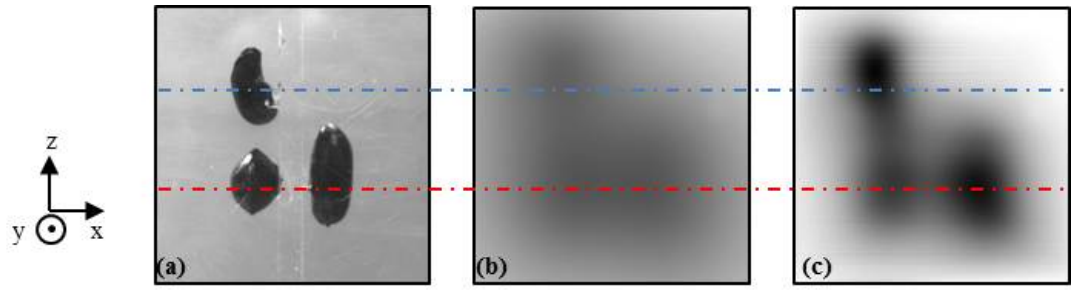

Fig. 6.7. Scattering suppression in transillumination imaging at 90-deg orientation: (a) observed image in clear medium, (b) observed image in scattering medium, (c) result using the proposed technique.

Figures 6.8 and 6.9 show cross sectional images at the height indicated by the dashed lines in Figs. 6.6 and 6.7. Figures 6.8(a), (b), (c) and 6.9(a), (b), (c) are the cross sectional images obtained from the data of Figs. 6.6(a), (b), (c) and 6.7(a), (b), (c), respectively.

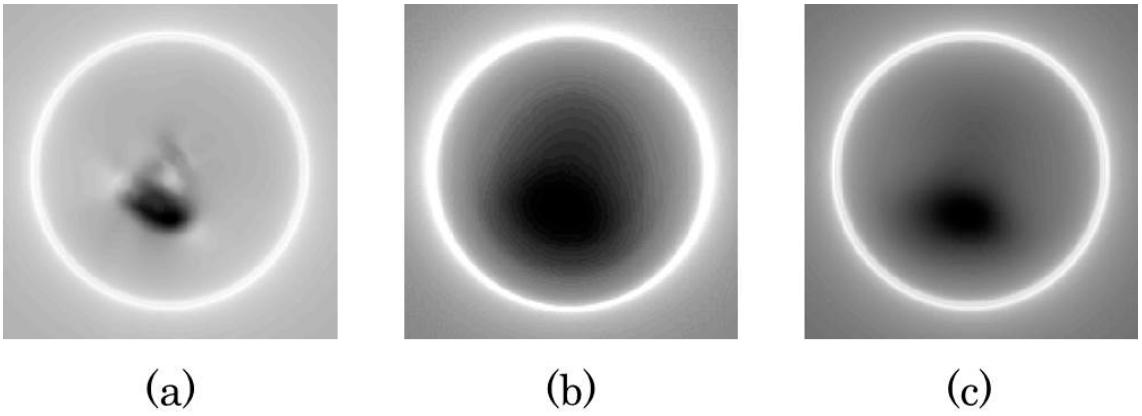

Fig. 6.8. Cross sectional images at the height indicated by the blue dashed line (upper) in Figs. 6.6 and 6.7: (a) from observed images in clear medium, (b) from observed images in scattering medium, (c) by proposed technique.

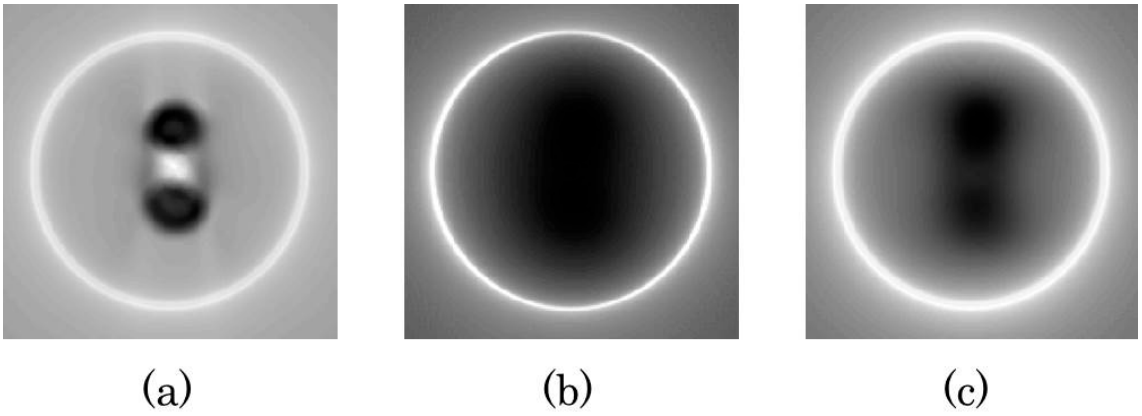

Fig. 6.9. Cross sectional images at the height indicated by the red dashed line (lower) in Figs. 6.6 and 6.7: (a) from observed images in clear medium, (b) from observed images in scattering medium, (c) by proposed technique.

Figure 6.10 shows results with two-level thresholds, which are common in all the figures. The internal structure, which is hardly seen in Fig. 6.10(b), became visible by the proposed technique.

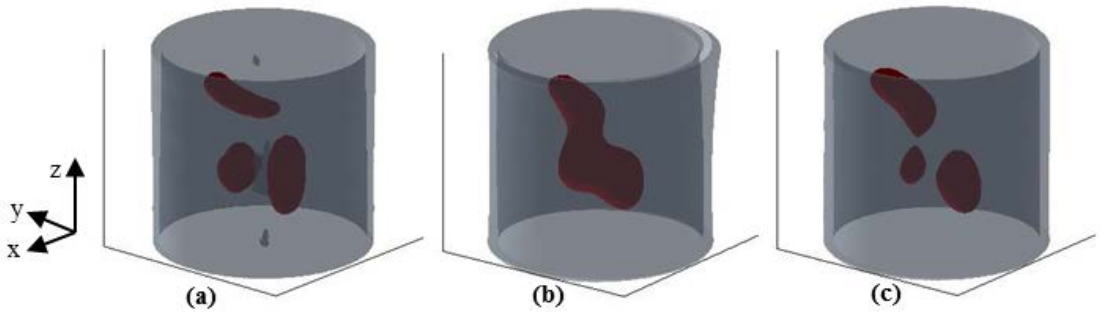

Fig. 6.10. 3D images reconstructed from transillumination images: (a) from observed image in clear medium, (b) from observed image in scattering medium, (c) result using the proposed technique.

6.3 Conclusion

In this chapter, a new 3D reconstruction technique from transillumination images for unknown-structure images using the depth-dependent PSF has developed. The erroneous in the deconvoluted images can be effectively suppressed. It provided the useful projection images for 3D reconstruction the unknown-structure. Using this technique, it is able to reconstruct the unknown-absorbing-structure in turbid medium. The technique can be applied in repetition until get the satisfaction result. The effectiveness of the proposed technique was confirmed in simulation and experiment.

This proposed technique opens a way in 3D reconstruction of unknown-structure in turbid medium. It can be applied in other application such as 3D bioluminescence or fluorescent imaging, biometrics, and so on.

In the next chapter, this proposed technique will be applied to reconstruct 3D image of high light-absorbing structure in small animal imaging.

Chapter 7
3D optical imaging of an animal body [7.1,7.2]

As shown in the previous chapters, the blurring effect of scattering in transillumination images can be effectively suppressed and the 3D image of light-absorbing structure in a turbid medium can be reconstructed. The proposed technique also expanded to the unknown-structure transillumination images. As the aims of this study, the proposed technique will be examined with small animal.

In practice, it is difficult to obtain transillumination image of small animal. The observed images were not useful or satisfaction due to the strong scattering in animal tissue and the size of experimental animal. The animal body was squeezed to reduce the size and thus the transillumiantion can be obtained. However, this technique does not allow obtaining full body 360° degrees; it is not useful for 3D imaging. To overcome this problem, with a view toward the realization of 3D optical whole-body small animal imaging, a practical technique had devised to obtain the transillumination image of small animal sensitively. The technique will be described in the first section of this chapter. Using this technique and the proposed technique in the previous chapter, it would be able to reconstruct the 3D image of high light-absorbing in animal body. To examine the applicability of the proposed technique to a living animal body, experiments were conducted with a mouse. The effectiveness of the proposed technique will be examined in this chapter.

7.1 Small animal transillumination imaging

Figure 7.1 shows the experimental setup. A female mouse (Slc:ICR, 20 week-old, 38.0 g) was anesthetized by the intraperitonial injection with 0.016 ml of sodium pentobarbital (Nembutal, 50 mg/ml, Abbott Lab.). The mouse was held in a cylindrical holder made of transparent acrylic resin. Laser light (Ti:Sapphire, 850 nm wavelength, 432 mW average power, 15.0 mm beam diameter) was illuminated from one side of the holder. The incident light power is safety for mouse. Then the image was recorded using a CMOS camera (C11440-10C; Hamamatsu Photonics K.K.) from another side.

The transillumination images were obtained while rotating the holder by rotation system. Using this technique, it would be able to reconstruct 3D image by using the filtered-back-projection algorithm if the projection images can be obtained.

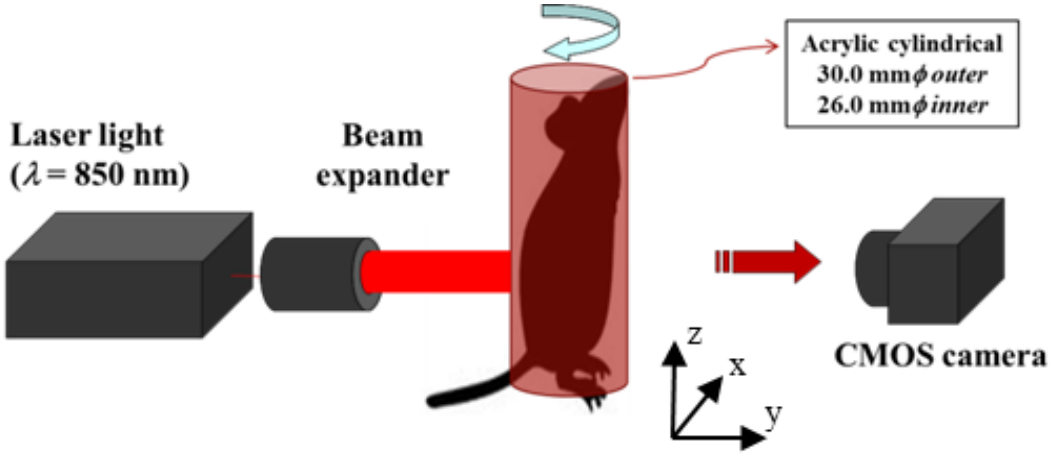

Fig. 7.1. Setup for experiment with living animal.

Special caution had to be taken to obtain transillumination images. Figure 7.2 presents an example of the transillumination image obtained with the experimental setup shown in Fig. 7.1. The surface of the mouse was lighted up, and the internal structure could hardly be seen because of the light guide effect of the acrylic cylinder. The incident light was guided through the cylindrical acrylic wall, subsequently illuminating a wide area of the body-surface of the mouse. To prevent this phenomenon, the cylinder was cut in half and installed light traps in the cylinder wall. Figure 7.3 presents the light trap structure.

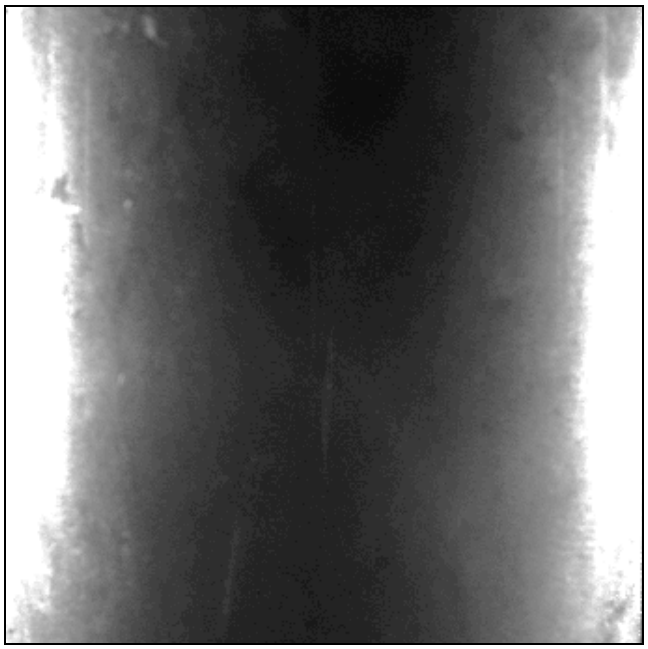

Fig. 7.2. Transillumination image obtained with the experimental setup shown in Fig. 7.1.

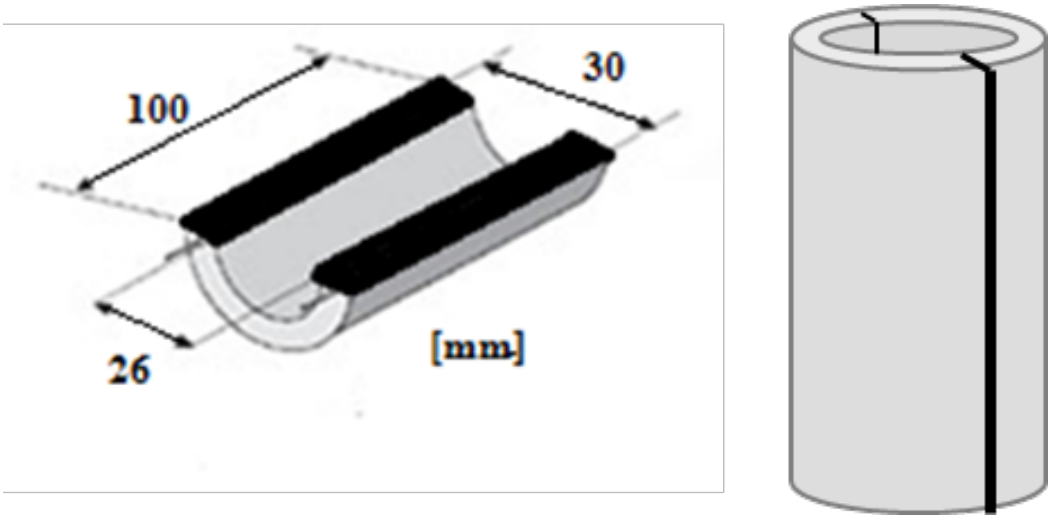

Fig. 7.3. Light trap structure.

Figure 7.4 shows an example of experimental setup with a mouse was fixed in the holder using light trap.

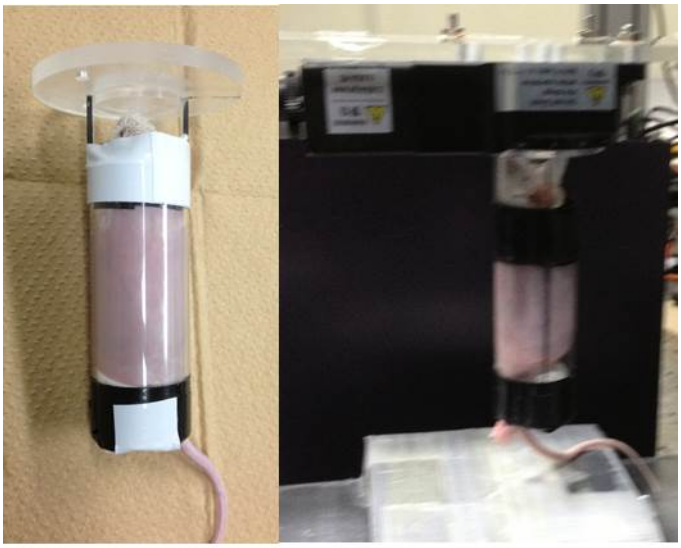

(a) (b)

Fig. 7.4. Experimental setup with mouse: (a) mouse was fixed in the holder with light trap, (b) mouse was fixed in the rotation stage.

Figure 7.5 shows the transillumination image obtained in the same experimental setup (Fig. 7.1) using the cylindrical mouse holder with light traps. By suppressing body-surface scattering, the internal structure came out in the image.

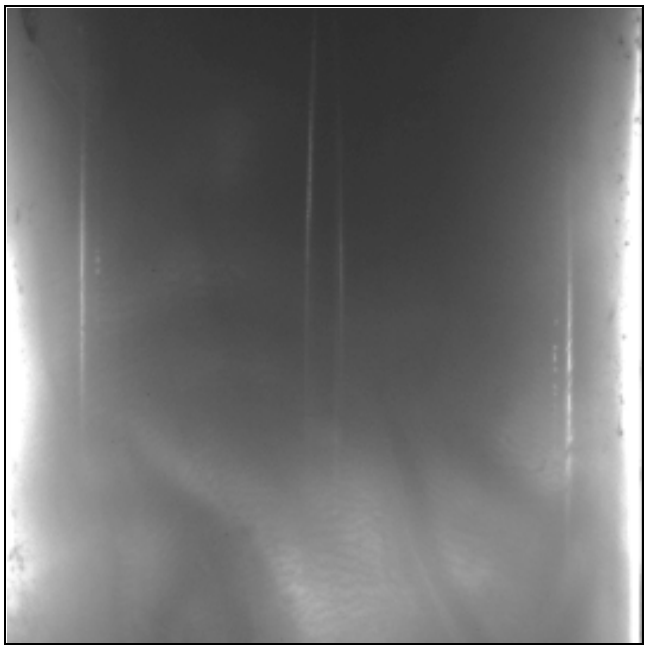

Fig. 7.5. Transillumination image obtained with the experimental setup shown in Fig. 7.1 using the light trap structure.

7.2 3D optical small animal imaging

The recording of a transillumination image was repeated while rotating the holder around the rotation axis shown in Fig. 7.1 using a mechanical rotation system. Figure 7.6 shows typical transillumination images obtained before and after the scattering suppression of the proposed technique. The internal light-absorbing structure became visible when using the proposed technique.

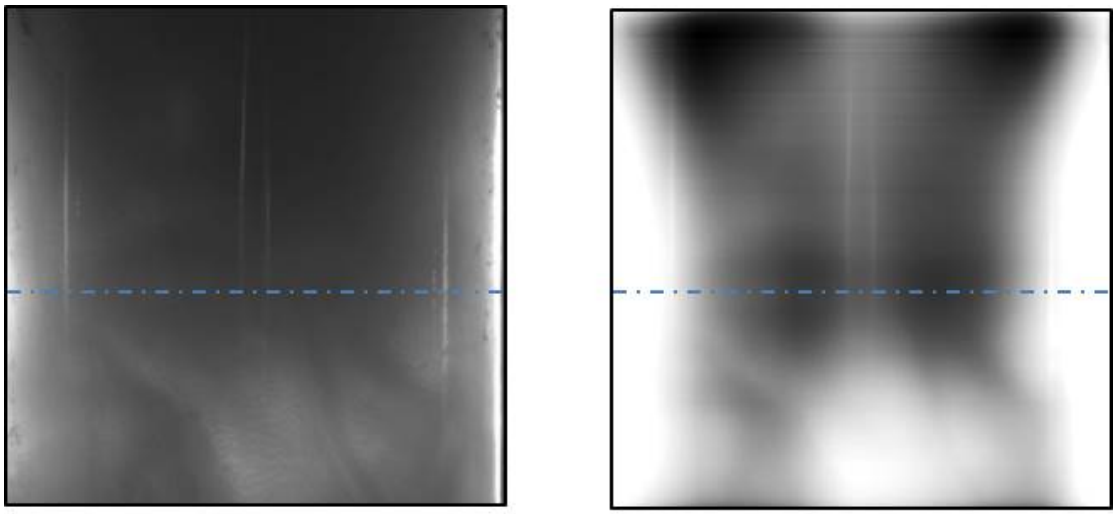

Fig. 7.6. Transillumination images of mouse abdomen: (a) observed image, (b) deconvoluted image with PSF (μ_s' =1.5 /mm, μ_a =0.02 /mm).

From these transillumination images, the cross-sectional images were reconstructed using the proposed technique described in chapter 6. The proposed technique was applied with the number of different depths n = 350 and with a single step of the template erasure process.

Figure 7.7 shows cross sectional image at the height indicated with the dashed line in Fig. 7.6. Figure 7.7(a) is the result of filtered back-projection from the observed transillumination image. Figure 7.7(b) is the result of the proposed technique mentioned in chapter 6. The internal structure hardly seen in Fig. 7.7(a) came out in Fig. 7.7(b).

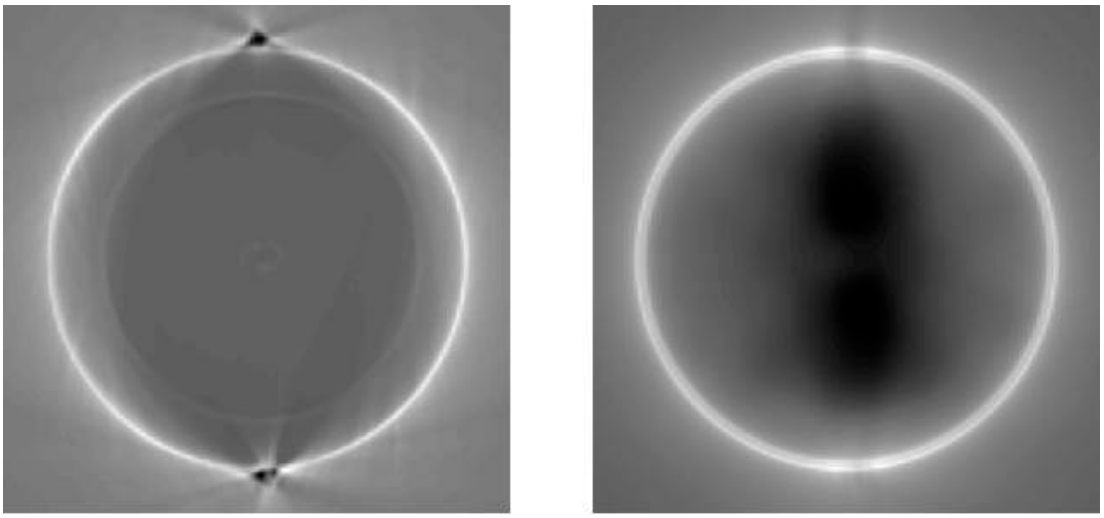

(a) (b)

Fig. 7.7. Cross sectional image reconstructed from transillumination images at the height indicated with the dashed line in Fig. 7.6: (a) from observed image, (b) by proposed technique.

These cross-sectional images were piled up vertically and a 3D image was constructed. Figure 7.8 presents results with three-level thresholds. Common thresholds were used for Figs. 7.8(a) and 7.8(b). The internal structure hardly seen in Fig. 7.8(a) became visible using the proposed technique. The high-absorption organs such as kidneys and the bottom parts of the liver were identified.

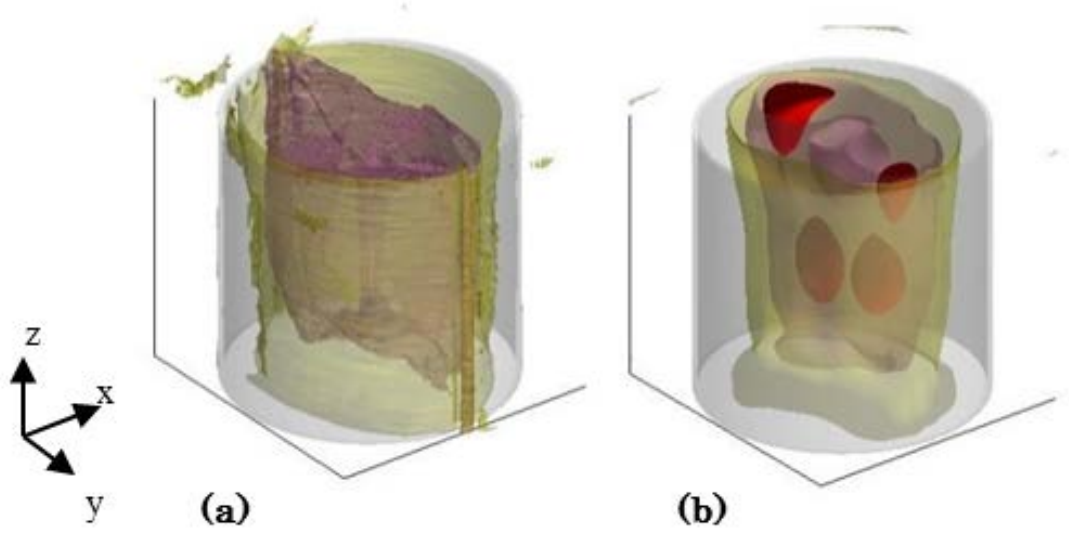

Fig. 7.8. 3D images reconstructed from transillumination images of mouse: (a) from observed images, (b) result using the proposed technique.

This experimental study verified the feasibility of the practical 3D imaging of the internal light-absorbing structure of a small animal.

7.3 Conclusion

In this chapter, the applicability of proposed technique to realize the 3D optical small animal imaging was examined. To overcome the problem in small animal transillumnation imaging, a new practical technique had developed using the light trap. Using this technique, the transllulimation of small animal body can be obtained sensitively. Using these transillumination images, the scattering suppression can be done by applying the proposed scattering suppression technique.

The improved images are useful to provide the projection images, as the result, the 3D image of high light-absorbing organs in animal body can be reconstructed.

The applicability of proposed technique was confirmed in experiment with a mouse. Using this technique, the high-absorption organs such as kidneys and a part of liver were visualized.

With a view toward the realization of 3D reconstruction from transillumination

images of animal body, the aims of this thesis were done. The proposed technique provided a way to realize the non-contact 3D optical tomography imaging for small animal optical tomography using NIR transillumination images with completely absence of matching fluids.

Besides that, the other studies were done to expand this technique for more practical use. The preliminary results of these studies will be present in the next chapter.

The animal experiment in this study was conducted in accordance with the guidelines [7.1] and with the approval of the review committee for animal experiments at Hokkaido University.

Chapter 8
Preliminary study for more practical use

In this chapter, the other studies to expand the applicability of the proposed technique will be introduced. There are three studies will be presented in this chapter:

1. Depth estimation technique for transillumination image,
2. Preliminary study for developing 3D physiological function imaging for small animal using transillumination image,
3. Scattering suppression technique for transillumination image using point spread function derived for cylindrical scattering medium shape.

8.1 Depth estimation technique for transillumination image

In previous chapters, the scattering effect could be effectively suppressed using the light-source PSF [8.1]. However, this PSF is depth dependence, so that the depth information is required in practical. This section will present a new technique for estimation depth of an absorber in 2D transillumination image.

8.1.1 Depth estimation technique

Because the optical properties of biological tissues are wavelength dependence, it is possible to obtain the images that are different by changing the wavelength of the light source or changing the concentration of the chromophores. The observed images of an absorber located in scattering medium at depth d with wavelength λ_i can be expressed by

$$Obs(\lambda_i, d) = Ori \times PSF(\lambda_i, d), \tag{8.1}$$

where $Obs(\lambda_i, d)$, Ori, and $PSF(\lambda_i, d)$, are respectively stand for the observed image, the original image, and the PSF calculated from Eq. (3.46). By convolving the

$Obs(\lambda_i, d)$ with the PSF for other wavelength, the convoluted images will be matched each other's, as given by

$$Obs(\lambda_1, d) \times PSF(\lambda_2, d) = Obs(\lambda_2, d) \times PSF(\lambda_1, d). \quad (8.2)$$

So that, the depth estimation can be done by changing the depth d for calculated PSF and finding the matched pair of the convoluted image. The process can be described by

$$Obs(\lambda_1, d_t) \times PSF(\lambda_2, d_i) = Ori \times PSF(\lambda_1, d_t) \times PSF(\lambda_2, d_i), \quad (8.3)$$

$$Obs(\lambda_2, d_t) \times PSF(\lambda_1, d_i) = Ori \times PSF(\lambda_2, d_t) \times PSF(\lambda_1, d_i), \quad (8.4)$$

where d_t and d_i are respectively stand for the true depth and the estimated depth. The two convoluted images will be matched when $d_i = d_t$. At each step, the convoluted images will be investigated by calculating the correlation and calculating the root-mean-square (RMS) difference. At the true depth, the RMS difference will be the minimum. Figure 8.1 shows an example of the convoluted images to illustrate this process.

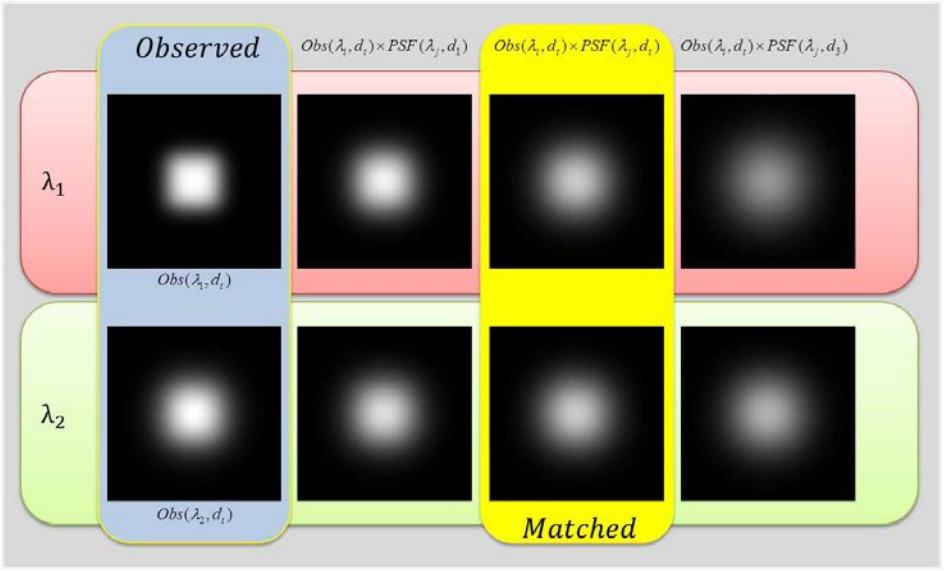

Fig. 8.1. Illustration of the proposed technique.

8.1.2 Validation of proposed technique in simulation

This section presents the validation of proposed technique in simulation. A square absorber (30.0 mm wide) was simulated to be placed at d_t=3.00, 5.00, and 7.00 mm deep from observation surface of a square scattering medium (100 mm wide). This absorber was at the center of the observed image.

The optical properties of scattering medium were given as $\mu_s'(\lambda_1) = \mu_s'(\lambda_2) = 1.00$ /mm, $\mu_a(\lambda_1) = 0.01$ /mm, and $\mu_a(\lambda_2) = 0.10$ /mm. The simulated observation images were obtained by convolving the original image with the corresponding PSF from Eq. (3.46). The depth estimation technique was performed with d_i varying from 1.00 to 10.0 mm. The step interval is 1.00 mm. Figures 8.2, 8.3, and 8.4 show the RMS difference at each depth. As shown in these figures, at the true depth, the RMS difference became the minimum.

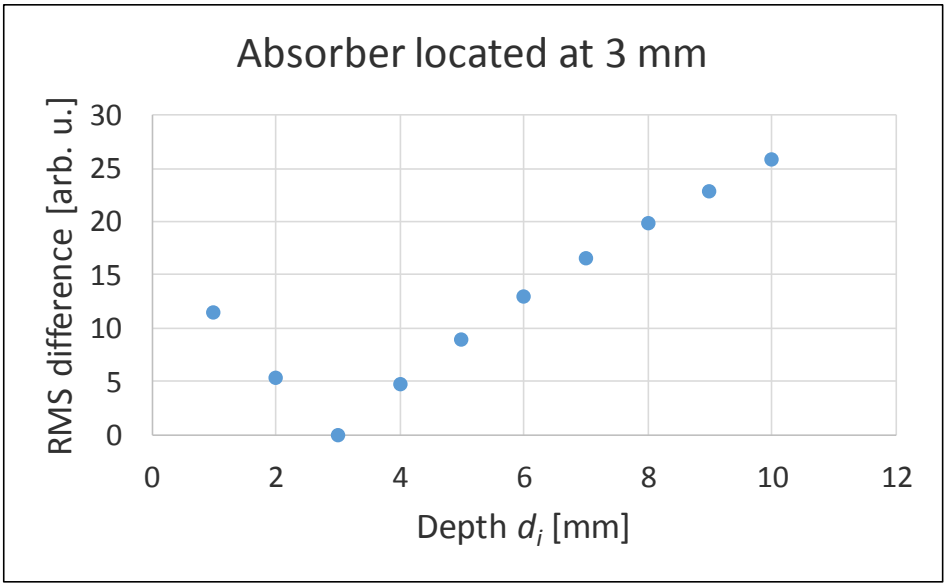

Fig. 8.2. Estimation depth of absorber (d_t=3.00 mm).

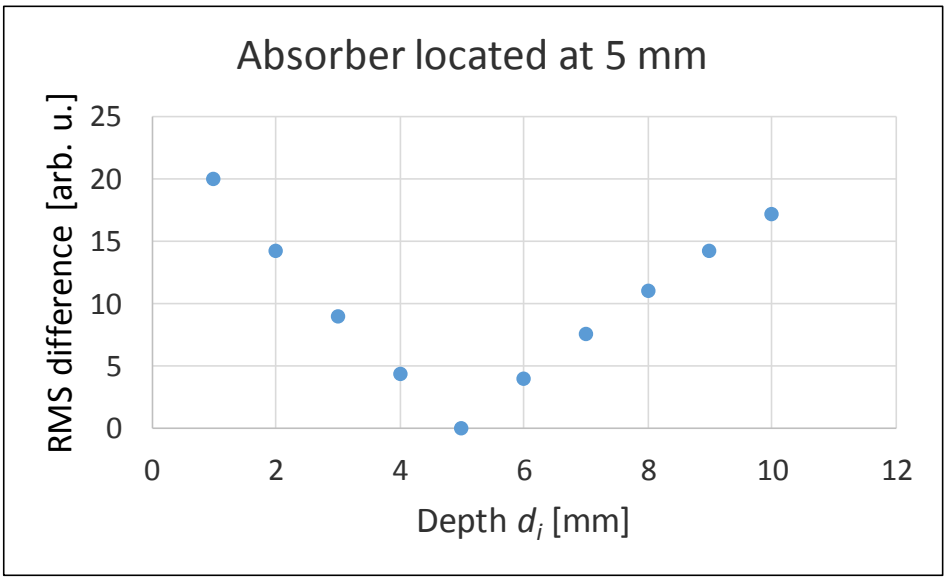

Fig. 8.3. Estimation depth of absorber (d_t =5.00 mm).

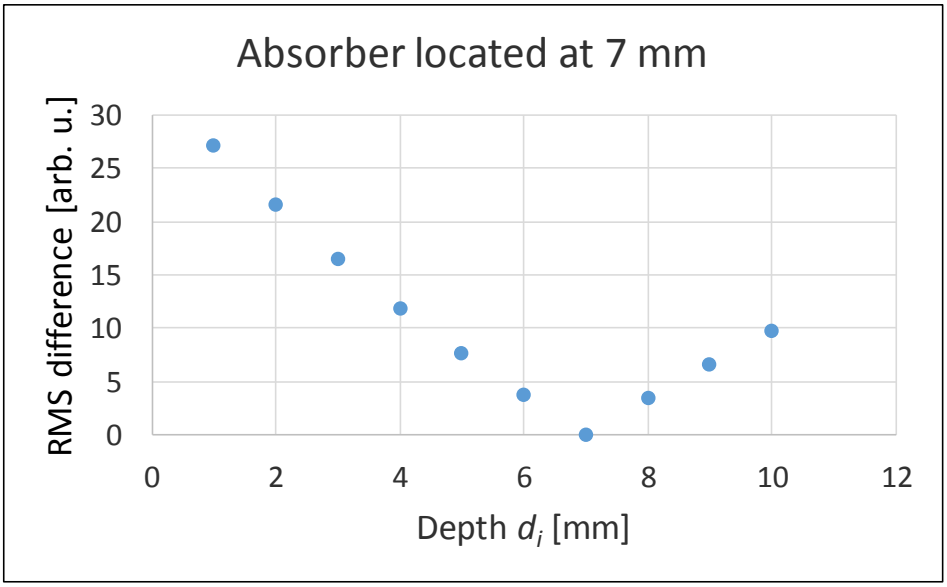

Fig. 8.4. Estimation depth of absorber (d_t =7.00 mm).

In the next simulation, the optical properties of scattering medium were given as $\mu_s'(\lambda_1) = 0.80$ /mm, $\mu_s'(\lambda_2) = 1.20$ /mm, $\mu_a(\lambda_1) = \mu_a(\lambda_2) = 0.00536$ /mm. The depth estimation technique was performed with d_i varying from 1.00 to 10.0 mm. The step

interval is 1.00 mm. Figures 8.5, 8.6, and 8.7 show the RMS difference at each depth. As shown in these figures, at the true depth, the RMS difference became the minimum.

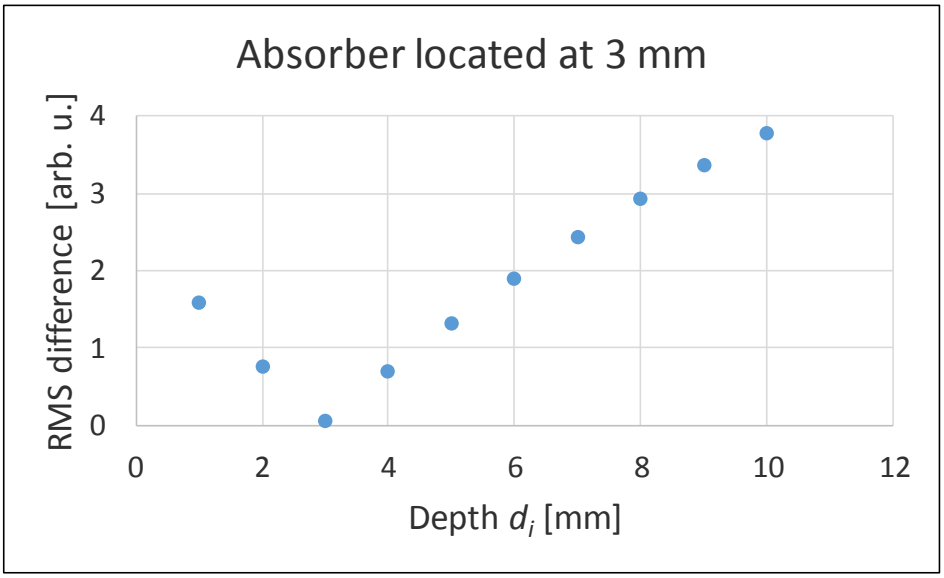

Fig. 8.5. Estimation depth of absorber (d_t =3.00 mm).

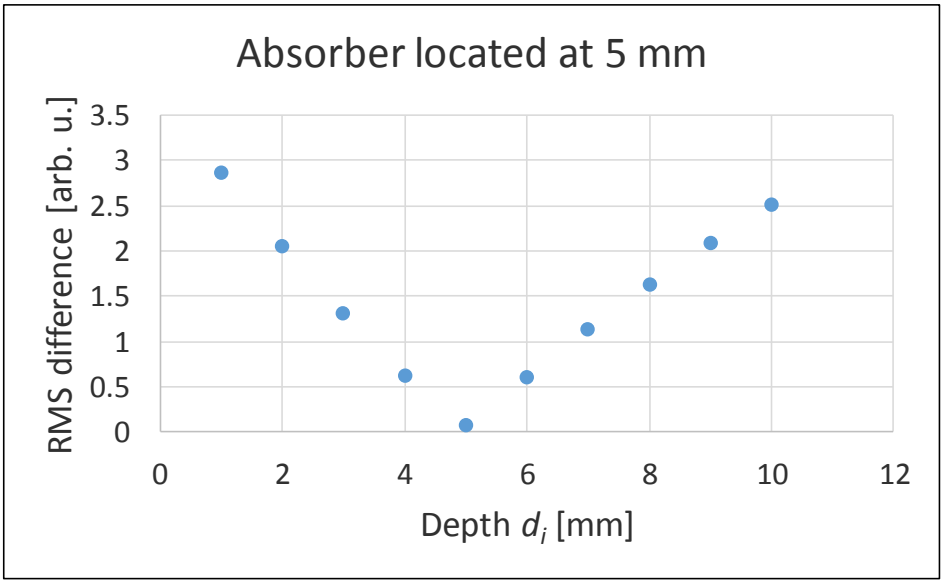

Fig. 8.6. Estimation depth of absorber (d_t =5.00 mm).

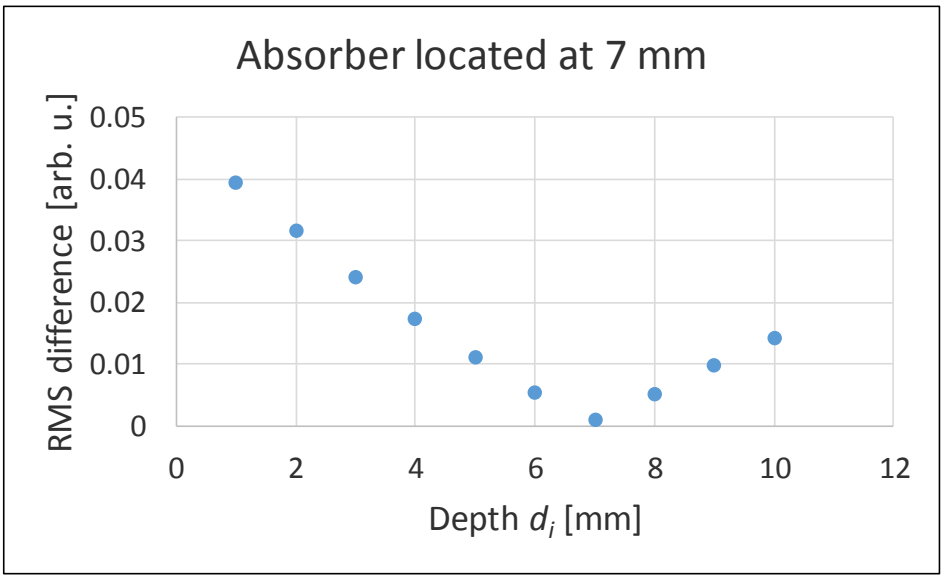

Fig. 8.7. Estimation depth of absorber (d_t =7.00 mm).

The results suggest that the proposed technique is valid. The effectiveness of the proposed technique was confirmed in simulation.

8.1.3 Validation in experiment with tissue-equivalent phantom

To verify the applicability of the proposed technique, the experiments with tissue-equivalent phantom were conducted. These experiments were performed same as the experimental conditions shown in Fig. 4.4. At this time, the wavelength of light source didn't change. The different conditions were made by changing the optical properties of scattering medium. The observed images were obtained when the absorber located at 4.00 and 6.00 mm.

The optical properties of scattering medium were given as $\mu_s'(\lambda_1) = \mu_s'(\lambda_2) = 1.00\,/\mathrm{mm}$, $\mu_a(\lambda_1) = 0.01/\mathrm{mm}$, and $\mu_a(\lambda_2) = 0.10\,/\mathrm{mm}$. Figures 8.8 and 8.9 show the RMS difference at each depth. As shown in these figures, at the true depth, the RMS difference became the minimum.

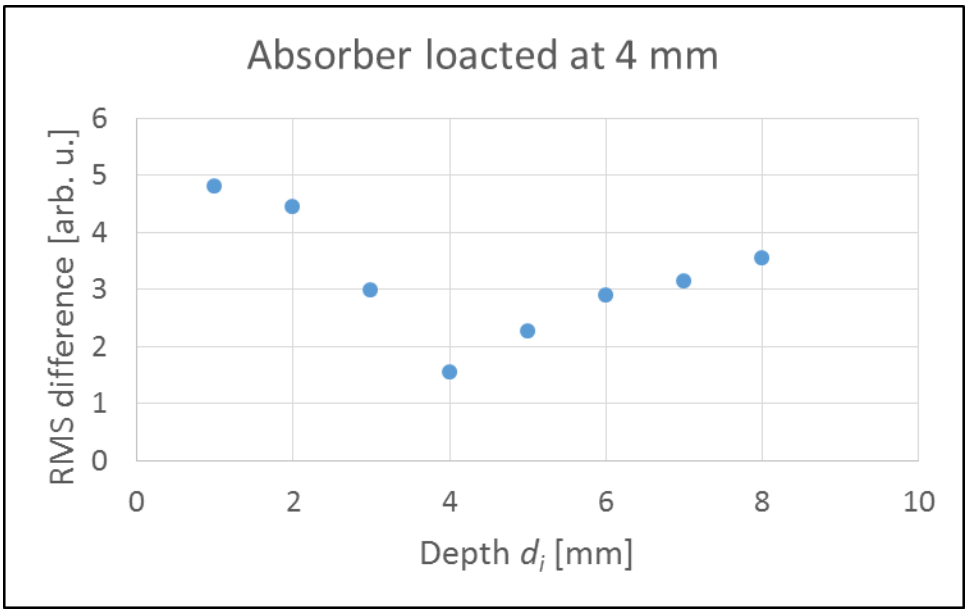

Fig. 8.8. Estimation depth of absorber (d_t =4.00 mm).

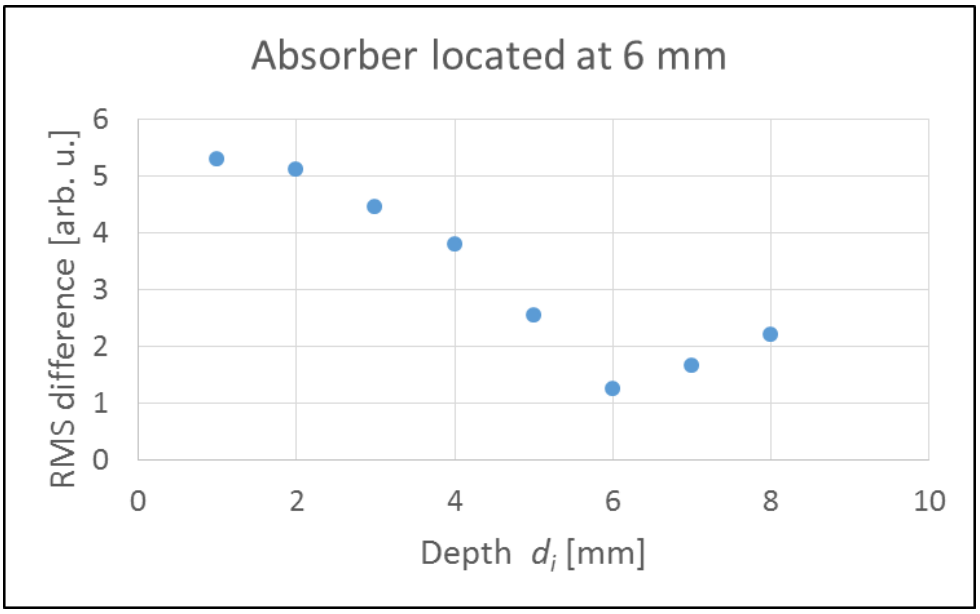

Fig. 8.9. Estimation depth of absorber (d_t =6.00 mm).

In the next simulation, the optical properties of scattering medium were given as $\mu_s'(\lambda_1) = 0.80$ /mm, $\mu_a(\lambda_1) = 0.05$ /mm, $\mu_s'(\lambda_2) = 1.00$ /mm $\mu_a(\lambda_2) = 0.01$ /mm. Figures 8.10 and 8.11 show the RMS difference at each depth. As shown in these figures, at the

true depth, the RMS difference became the minimum.

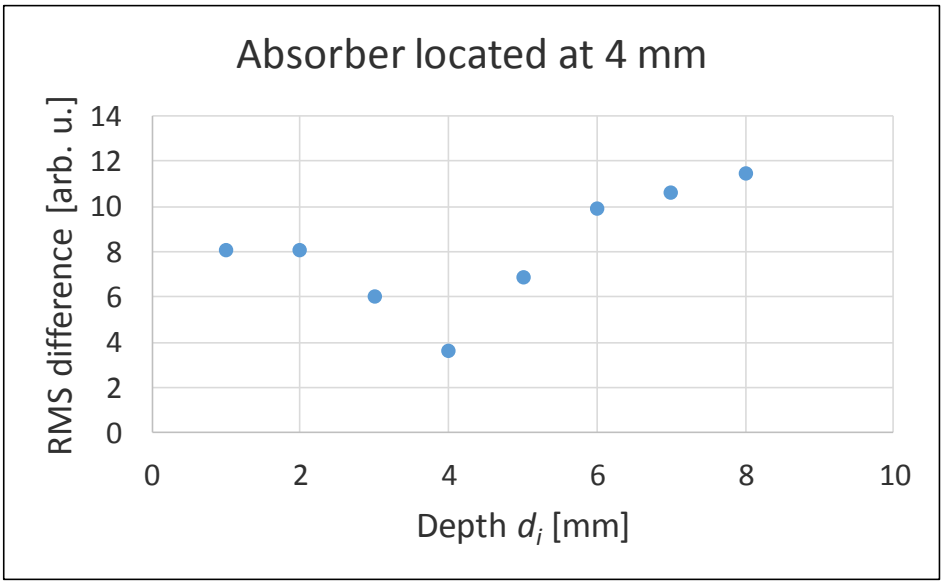

Fig. 8.10. Estimation depth of absorber (d_t =4.00 mm).

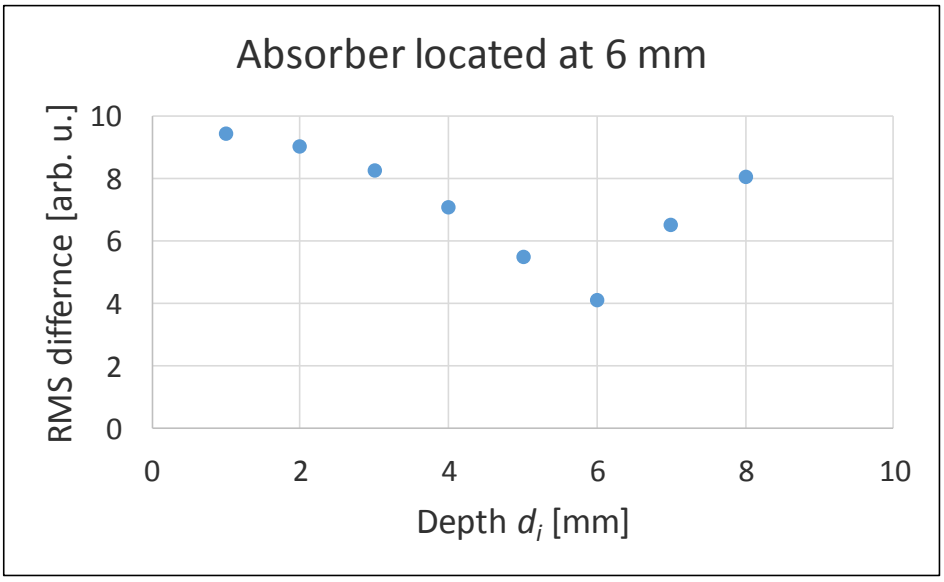

Fig. 8.11. Estimation depth of absorber (d_t =6.00 mm).

As shown in these figures, the estimation depth is correctly matched with the given

depth. The effectiveness of the proposed technique was also confirmed in experiment with tissue equivalent phantom.

Results presented in this section were equally contributed by Mr. Kohei Yamamoto, who was a master course student of my laboratory.

8.2 3D physiological function imaging for small animal using transillumination image

The optical computed tomography (optical CT) using near-infrared light (NIR) is a promising technique for noninvasive imaging of an animal body. Using the technique proposed in previous chapters, the scattering effect can be effectively suppressed in transillumination images and reconstructed the 3D structure with a common filtered back-projection algorithm.

In addition, there are different kinds of endogenous chromophores in an animal body. Their absorption spectra in the optical range are sensitive to the physiological change of the animal body. In the near-infrared region (700–1200 nm wavelength), hemoglobin has a characteristic absorption spectrum which is dependent on its redox state [8.2,8.3]. Therefore, the functional information inside the animal body can be obtained noninvasively by measuring the transmitted light [8.3]. By detecting the change of the absorption characteristics of animal body, the functional change inside the body can be detected in a two-dimensional (2D) transillumination image. Using the 2D images obtained in many different orientations, 3D physiological function imaging of animal body by transillumination could be expected. This section presents a preliminary result in animal experiment to show the feasibility of this technique.

8.2.1 Method and experimental setup

The experiment was performed same as the experiment in chapter 7. Figure 7.1 shows a schematic of the experimental system to obtain transillumination images of an animal body. A male mouse (Slc:ICR, 11 week-old, 38.4g) was anesthetized by the

intraperitonial injection with 0.016 ml of sodium pentobarbital (Nembutal, 50 mg/ml, Abbott Lab.). The mouse was held in a cylindrical holder made of transparent acrylic resin. Laser light (Ti:Sapphire, 760nm and 850 nm wavelength, 430 mW average power, 15 mm beam diameter) was illuminated from one side of the holder and the image was recorded with a cooled CMOS camera (C11440-10C, Hamamatsu Photonics K.K.) from another side. The incident light power is safety for mouse.

Figure 8.12 show the absorption spectra of oxyhemoglobin (HbO_2) and deoxyhemoglobin (Hb) in the near infrared region. The dashed lines indicate the selected wavelengths for experiment.

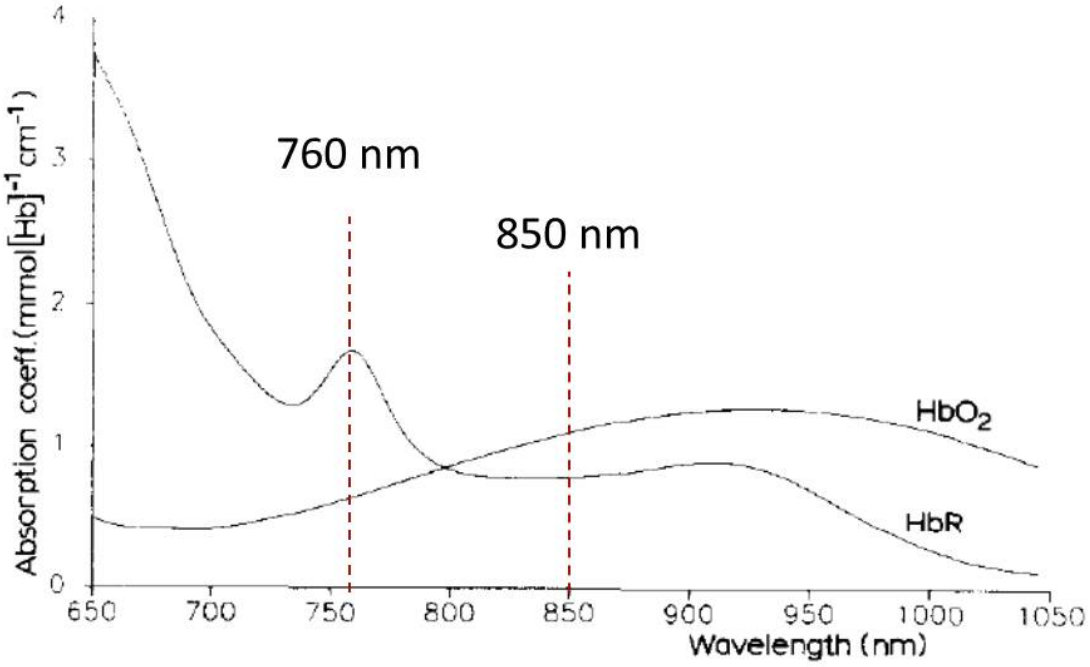

Fig. 8.12. Haemoglobin near IR absorption spectra from lysed, normal human blood obtained from fully oxygenated and fully deoxygenated haemoglobin. (Figure adapted from [8.2]).

The localized change in animal body was made by occluding the left or right blood vessel to make the blood circulation of the kidney asymmetric. Figure 8.13 shows an example how to make a restorable occlusion of the blood vessel. A line of thread was turned around the interlobar vessel and was drawn out through a fine plastic tube. By pulling or loosening the thread, the blood vessel was occluded and opened reversibly.

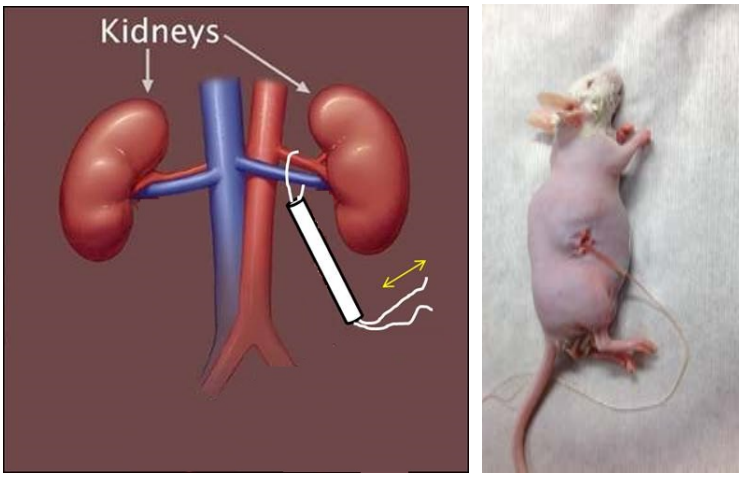

Fig. 8.13. Control of the circulation of the kidney.

8.2.2 Preliminary result in animal experiment

Figures 8.14 and 8.15 show the transillumination image using the wavelength 760 nm. As shown in these figure, the intensity distribution is darker in the Figs. 8.14(b) and 8.15(b) at the region where the thread presented, because the absorption coefficient changes by pulling the thread. While the circulation is stopped, the concentration of hemoglobin become higher. Therefore, the absorption coefficient is increased while using the wavelength 760 nm and decreased while using the wavelength 850 nm.

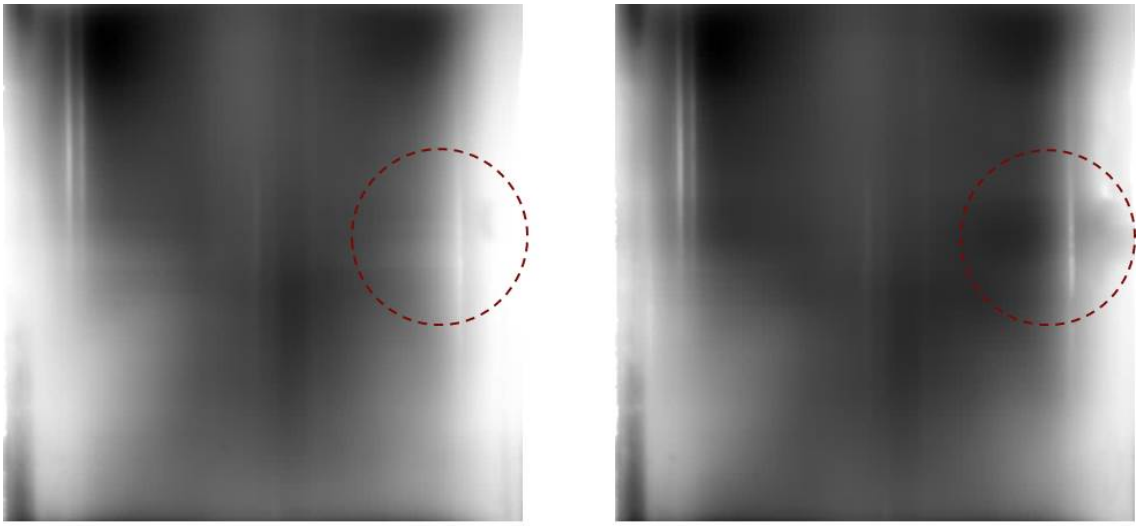

Fig. 8.14. Transillumination image of mouse's back using light source with 760 nm: (a). loosening the thread, (b). pulling the thread. Dashed red circle marked the region where the thread presented.

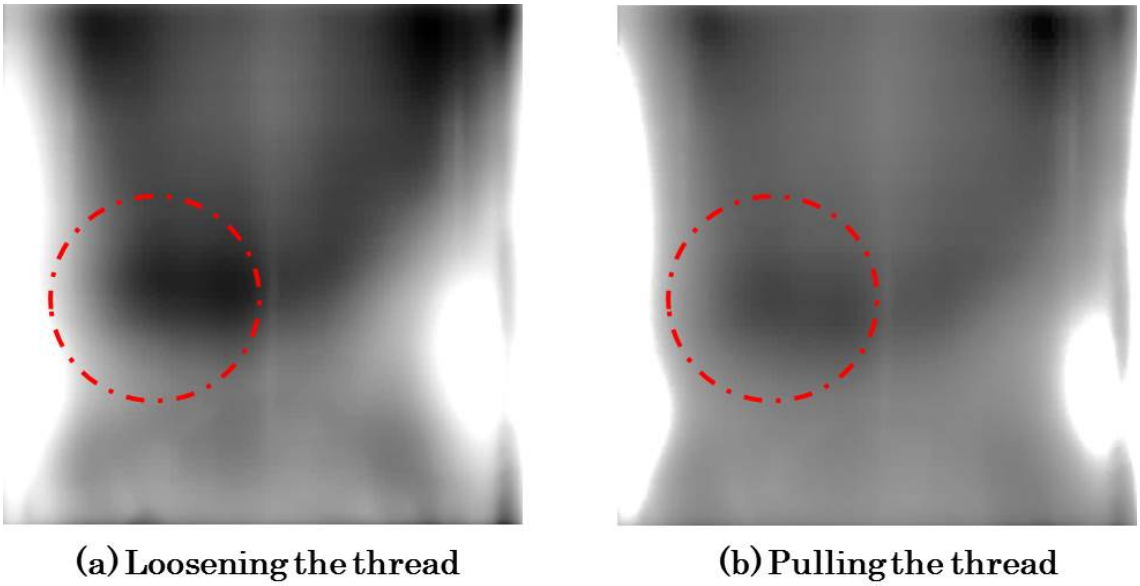

Fig. 8.15. Transillumination image of mouse's abdomen using light source with 850 nm: (a). loosening the thread, (b). pulling the thread. Dashed red circle marked the region where the thread presented.

By applying the technique mentioned in chapter 6, the cross-sectional images and 3D images were reconstructed from improved data. Figure 8.16 shows the cross-sectional

images at the height of kidneys while loosening and pulling the thread. As shown in Fig. 8.16, the region where the absorption coefficient increased can be vilsualized.

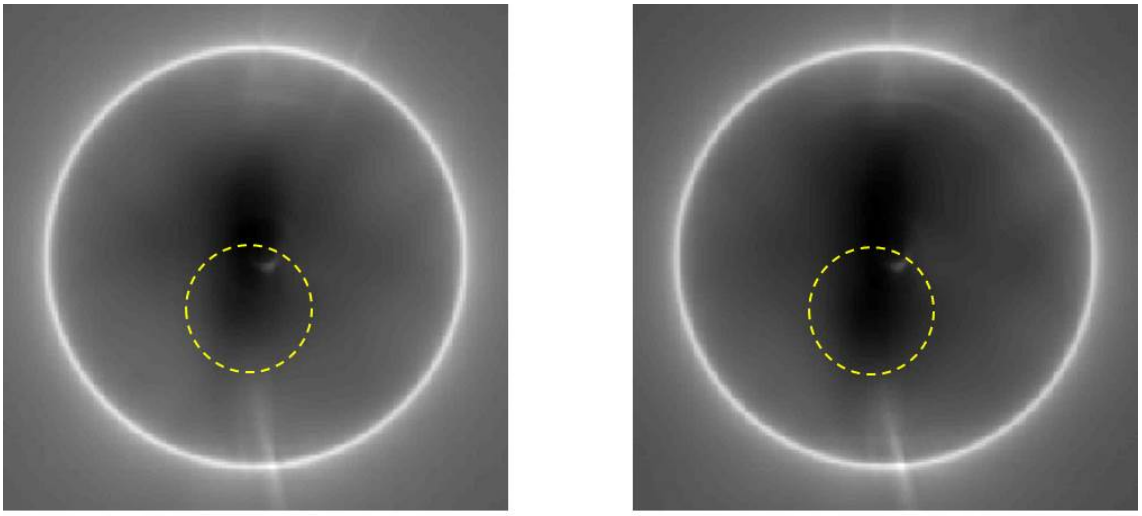

(a) Loosening the thread (b) Pulling the thread

Fig. 8.16. Cross-sectional image at the height of kidneys while using the wavelength 760 nm: (a). loosening the thread, (b). pulling the thread. Dashed yellow circle marked the region where the thread presented.

Figure 8.17 shows the cross-sectional images at the height of kidneys while loosening and pulling the thread. As shown in Fig. 8.17, the region where the absorption coefficient decreased can be visualized.

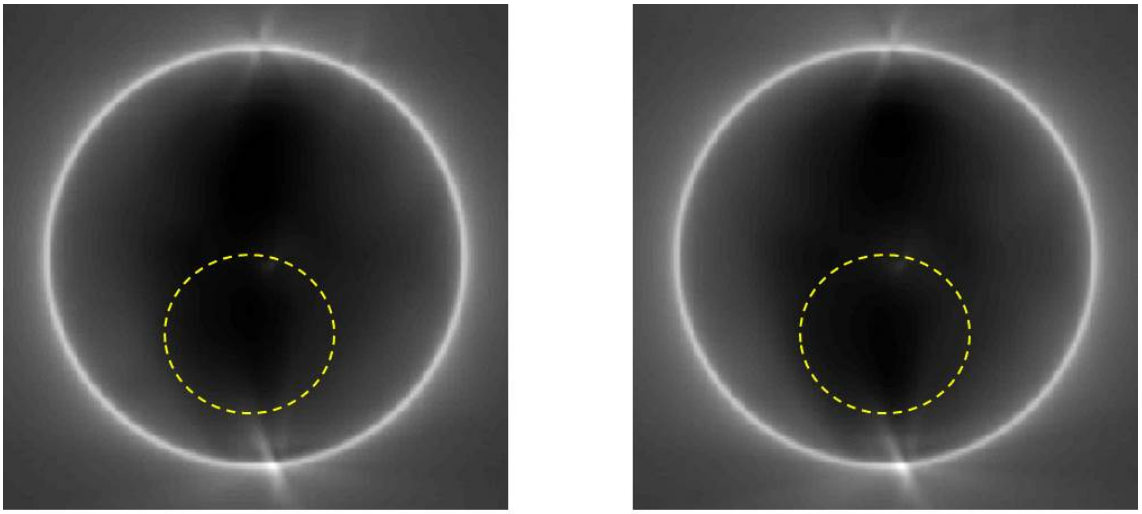

(a) Loosening the thread (b) Pulling the thread

Fig. 8.17. Cross-sectional image at the height of kidneys while using the wavelenght 850 nm: (a). loosening the thread, (b). pulling the thread. Dashed yellow circle marked the region where the thread presented.

These cross-sectional images were piled up to reconstruct the 3D image of absorbing structure in mouse body. Figures 8.18 and 8.19 respectively show the 3D image of absorbing structure in mouse body using the common threshold value with the wavelength 760 nm and with the wavelength 850 nm. As shown in these figures, the local changes inside mouse body can be visualized. The structure was not reconstructed in successful due to the bleeding inside mouse body. However, as the local changes can be reconstructed in successful, this result suggests the possibility to realize to 3D physiological function imaging for small animal using transillumination image. In future work, other experiment should be done with a good skill in operation and avoided to make the bleeding as much as possible.

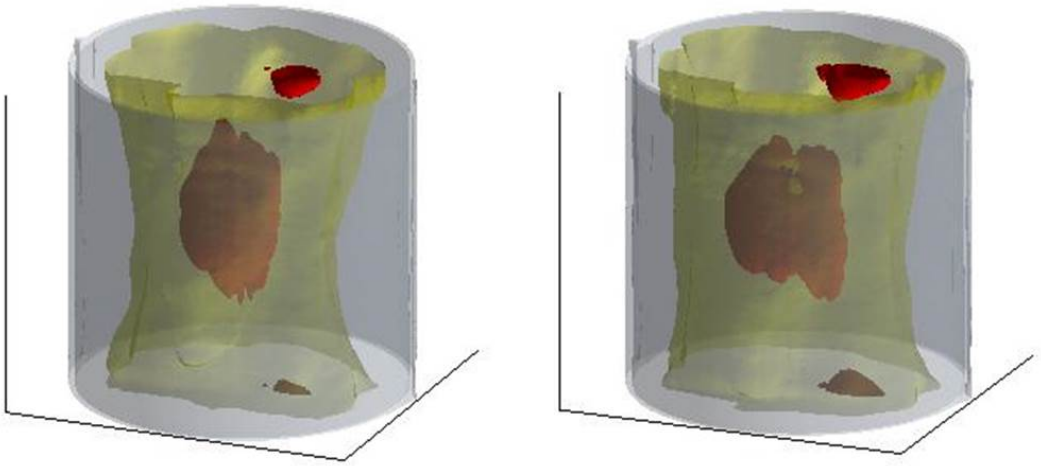

(a) Loosening the thread (b) Pulling the thread

Fig. 8.18. 3D image of absorbing structure in mouse body with the wavelength 760 nm: (a) lossening the thread, (b) pulling the thread. The right side of each figure is the region where the thread presented.

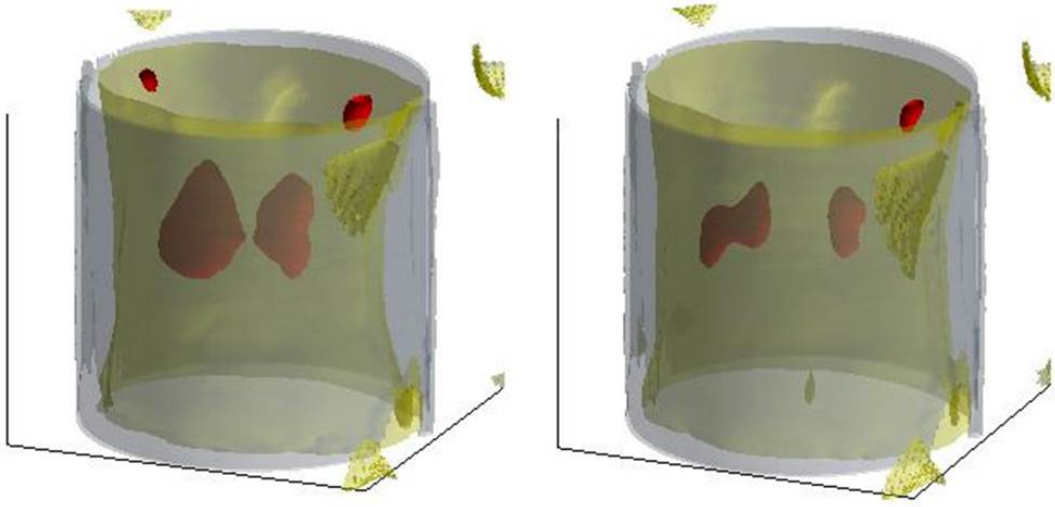

(a) Loosening the thread (b) Pulling the thread

Fig. 8.19. 3D image of absorbing structure in mouse body with the wavelength 850 nm: (a) loosening the thread, (b) pulling the thread. The right side of each figure is the region where the thread presented.

The animal experiment in this study was conducted in accordance with the guidelines [8.4] and with the approval of the review committee for animal experiments at Hokkaido University.

8.3 Scattering suppression technique for transillumination image using PSF derived for cylindrical scattering medium shape

8.3.1 Position-dependent PSF for cylindrical structure

The depth-dependent PSF as presented in chapter 3 was calculated on the assumption that the surface of scattering medium was flat. Figure 8.20 shows the observed image of a fluorescence object in the slab medium and in the cylindrical medium. In this case the fluorescence object is off-center and with cylindrical medium a shifted effect was occurred. Because of the asymmetry of scattering medium, the light source position was shifted to the side of thinner scattering medium.

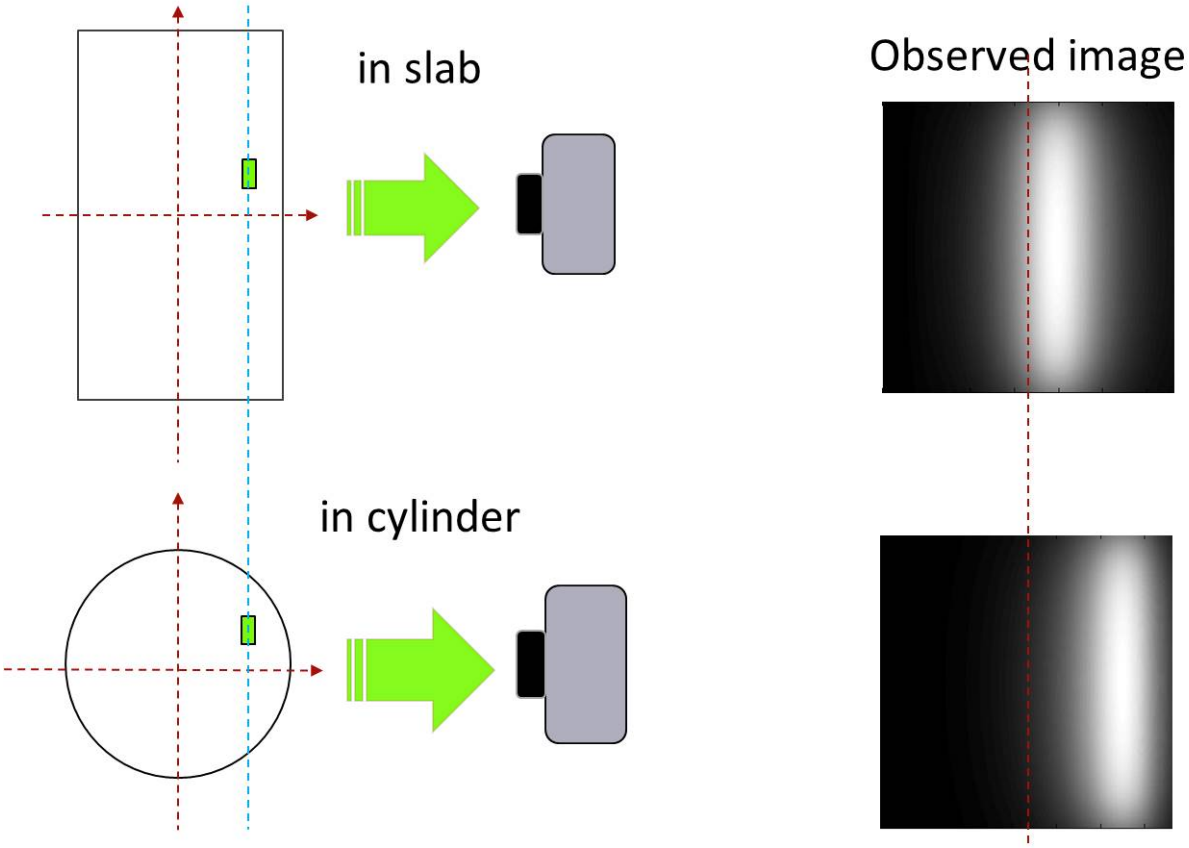

Fig. 8.20. Transillumination image of a fluorescence object in the slab medium and in the cylindrical medium.

To overcome this problem, the position-dependent PSF for the cylindrical scattering structure had derived in previous study of my research group [8.5,8.6]:

$$PSF(r,\theta,z|R,\Theta,Z)=\frac{3P_0}{(4\pi)^2}\left\{(\mu_s'+\mu_a)\cos\Theta+\left[\kappa_d+\frac{1}{(Z^2+d^2)^{1/2}}\right]\cos\alpha\times\frac{d}{(Z^2+d^2)^{1/2}}\right\}\frac{\exp\left[-\kappa_d(Z^2+d^2)^{1/2}\right]}{(Z^2+d^2)^{1/2}} \quad (8.5)$$

where the angle and the position parameters are illustrated in Fig. 8.21. (R,Θ,Z), P_0, μ_s' and μ_a are the vertical position, the optical power of a point source, the reduced scattering coefficient and the absorption coefficient, respectively. $\kappa_d=\sqrt{3\mu_a(\mu_s'+\mu_a)}$, $d=\sqrt{R^2+r^2-2Rr\cos(\theta-\Theta)}$, and $\alpha=\tan^{-1}\{[r\sin(\theta-\Theta)]/[R-r\cos(\theta-\Theta)]\}-\Theta$, where a cylindrical coordinate (r,θ,z) indicates the position of an point source in a scattering medium.

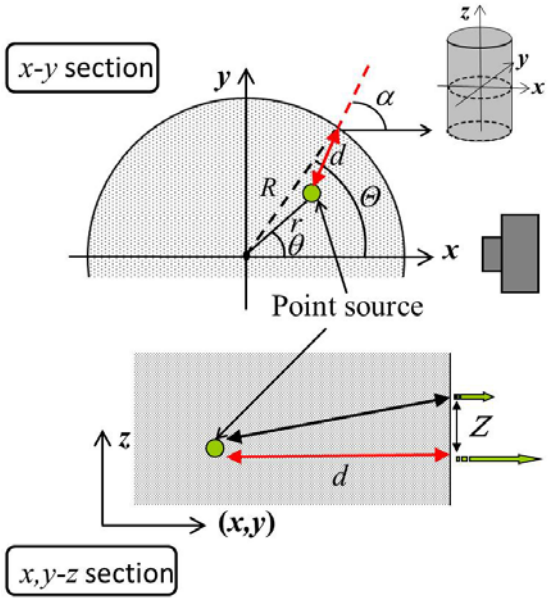

Fig. 8.21. Geometry of the theoretical model.

To suppress the scattering effect in transillumination of a scattering cylindrical medium, the deconvolution operation was performed using the above PSF. As a result, the transillumination image could be obtained similar to that through a low-scattering slab medium. This process will be repeated with the images observed in different circumferential directions, and obtain the projection images for the 3D reconstruction of the absorbing structure using the filtered back-projection method.

8.3.2 Validation in experiment

To validate the effectiveness of the proposed method, the experiment with an absorber rod in a tissue-equivalent phantom was conducted. Fig. 8.22(a) shows the

experimental system. An image was captured with a cooled CMOS camera, placed at the opposite side of the phantom to the light source. Intralipid suspension (Fresenius Kabi AG) and black ink (INK-30-B; Pilot Corp.) were mixed with distilled water to produce a tissue-equivalent medium (μ_s' =1.00 /mm, μ_a = 0.00536 /mm). It was contained in a cylindrical container (R=25.0 mm) made of polyacetal resin, which has the optical properties similar to those of human tissue. As an absorbing structure, a cylindrical post (5.00 mm diameter) made of black-painted metal was used. The distance between the center of the cylindrical scattering medium and the center of absorbing target was 19.5 mm. The transillumination images were recorded in different circumferential directions using a mechanical rotation system.

Figure 8.22(b) and 8.22(c) show the observed and deconvoluted images for the case θ=0°, or the absorber was on the x-axis. Figure 8.23 shows the intensity profiles along the horizontal centerlines of Fig. 8.22. The effect of scattering was effectively suppressed.

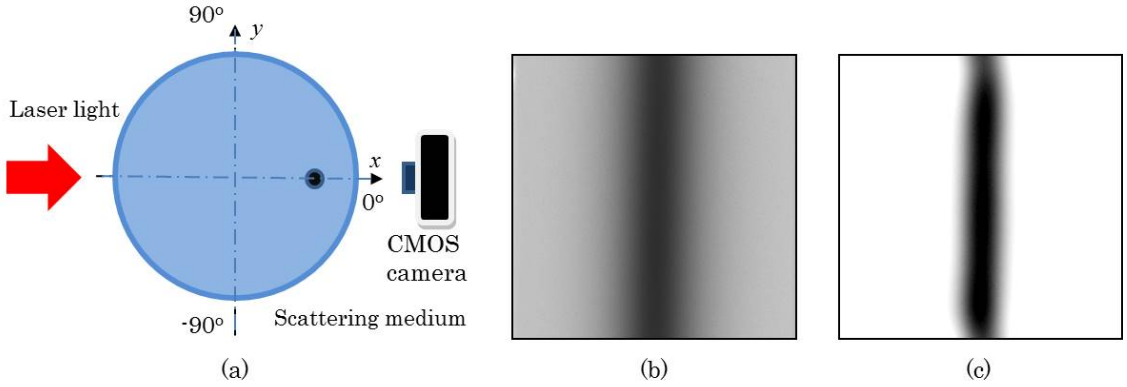

Fig. 8.22. Transillumination image at θ=0°: (a) experimental setup, (b) observed image, (c) deconvoluted image.

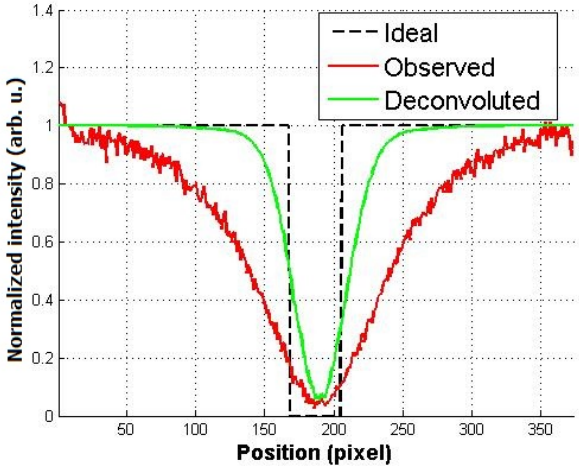

Fig. 8.23. Intensity profiles along horizontal centerlines of Fig. 8.22(b) and 8.22(c).

Figure 8.24 shows the result when the absorber was off-center from the observation light axis (x-axis) for the case θ=45°. Figure 8.25 shows the intensity profiles along the horizontal centerlines of observed image and deconvoluted image in Fig. 8.24. In this case, the thickness of the scattering medium in x-direction was asymmetry between left and right parts of the absorber. This causes the positional shift of the observed image toward the direction of thinner scattering medium. Thus, the transillumination images of the absorber were shifted toward the surface of the cylindrical scattering medium in Fig. 8.24. In the deconvolution with our PSF, the shift was corrected as well as deblurring the image.

Fig. 8.24. Result when the absorber was off-center from the observation light axis (x-axis) for the case θ=45°.

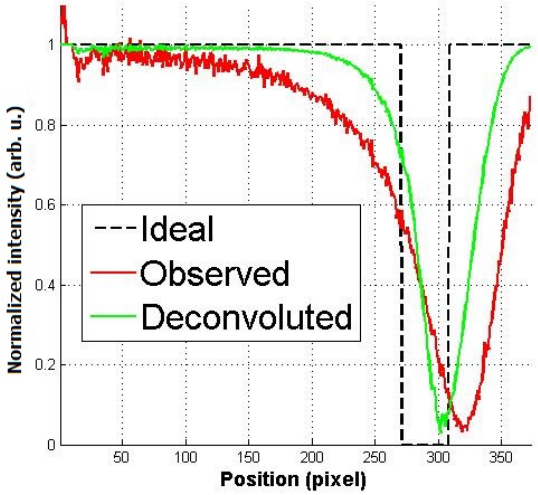

Fig. 8.25. Intensity profiles along horizontal centerlines of observed image and deconvoluted image in Fig. 8.24.

Figure 8.26 shows the result when the absorber was off-center from the observation light axis (x-axis) for the case θ=90°. In this case, the shifted effect became very strong

and it is difficult to recover the object. As shown in the Fig 8.26 the restored object became very thin. To overcome this problem, a new technique had devised to recover the object. Figure 8.27 illustrated the new technique. Figure 8.28 shows the result using the proposed technique when the absorber was off-center from the observation light axis (x-axis) for the case θ=90°. Figure 8.29 shows the intensity profiles along the centerlines of observed image and deconvoluted image. As shown in the Figs. 8.28 and 8.29, the object can be recovered properly.

Fig. 8.26. Result when the absorber was off-center from the observation light axis (x-axis) for the case θ=90°.

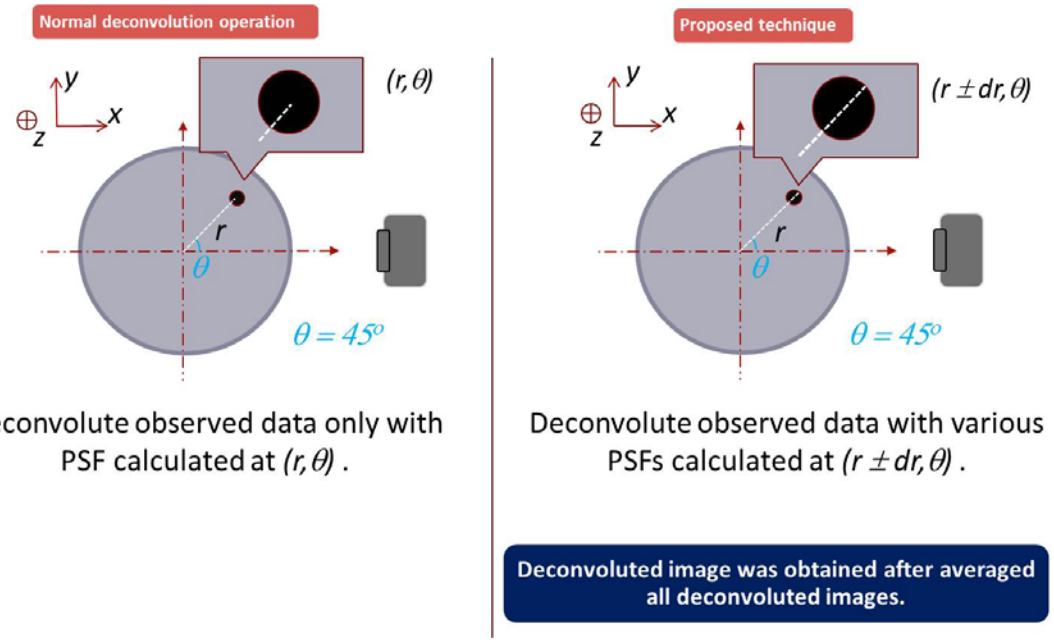

Fig. 8.27. Deconvolution operation technique while the absorber was off-center from the observation light axis.

Fig. 8.28. Result when the absorber was off-center from the observation light axis (x-axis) for the case θ =90°.

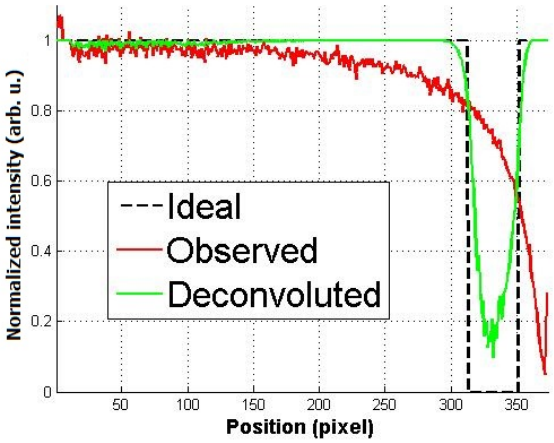

Fig. 8.29. Intensity profiles along horizontal centerlines of observed image and deconvoluted image in Fig. 8.28.

This process will be repeated with the images observed in different circumferential directions, and obtain the projection images for the 3D reconstruction of the absorbing structure using the filtered back-projection method. Figure 8.30 shows the cross-sectional images reconstructed from observed data and deconvoluted data. As shown in this figure, the shifted effect can be recovered in cross-sectional image from deconvoluted data.

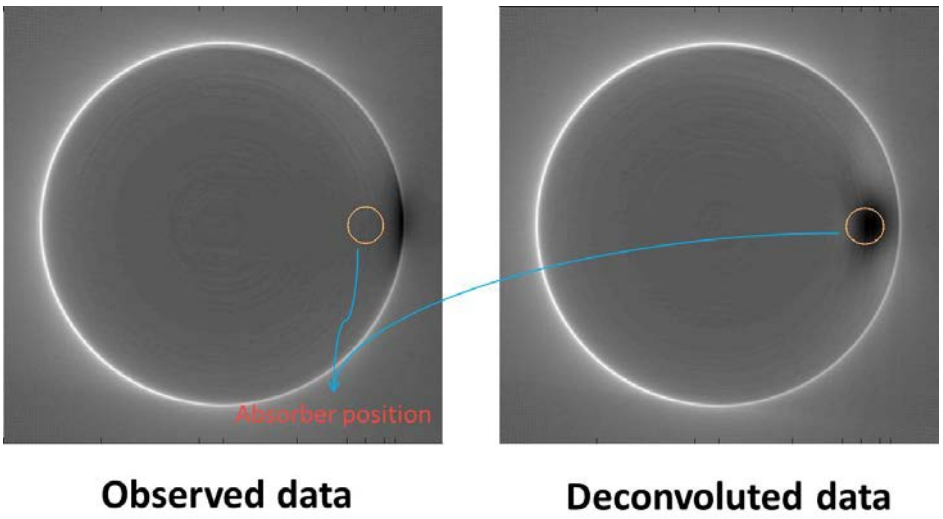

Fig. 8.30. Cross-sectional images reconstructed from observed images and deconvoluted images. Yellow circle indicates the true position of the absorber.

These cross-sectional images were piled up to reconstruct the 3D image of the absorbing structure. Figure 8.31 shows the 3D images of absorbing structure reconstructed from observed data and deconvoluted data. As shown in this figure, the 3D image reconstructed using the proposed method can be recovered properly.

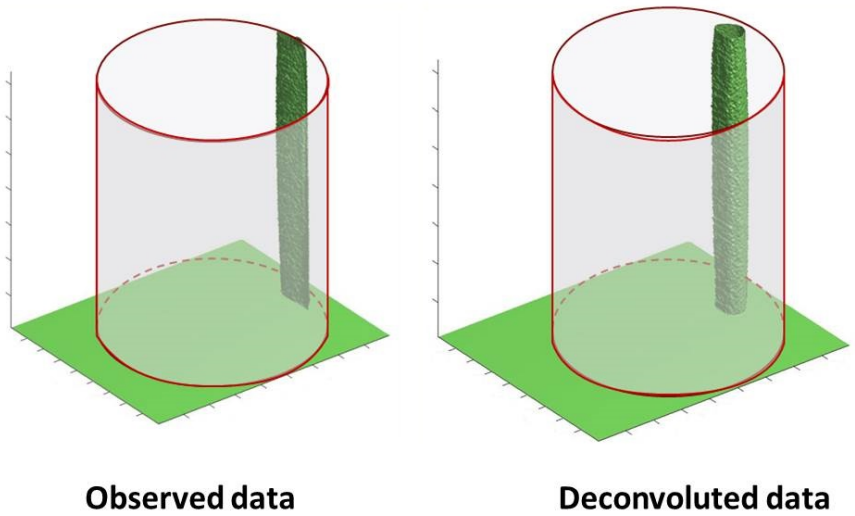

Fig. 8.31. 3D image of absorbing structure reconstructed from observed images and deconvoluted images.

Through this analysis, the effectiveness of the proposed technique was verified.

8.4 Conclusion

This chapter presented three additional studies that were performed to expand the proposed technique in this thesis for more practical application. The effectiveness of these techniques that proposed in these studies was confirmed in experiments. The result is promising and suggests the new techniques for applying in future studies using transillumination images.

Chapter 9
Conclusions

The objective of developing an optical tomography imaging system for small animals on a whole-body scale plays a significant character in current biological research. Optical imaging has several advantages over existing conventional imaging methods, such as the non-ionizing radiation, the inexpensive imaging equipment, the high sensitivity, and well fitted for the repetition and long-term studies events in live animals. However, the adoption of current optical techniques in preclinical imaging faces distinct challenges such as complex distribution of heterogeneous optical properties in animal's tissue, highly scattering effect of photons propagate through the tissue, complex boundaries, sophisticated source-detector pairs design, and highly ill-posed inverse problem associated with the tomographic reconstruction. The challenges guiding the development of a versatile imaging modality that can offer a wealth of data, which can be applied to research and produce novel approaches towards reducing the ill-posed inverse problem in small animal optical imaging.

The transillumination imaging using near-infrared (NIR) light of 700–1200 nm wavelength region constitute a promising powerful alternative imaging modality for noninvasive optical imaging of an animal body. With this technique, it is potential to reconstruct 3D image using the common filtered-back-projection. It reduces so much effort for computation in inverse problem. However, the major challenges face to the strong scattering in tissues and imaging strategies that provide rich data content.

In order to overcome these problems, three system design parameters were outlined. First, a continuous-wave imaging modality which provides the spatial information rich measurement data for whole-body small animal imaging will be used. Second, a CMOS or CCD based detection system which is relatively inexpensive system and ensures acquisition of measurements with high spatial resolution. And third, a novel scattering suppression technique will be developed for improving the observed transillumination images and providing more information for use in solving the inverse problem. The

novel contributions of this thesis are the development of a novel imaging technique that can be sensitively obtained the transillumination image of small animal body, a scattering suppression technique using point spread function (PSF) which was derived for the light source located in the scattering medium, and the new algorithm for reconstruct 3D image of unknown-structure in turbid medium. These developments establish the successful development of the 3D small animal imaging modality using transillumination image and details below.

1. Through theoretical and experimental study, the applicability and the effectiveness of the PSF for the light source to the transillumination images of the light-absorbing structure were confirmed and described in chapter 4.

2. The scattering effect was efficiently suppressed by deconvolving the transillmination image using the PSF above. It provided the useful projection image to 3D image reconstruction of absorbing structure using the common filtered back-projection algorithm. The effectiveness of the proposed technique was confirmed in 3D reconstruction for known-structure as described in chapter 5.

3. The PSF is depth-dependent, and the technique explained above was applicable only for an object with known internal structure. To expand the applicability of this technique, new algorithm had devised. An observed transillumination image is deconvoluted with the PSFs of different depths. Then the deconvoluted images are summed up to produce a new image that serves as a projection image in cross-sectional reconstruction. The projection image contains the projection of the true absorption distribution and the incompletely deconvoluted projection as well. To suppress the effect of this erroneous projection, an erasing process was devised. A cross-sectional image is reconstructed from the projection images obtained from many orientations. It is used as a template to erase the erroneous distribution in the cross-section. After the application of this erasing process, a new improved projection image is formed in which the effect of the erroneous distribution is suppressed effectively. The feasibility of the proposed technique was examined in a computer simulation and an experiment with a model phantom. The results demonstrated the effectiveness of the proposed technique as described in chapter 6.

4. Finally, the applicability of the proposed technique to a living animal was examined. An anesthetized mouse was fixed in a transparent cylinder. A practical technique using light trap in the cylinder was devised to produce a transillumination image of good quality. Using the proposed technique, the 3D structure of the mouse abdomen was reconstructed. High-absorbing organs such as the kidneys and parts of livers became visible as described in chapter 7.

Results of this study suggest that the realization of a novel non-contact optical CT, which is using NIR transillumination images with completely absence of matching fluids, having different features from those of currently available techniques such as conventional diffuse optical tomography (DOT) or time-resolved techniques. This simple system can provide a cross-sectional image and reconstruct the 3D structure of internal organ in the mouse body. It can provide a useful and safe tool for the functional imaging of internal organs of experimental animals and for optical CT imaging of the near-surface structure of the human body. The feasibility of 3D physiological function imaging using transillumination image was examined and described in section 8.2 with promising results.

This study opened a way toward practical 3D imaging of animal body. The applicability of the proposed technique could be expanded to use with other applications such as fluorescence and bioluminescence imaging and the biometric application.

Bibliography

Chapter 1

[1.1] J. M. Boone, O. Velazquez, and S. R. Cherry, "Small-animal X-ray dose from micro-CT," Mol. Imaging **3**, 149–158 (2004).

[1.2] V. Koo, P. W. Hamilton, and K. Williamson, "Non-invasive in vivo imaging in small animal research," Cell. Oncol. **28**, 127–139 (2006).

[1.3] S. H. Bartling, W. Stiller, W. Semmler, F. Kiessling, "Small Animal Computed Tomography Imaging," Curr. Med. Imaging Rev. **3**, 45–59 (2007).

[1.4] B. L. Franc, P. D. Acton, C. Mari, and B. H. Hasegawa, "Small-animal SPECT and SPECT/CT: important tools for preclinical investigation," J. Nucl. Med. **49**,1651–1663 (2008).

[1.5] H. Li, H. Zhang, Z. Tang, and G. Hu, "Micro-computed tomography for small animal imaging: technological details," Progress in Natural Science **18**, 513–521 (2008).

[1.6] F. B. DiFilippo, S. Patel, K. Asosingh, S. C. Erzurum, "Small-animal imaging using clinical positron emission tomography/computed tomography and super-resolution," Mol. Imaging. **11**, 210–219 (2012).

[1.7] M. L. James and S. S. Gambhir, "A molecular imaging primer: modalities, imaging agents, and applications," Physiol. Rev. **92**, 897–965 (2012).

[1.8] J. S. Lewis, S. Achilefu, J. R. Garbow, R. Laforest, and M. J. Welch, "Small animal imaging: current technology and perspectives for oncological imaging," Eur. J. Cancer **38**, 2173–2188 (2002).

[1.9] R. Weissleder, "Scaling down imaging: molecular mapping of cancer in mice," Nat. Rev. Cancer **2**, 11–18 (2002).

[1.10] M. Rudin and R. Weissleder, "Molecular imaging in drug discovery and development," Nat. Rev. Drug. Discov. **2**, 123–131 (2003).

[1.11] T. F. Massoud and S. S. Gambhir, "Molecular imaging in living subjects: seeing fundamental biological processes in a new light," Genes. Dev. **17**, 545–580 (2003).

[1.12] A. H. Hielscher, "Optical tomographic imaging of small animals," Curr. Opin.

Biotechnol. **16**, 79–88 (2005).

[1.13] G. Zacharakis, J. Ripoll, R. Weissleder, and V. Ntziachristos, "Fluorescent protein tomography scanner for small animal imaging," IEEE Trans. Med. Imaging **24**, 878–885 (2005).

[1.14] V. Ntziachristos, "Fluorescence molecular imaging," Annu. Rev. Biomed. Eng. **8**, 1–33 (2006).

[1.15] E. L. Kaijzel, G. van der Pluijm, and C. W, Löwik, "Whole-body optical imaging in animal models to assess cancer development and progression," Clin. Cancer Res. **13**, 3490–3497 (2007).

[1.16] J. K. Willmann, N. van Bruggen, L. M. Dinkelborg, and S. S. Gambhir, "Molecular imaging in drug development," Nat. Rev. Drug. Discov. **7**, 591–607 (2008).

[1.17] R. B. Schulz and W. Semmler , "Fundamental of optical imaging," in *Handbook of Experimental Pharmacology 185/I*, W. Semmler and M. Schwaiger eds. (Springer-Verlag, Berlin, Heidenberg, 2008).

[1.18] R. Weissleder and M. J. Pittet, "Imaging in the era of molecular oncology," Nature **452**, 580–589 (2008).

[1.19] F. Leblond, S. C. Davis, P. A. Valdés, and B. W. Pogue, "Pre-clinical whole-body fluorescence imaging: Review of instruments, methods and applications," J. of Photochem. and Photobio. B: Biology **98**, 77–94, (2010).

[1.20] S. Dufort, L. Sancey, C. Wenk, V. Josserand, and J. L. Coll, "Optical small animal imaging in the drug discovery process," Biochim. Biophysica. Acta. **1798**, 2266–2273 (2010).

[1.21] J. A. Guggenheim, H. R. A. Basevi, J. Frampton, I. B. Styles, and H. Dehghani, "Multi-modal molecular diffuse optical tomography system for small animal imaging," Meas. Sci. Technol. **24**, 105405–105426 (2013).

[1.22] C. Darne, Y. Lu, and E. M. Sevick-Muraca, "Small animal fluorescence and bioluminescence tomography: a review of approaches, algorithms and technology update," Phys Med Biol. **59**, R1–R64 (2014).

[1.23] R. Bright, *Diseases of the brain and nervous system vol. II* (London: Longman, 1831).

[1.24] T. B. Curling, *A practical treatise on the diseases of the testis and of the spermatic cord and scrotum* (London: Samuel Highley, 1843).

[1.25] M. Cutler, “Transillumination as an aid in the diagnosis of breast lesions,” Surg. Gynecol. Obstet. **48**, 721–728 (1929).

[1.26] J. C. Hebden, S. R. Arridge, and D. T. Delpy, “Optical imaging in medicine: I. Experimental techniques,” Phys. Med. Biol. **42**, 825–840 (1997).

[1.27] R. Weisslader and V. Ntziachristos, “Shedding light onto live molecular targets,” Nat. Med. **9**, 123–128 (2003).

[1.28] A. P. Gibson, J. C. Hebden, and S. R. Arridge, “Recent advances in diffuse optical imaging,” Phys. Med. Biol. **50**, R1–R43 (2005).

[1.29] A. Gibson and H. Dehghani, “Diffuse optical imaging,” Phil. Trans. R. Soc. A **367**, 3055–3072 (2009).

[1.30] B. D'Alessandro and A. P. Dhawan, “Transillumination imaging for blood oxygen saturation estimation of skin lesions,” IEEE Trans. Biomed. Eng. **59**, 2660–2667 (2012).

[1.31] F. F. Jöbsis, “Noninvasive infrared monitoring of cerebral and myocardial oxygen sufficiency and circulatory parameters,” Science **198**, 1264–1267 (1977).

[1.32] M. Cope and D. T. Delpy, “System for the long-term measurement of cerebral blood and tissue oxygenation on newborn infants by near infrared transillumination,” Med. Biol. Eng. Comput. **26**, 289–294 (1988).

[1.33] G. Gratton, P. M. Corballis, E. Cho, M. Fabiani, and D. C. Hood, “Shades of grey matter: noninvasive optical images of human brain responses during visual stimulation,” Psychophysiology **32**, 505–509 (1995).

[1.34] E. Okada, M. Firbank, M. Schweiger, S. R. Arridge, M. Cope, and D. T. Delpy, “Theoretical and experimental investigation of near-infrared light propagation in a model of the adult head,” Appl. Opt. **36**, 21–31 (1997).

[1.35] F. F. Jöbsis, “Discovery of the near-infrared window into the body and the early development of near infrared spectroscopy,” J. Biomed. Opt. **4**, 392–396 (1999).

[1.36] Y. Taka, Y. Kato, and K. Shimizu, “Transillumination imaging of physiological functions by NIR light,” in Proceedings of IEEE Conference on 22nd Annual International Conference of the IEEE Engineering in Medicine and Biology Society (IEEE, 2000), pp. 771–774.

[1.37] H. Obrig and A. Villringer, “Beyond the visible—imaging the human brain with light,” J. Cereb. Blood Flow Metab. **23**, 1–18 (2003).

[1.38] Y. Hoshi, “Functional near-infrared optical imaging: utility and limitations in

human brain mapping," Psychophysiology **40**, 511–520 (2003).

[1.39] I. Nishidate, Y. Aizu, and H. Mishina, "Depth visualization of a local blood region in skin tissue by use of diffuse reflectance images," Opt. Lett. **30**, 2128–2130 (2005).

[1.40] M. Wolf, M. Ferrari, and V. Quaresima, "Progress of near-infrared spectroscopy and topography for brain and muscle clinical applications," J. Biomed. Opt. **12**, 062104 (2007).

[1.41] T. Hamaoka, K. K. McCully, V. Quaresima, K. Yamamoto, and B. Chance, "Near-infrared spectroscopy/imaging for monitoring muscle oxygenation and oxidative metabolism in healthy and diseased humans," J. Biomed. Opt. **12**, 062105 (2007).

[1.42] A. Y. Bluestone, G. Abdoulaev, C. Schmitz, R. L. Barbour, and A. H. Hielscher, "Three-dimensional optical tomography of hemodynamics in the human head," Opt. Express **9**, 272–286 (2001).

[1.43] D. A. Boas, D. H. Brooks, E. L. Miller, C. A. DiMarzio, M. Kilmer, R. J. Gaudette, and Q. Zhang, "Imaging the body with diffuse optical tomography," IEEE Signal Processing Magazine **18**, 57–75 (2001).

[1.44] H. Jiang, Y. Xu, N. Iftimia, J. Eggert, K. Klove, L. Baron, and L. Fajardo, "Three-dimensional optical tomographic imaging of breast in a human subject," IEEE Trans. Med. Img. **20**, 1334–1340 (2001).

[1.45] A. H. Hielscher, A. Y. Bluestone, G. S. Abdoulaev, A. D. Klose, J. Lasker, M. Stewart, U. Netz, and J. Beuthan, "Near-infrared diffuse optical tomography," Dis. Markers. **18**, 313–337 (2002).

[1.46] F. Gao, H. Zhao, and Y. Yamada, "Improvement of image quality in diffuse optical tomography by use of full time-resolved data," Appl. Opt. **41**, 778–791 (2002).

[1.47] J. C. Hebden, A. Gibson, R. M. Yusof, N. Everdell, E. M. C. Hillman, D. T. Delpy, S. R. Arridge, T. Austin, J. H. Meek, and J. S. Wyatt, "Three-dimensional optical tomography of the premature infant brain," Phys. Med. Biol. **47**, 4155–4166 (2002).

[1.48] H. Dehghani, B. W. Pogue, S. P. Poplack, and K. D. Paulsen, "Multiwavelength three-dimensional near-infrared tomography of the breast: initial simulation, phantom, and clinical results," Appl. Opt. **42**, 135–145 (2003).

[1.49] J. P. Culver, A. M. Siegel, J. J. Stott, and D. A. Boas,"Volumetric diffuse optical

tomography of brain activity," Opt. Lett. **28**, 2061–2063 (2003).

[1.50] D. A. Boas, K. Chen, D. Grebert, and M. A. Franceschini,"Improving the diffuse optical imaging spatial resolution of the cerebral hemodynamic response to brain activation in humans," Opt. Lett. **29**, 1506–1508 (2004).

[1.51] B. W. Pogue, S. C. Davis, X. Song, B. A. Brooksby, H. Dehghani, and K. D. Paulsen, "Image analysis methods for diffuse optical tomography," J. Biomed. Opt. **11**, 033001 (2006).

[1.52] L. C. Enfield, A. P. Gibson, N. L. Everdell, D. T. Delpy, M. Schweiger, S. R. Arridge, C. Richardson, M. Keshtgar, M. Douek, and J. C. Hebden, "Three-dimensional time-resolved optical mammography of the uncompressed breast," Appl. Opt. **46**, 3628–3638 (2007).

[1.53] M. L. Flexman, F. Vlachos, H. K. Kim, S. R. Sirsi, J. Huang, S. L. Hernandez, T. B. Johung, J. W. Gander, A. R. Reichstein, B. S. Lampl, A. Wang, M. A. Borden, D. J. Yamashiro, J. J. Kandel, and A. H. Hielscher, "Monitoring early tumor response to drug therapy with diffuse optical tomography," J. Biomed. Opt. **17**, 016014 (2012).

[1.54] D. S. C. Biggs and M. Andrews, "Acceleration of iterative image restoration algorithms," Appl. Opt. **36**, 1766–1775 (1997).

[1.55] R. J. Hanisch, R. L. White, and R. L. Gilliland, "Deconvolution of hubble space telescope images and spectra," in *Deconvolution of images and spectra*, P.A. Jansson, ed. (Academic Press, Boston, MA, 1997).

[1.56] K. Shimizu, K. Tochio, and Y. Kato, "Improvement of transcutaneous fluorescent images with depth-dependent point-spread function," Appl. Opt. **44**, 2154–2161 (2005).

Chapter 2

[2.1] J. M. Boone, O. Velazquez, and S. R. Cherry, "Small-animal X-ray dose from micro-CT," Mol. Imaging **3**, 149-58 (2004).

[2.2] V. Koo, P. W. Hamilton, and K. Williamson, "Non-invasive in vivo imaging in small animal research," Cell. Oncol. **28**, 127–139 (2006).

[2.3] S. H. Bartling, W. Stiller, W. Semmler, F. Kiessling, "Small Animal Computed Tomography Imaging," Curr. Med. Imaging Rev. **3**, 45–59 (2007).

[2.4] B. L. Franc, P. D. Acton, C. Mari, and B. H. Hasegawa, "Small-animal SPECT and SPECT/CT: important tools for preclinical investigation," J. Nucl. Med. **49**,1651–1663 (2008).

[2.5] H. Li, H. Zhang, Z. Tang, and G. Hu, "Micro-computed tomography for small animal imaging: technological details," Progress in Natural Science **18**, 513–521 (2008).

[2.6] F. B. DiFilippo, S. Patel, K. Asosingh, S. C. Erzurum, "Small-animal imaging using clinical positron emission tomography/computed tomography and super-resolution," Mol. Imaging. **11**, 210–219 (2012).

[2.7] M. L. James and S. S. Gambhir, "A molecular imaging primer: modalities, imaging agents, and applications," Physiol. Rev. **92**, 897–965 (2012).

[2.8] J. S. Lewis, S. Achilefu, J. R. Garbow, R. Laforest, and M. J. Welch, "Small animal imaging: current technology and perspectives for oncological imaging," Eur. J. Cancer **38**, 2173–2188 (2002).

[2.9] R. Weissleder, "Scaling down imaging: molecular mapping of cancer in mice," Nat. Rev. Cancer **2**, 11–18 (2002).

[2.10] M. Rudin and R. Weissleder, "Molecular imaging in drug discovery and development," Nat. Rev. Drug. Discov. **2**, 123–131 (2003).

[2.11] T. F. Massoud and S. S. Gambhir, "Molecular imaging in living subjects: seeing fundamental biological processes in a new light," Genes. Dev. **17**, 545–580 (2003).

[2.12] A. H. Hielscher, "Optical tomographic imaging of small animals," Curr. Opin. Biotechnol. **16**, 79–88 (2005).

[2.13] G. Zacharakis, J. Ripoll, R. Weissleder, and V. Ntziachristos, "Fluorescent protein tomography scanner for small animal imaging," IEEE Trans. Med. Imaging **24**, 878–885 (2005).

[2.14] V. Ntziachristos, "Fluorescence molecular imaging," Annu. Rev. Biomed. Eng. **8**, 1–33 (2006).

[2.15] E. L. Kaijzel, G. van der Pluijm, and C. W, Löwik, "Whole-body optical imaging in animal models to assess cancer development and progression," Clin. Cancer Res. **13**, 3490–3497 (2007).

[2.16] J. K. Willmann, N. van Bruggen, L. M. Dinkelborg, and S. S. Gambhir, "Molecular imaging in drug development," Nat. Rev. Drug. Discov. **7**, 591–607

(2008).

[2.17] R. B. Schulz and W. Semmler , "Fundamental of optical imaging," in *Handbook of Experimental Pharmacology 185/I*, W. Semmler and M. Schwaiger eds. (Springer-Verlag, Berlin, Heidenberg, 2008).

[2.18] R. Weissleder and M. J. Pittet, "Imaging in the era of molecular oncology," Nature **452**, 580–589 (2008).

[2.19] F. Leblond, S. C. Davis, P. A. Valdés, and B. W. Pogue, "Pre-clinical whole-body fluorescence imaging: Review of instruments, methods and applications," J. of Photochem. and Photobio. B: Biology **98**, 77–94, (2010).

[2.20] S. Dufort, L. Sancey, C. Wenk, V. Josserand, and J. L. Coll, "Optical small animal imaging in the drug discovery process," Biochim. Biophysica. Acta. **1798**, 2266–2273 (2010).

[2.21] J. A. Guggenheim, H. R. A. Basevi, J. Frampton, I. B. Styles, and H. Dehghani, "Multi-modal molecular diffuse optical tomography system for small animal imaging," Meas. Sci. Technol. **24**, 105405–105426 (2013).

[2.22] C. Darne, Y. Lu, and E. M. Sevick-Muraca, "Small animal fluorescence and bioluminescence tomography: a review of approaches, algorithms and technology update," Phys Med Biol. **59**, R1–R64 (2014).

[2.23] A. Y. Bluestone, G. Abdoulaev, C. Schmitz, R. L. Barbour, and A. H. Hielscher, "Three-dimensional optical tomography of hemodynamics in the human head," Opt. Express **9**, 272–286 (2001).

[2.24] D. A. Boas, D. H. Brooks, E. L. Miller, C. A. DiMarzio, M. Kilmer, R. J. Gaudette, and Q. Zhang, "Imaging the body with diffuse optical tomography," IEEE Signal Processing Magazine **18**, 57–75 (2001).

[2.25] H. Jiang, Y. Xu, N. Iftimia, J. Eggert, K. Klove, L. Baron, and L. Fajardo, "Three-dimensional optical tomographic imaging of breast in a human subject," IEEE Trans. Med. Img. **20**, 1334–1340 (2001).

[2.26] A. H. Hielscher, A. Y. Bluestone, G. S. Abdoulaev, A. D. Klose, J. Lasker, M. Stewart, U. Netz, and J. Beuthan, "Near-infrared diffuse optical tomography," Dis. Markers. **18**, 313–337 (2002).

[2.27] F. Gao, H. Zhao, and Y. Yamada, "Improvement of image quality in diffuse optical tomography by use of full time-resolved data," Appl. Opt. **41**, 778–791 (2002).

[2.28] J. C. Hebden, A. Gibson, R. M. Yusof, N. Everdell, E. M. C. Hillman, D. T. Delpy,

S. R. Arridge, T. Austin, J. H. Meek, and J. S. Wyatt, "Three-dimensional optical tomography of the premature infant brain," Phys. Med. Biol. **47**, 4155–4166 (2002).

[2.29] H. Dehghani, B. W. Pogue, S. P. Poplack, and K. D. Paulsen, "Multiwavelength three-dimensional near-infrared tomography of the breast: initial simulation, phantom, and clinical results," Appl. Opt. **42**, 135–145 (2003).

[2.30] J. P. Culver, A. M. Siegel, J. J. Stott, and D. A. Boas,"Volumetric diffuse optical tomography of brain activity," Opt. Lett. **28**, 2061–2063 (2003).

[2.31] D. A. Boas, K. Chen, D. Grebert, and M. A. Franceschini,"Improving the diffuse optical imaging spatial resolution of the cerebral hemodynamic response to brain activation in humans," Opt. Lett. **29**, 1506–1508 (2004).

[2.32] B. W. Pogue, S. C. Davis, X. Song, B. A. Brooksby, H. Dehghani, and K. D. Paulsen, "Image analysis methods for diffuse optical tomography," J. Biomed. Opt. **11**, 033001 (2006).

[2.33] L. C. Enfield, A. P. Gibson, N. L. Everdell, D. T. Delpy, M. Schweiger, S. R. Arridge, C. Richardson, M. Keshtgar, M. Douek, and J. C. Hebden, "Three-dimensional time-resolved optical mammography of the uncompressed breast," Appl. Opt. **46**, 3628–3638 (2007).

[2.34] M. L. Flexman, F. Vlachos, H. K. Kim, S. R. Sirsi, J. Huang, S. L. Hernandez, T. B. Johung, J. W. Gander, A. R. Reichstein, B. S. Lampl, A. Wang, M. A. Borden, D. J. Yamashiro, J. J. Kandel, A. H. Hielscher, "Monitoring early tumor response to drug therapy with diffuse optical tomography," J. Biomed. Opt. **17**, 016014 (2012).

[2.35] L. G. Henyey and J. L. Greenstein, "Diffuse radiation in the galaxy," Astrophys. J. **93**, 70–83 (1941).

[2.36] D. T. Delpy, M. Cope, P. van der Zee, S. Arridge, S. Wray, and J. Wyatt, "Estimation of optical pathlength through tissue from direct time of flight measurement," Phys. Med. Biol. **33**, 1433–1442 (1988).

[2.37] W. F. Cheong, S. A. Prahl, and A. J. Welch, "A review of the optical properties of biological tissues," IEEE Journal of Quantum Electronics **26**, 2166–2185 (1990).

[2.38] J. Mourant, T. Fuselier, J. Boyer, T. Johnson, and I. Bigio, "Predictions and measurements of scattering and absorption over broad wavelength ranges in

tissue phantoms," Appl. Opt. **36**, 949–957 (1997).

[2.39] S. L. Jacques and S. A. Prahl, *ECE532 Biomedical Optics*, Oregon Graduate Institute (1998). (http://omlc.ogi.edu/education/ece532/class3/muaspectra.html)

[2.40] V. Tuchin, *Tissue optics: Light Scattering Methods and Instruments for Medical Diagnosis*, (SPIE Optical Engineering Press, Bellingham, WA, 2000).

[2.41] A. Torricelli, A. Pifferi, P. Taroni, E. Giambattistelli, and R. Cubeddu, "In vivo optical characterization of human tissues from 610 to 1010 nm by time-resolved reflectance spectroscopy," Phys. Med. Biol. **46**, 2227–2237 (2001).

[2.42] J. Mobley and T. Vo-Dinh, "Optical properties of tissue," in *Biomedical Photonics Handbook* T. Vo-Dinh, ed. (CRC Press, Boca Raton, FL, 2003).

[2.43] G. Alexandrakis, F. Rannou, and A. Chatziioannou, "Tomographic bioluminescence imaging by use of a combined optical-PET (OPET) system: a computer simulation feasibility study," Physics in Medicine and Biology **50**, 4225–4241 (2005).

[2.44] D. T. Delpy and M. Cope, "Quantification in tissue near infrared spectroscopy," Phil. Trans. R. Soc. Lond. B **352**, 649-659 (1997).

[2.45] D. Hattery, V. Chernomordik, M. Loew, I. Gannot, and A. Gandjbakhche, "Analytical solutions for time-resolved fluorescence lifetime imaging in a turbid medium such as tissue," J. Opt. Soc. Am. A **18**, 1523-1530 (2001).

[2.46] V. Ntziachristos and R. Weissleder, "Charge-coupled-device based scanner for tomography of fluorescent near-infrared probes in turbid media," Med. Phys. **29**, 803–809 (2002).

[2.47] H. Koizumi, T. Yamamoto, A. Maki, Y. Yamashita, H. Sato, H. Kawaguchi, and N. Ichikawa, "Optical topography: practical problems and new applications," Appl. Opt. **42**, 3054–3062 (2003).

[2.48] G. Zacharakis, J. Ripoll, R. Weissleder, and V. Ntziachristos, "Fluorescent protein tomography scanner for small animal imaging," IEEE Trans. Medical Imaging **24**, 878–885 (2005).

[2.49] N. Deliolanis, T. Lasser, D. Hyde, A. Soubret, J. Ripoll, and V. Ntziachristos, "Free-space fluorescence molecular tomography utilizing 360 degrees geometry projections," Opt. Lett. **32**, 382–384 (2007).

[2.50] D. Kepshire, S. Davis, H. Dehghani, K. Paulsen, and B. Pogue, "Fluorescence tomography characterization for sub-surface imaging with protoporphyrin IX," Opt. Express **16**, 8581–8593 (2008).

[2.51] H. Korideck and J. Peterson, "Noninvasive, in vivo quantification of asthma severity using fluorescence molecular tomography," Nature Methods **5**, iii–iv (2008).

[2.52] S. Han, S. Farshchi-Heydari, and D. Hall, "Analytical method for the fast time-domain reconstruction of fluorescent inclusions in vitro and in vivo," Biophys. J. **98**, 350–357 (2010).

[2.53] B. Chance, M. Cope, E. Gratton, N. Ramanujam, and B. Tromberg,, "Phase measurement of light absorption and scatter in human tissue," Rev. Sci. Instrum. **69**, 3457–3481 (1998).

[2.54] S. Arridge and B. Lionheart, "Non-uniqueness in diffusion-based optical tomography," Opt. Lett. **23**, 882–884 (1998).

[2.55] F. Bevilacqua, A. Berger, A. Cerussi, D. Jakubowski, and B. Tromberg, "Broadband absorption spectroscopy in turbid media by combined frequency-domain and steady-state methods," Appl. Opt. **39**, 6498–6507 (2000).

[2.56] A. H. Hielscher, A. Y. Bluestone, G. S. Abdoulaev, A. D. Klose, J. Lasker, M. Stewart, U. Netz, and J. Beuthan, "Near-infrared diffuse optical tomography," Dis. Markers. **18**, 313–337 (2002).

[2.57] E. M. Sevick-Muraca, J. P. Houston, and M. Gurnkel, "Fluorescence-enhanced, near infrared diagnostic imaging with contrast agents," Curr. Opin. Chem. Biol. **6**, 642–650 (2002).

[2.58] A. Liebert, H. Wabnitz, D. Grosenick, and R. Macdonald, "Fiber dispersion in time domain measurements compromising the accuracy of determination of optical properties of strongly scattering media," J. Biomed. Opt. **8**, 512–516 (2003).

[2.59] E. Graves, J. Ripoll, R. Weissleder, and V. Ntziachristos, "A submillimeter resolution fluorescence molecular imaging system for small animal imaging," Med. Phys. **30**, 901–911 (2003).

[2.60] R. Roy, A. Godavarty, and E. M. Sevick-Muraca, "Fluorescence-enhanced optical tomography using referenced measurements of heterogeneous media," IEEE

Trans Med Imaging **22**, 824–836 (2003).

[2.61] A. Godavarty, E. M. Sevick-Muraca, and M. Eppstein, “Three-dimensional fluorescence lifetime tomography," Med. Phys. **32**, 992–1000 (2005).

[2.62] A. P. Gibson, J. C. Hebden, S. R. Arridge, “Recent advances in diffuse optical imaging,” Phys. Med. Biol. **50**, R1–R43 (2005).

[2.63] A. T. N. Kumar, J. Skoch, B. J. Bacskai, D. A. Boas, A. K. Dunn, “Fluorescence lifetime based tomography for turbid media,” Opt. Lett. **30**, 3347–3349 (2005).

[2.64] S. Bloch, F. Lesage, L. McIntosh, A. Gandjbakhche, K. Liang, and S. Achilefu, “Whole-body fluorescence lifetime imaging of a tumor-targeted near-infrared molecular probe in mice,” J. Biomed. Opt. **10**, 054003 (2005).

[2.65] V. Ntziachristos, J. Ripoll, L. V. Wang, and R. Weissleder, “Looking and listening to light: the evolution of whole-body photonic imaging,” Nat. Biotechnol. **23**, 313–320 (2005).

[2.66] X. Intes and B. Chance, “Multi-frequency diffuse optical tomography,” J. Mod. Opt. **52**, 2139–2159 (2005).

[2.67] M. B. Unlu, O. Birgul, R. Shafiiha, G. Gulsen, O. Nalcioglu, “Diffuse optical tomographic reconstruction using multifrequency data,” J. Biomed. Opt. **11**, 054008 (2006).

[2.68] R. Roy, A. Godavarty, and E. M. Sevick-Muraca, “Fluorescence-enhanced optical tomography of a large tissue phantom using point illumination geometries,” J. Biomed. Opt. **11**, 044007 (2006).

[2.69] V. Ntziachristos, “Fluorescence molecular imaging,” Annu. Rev. Biomed. Eng. **8**, 1–33 (2006).

[2.70] A. Joshi, J. C. Rasmussen, E. M. Sevick-Muraca, T. A. Wareing, and J. McGhee, “Radiative transport-based frequency-domain fluorescence tomography,” Phys. Med. Biol. **53**, 2069–2088 (2008).

[2.71] A. T. N. Kumar, S. B. Raymond, A. K. Dunn, B. J. Bacskai, and D. A. Boas, “A time domain fluorescence tomography system for small animal imaging,” IEEE Trans. Med. Imaging **27**, 1152–1163 (2008).

[2.72] L. Zhang, F. Gao, H. He, and H. Zhao, “Three-dimensional scheme for time-domain fluorescence molecular tomography based on laplace transforms with noise-robust factors," Opt. Express **16**, 7214–7223 (2008).

[2.73] S. Davis, B. Pogue, R. Springett, C. Leussler, P. Mazurkewitz, S. Tuttle, S.

Gibbs-Strauss, S. Jiang, H. Dehghani, and P. K.D., "Magnetic resonance coupled fluorescence tomography scanner for molecular imaging of tissue," Rev. Sci. Instrum. **79**, 064302 (2008).

[2.74] S. Patwardhan and J. Culver, "Quantitative diffuse optical tomography for small animals using an ultrafast gated image intensifier," J. Biomed. Opt. **13**, 011009 (2008).

[2.75] U. Netz, J. Beuthan, and A. Hielscher, "Multipixel system for gigahertz frequency-domain optical imaging of finger joints," Rev. Sci. Instrum. **79**, 034301 (2008).

[2.76] M. Bartels, W. Chen, R. Bardhan, S. Ke, N. J. Halas, T. Wareing, J. McGhee, and A. Joshi, "Multimodal optical molecular image reconstruction with frequency domain measurements," Conf. Proc. IEEE Eng. Med. Biol. Soc. 2009, 6655–6658 (2009).

[2.77] R. E. Nothdurft, S. V. Patwardhan, W. Akers, Y. Ye, S. Achilefu, and J. P. Culver, "In vivo fluorescence lifetime tomography," J. Biomed. Opt. **14**, 024004 (2009).

[2.78] V. Soloviev, C. D'Andrea, G. Valentini, R. Cubeddu, and S. Arridge, "Combined reconstruction of fluorescent and optical parameters using time-resolved data," Appl. Opt. **48**, 28–36 (2009).

[2.79] T. Poschinger, *Non-contact optical fluorescence tomography for small animal imaging*, Ph. D. thesis, Friedrich-Alexander-Universitat Erlangen-Nurnberg, 2010.

[2.80] C. Darne, B. Zhu, Y. Lu, I. Tan, J. Rasmussen, and E. M. Sevick-Muraca, "Radiofrequency circuit design and performance evaluation for small animal frequency-domain NIR fluorescence optical tomography," in Proceedings of SPIE **7896**, 789621 (2011).

[2.81] V. Venugopal, *A small animal time-resolved optical tomography platform using wide-field excitation*, Ph. D. thesis, Rensselaer Polytechnic Institute, 2011.

[2.82] Y. Lin, D. Thayer, O. Nalcioglu, and G. Gulsen, "Tumor characterization in small animals using magnetic resonance-guided dynamic contrast enhanced diffuse optical tomography ," J. Biomed. Opt **16**, 106015 (2011).

[2.83] J. Chen, *Optical tomography in small animal with time-resolved monte carlo methods*, Ph. D. thesis, Rensselaer Polytechnic Institute, 2012.

[2.84] K. Shimizu, K. Tochio, and Y. Kato, "Improvement of transcutaneous fluorescent

images with a depth-dependent point-spread function," Appl. Opt. **44**, 2154–2161 (2005).

Chapter 3

[3.1] R. H. Bracewell and A. C. Riddle, "Inversion of fan beam scans in radio astronomy," Astrophysics J. **150**, 427– 434 (1967).

[3.2] G. N. Ramanchandran and A. V. Lakshminarayanan, "Three dimensional reconstructions from radiographs and electron micrographs: application of convolution instead of Fourier transforms," Proc. Nat. Acad. Sci. **68**, 2236–2240 (1971).

[3.3] A. V. Lakshminarayanan, *Reconstruction from divergent ray data*, Tech. rep., Dept. Computer Science, State University of New York at Buffalo, 1975.

[3.4] H. H. Barrett and W. Swindell, *Radialogical imaging: the theory of image formation, detection and processing*, (Academic Press, New York, NY, 1981).

[3.5] A. C. Kak and M. Slaney, *Principles of computerized tomographic imaging*, (IEEE Press, New York, NY, 1988).

[3.6] R. P. V. Rao, R. D. Kriz, A. L. Abbott, and C. J. Ribbens, "Parallel Implementation of the Filtered Back Projection Algorithm for Tomographic Imaging," Virginia Polytechnic Institute and State University, 1995. (http://www.sv.vt.edu/xray_ct/parallel/Parallel_CT.html)

[3.7] S. W. Smith, *The scientist and engineer's guide to digital signal processing 2nd edition*, (California Technical Publishing, San Diego, CA, 1997). (http://www.dspguide.com/)

[3.8] S. Coric, *Parallel-beam backprojection: an FPGA implementation optimized for medical imaging*, M. S. thesis, Northeastern University, 2002.

[3.9] J. L. Semmlow, *Biological and medical image processing*, (CRC Press, Boca Raton, FL, 2009).

[3.10] G. Van Gompel, *Towards accurate image reconstruction from truncated X-ray CT projections*, Ph. D. thesis, University of Antwerp, 2009.

[3.11] R. C. Gonzalez and R. E. Woods, *Digital image processing 3rd edition*, (Pearson Education, New Delhi, India, 2013).

[3.12] S. Chandrasekhar, *Radiative transfer*, (Oxford University Press, New York, NY,

1960).

[3.13] A. Ishimaru, "Theory and application of wave propagation and scattering in random media," Proceedings of the IEEE **65**, 1030–1061 (1977).

[3.14] A. Ishimaru, *Wave Propagation and scattering in random media vol. 1*, (Academic Press, New York, NY, 1978).

[3.15] A. Ishimaru, Y. Kuga, R. Cheung, and K. Shimizu, "Scattering and diffusion of a beam wave in randomly distributed scatterers," J. Opt. Soc. Am. **73**, 131–136 (1983).

[3.16] Y. Kuga, A. Ishimaru, H. Chang, and L. Tsang, "Comparisons between the small-angle approximation and the numerical solution for radiative transfer theory," Appl. Opt. **25**, 3803–3805 (1986).

[3.17] A. Ishimaru, "Wave propagation and scattering in random media and rough surfaces," Proceedings of the IEEE **79**, 1359–1366 (1991).

[3.18] A. Ishimaru, *Wave Propagation and Scattering in Random Media*, (IEEE Press, New York, 1997).

[3.19] V. Tuchin, *Tissue Optics*, (SPIE, Bellingham, Washington, DC 2000).

[3.20] M. I. Mischenko, "Vector radiative transfer equation for arbitrarily shaped and arbitrarily oriented particles: a microphysical derivation from statistical electromagnetics," Appl. Opt. **41**, 7114–7134 (2002).

[3.21] M. I. Mischenko, "Micro physical approach to polarized radiative transfer: extension to the case of an external observation point," Appl. Opt. **42**, 4963–4967 (2003).

[3.22] K. Shimizu, K. Tochio, and Y. Kato, "Improvement of transcutaneous fluorescent images with a depth-dependent point-spread function," Appl. Opt. **44**, 2154–2161 (2005).

[3.23] G. Branco, *The development and evaluation of head probes for optical imaging of the human head*, PhD thesis, University of London, 2007.

[3.24] F. Martelli, S. Del Bianco, A. Ismaelli, and G. Zaccanti, *Light propagation through biological tissue*, (SPIE Press, Bellingham, DC 2010).

[3.25] W. H. Richardson, "Bayesian-based iterative method of image restoration," J. Opt. Soc. A **62**, 55–59 (1972).

[3.26] L. B. Lucy, "An iterative technique for the rectification of observed distributions," The Astro. J. **79**, 745–754 (1974).

[3.27] D. S. C. Biggs and M. Andrews, "Acceleration of iterative image restoration algorithms," Appl. Opt. **36**, 1766–1775 (1997).

[3.28] R. J. Hanisch, R. L. White, and R. L. Gilliland, "Deconvolution of hubble space telescope images and spectra," in *Deconvolution of images and spectra*, P. A. Jansson, ed. (Academic Press, Boston, MA, 1997).

[3.29] H. Tian, *Noise analysis in cmos image sensors*, PhD thesis, Stanford University, 2000.

[3.30] N. Dey, L. Blanc-Feraud, C. Zimmer, Z. Kam, J. C. Olivio-Marin, and J. Zerubia, "A deconvolution method for confocal microscopy with total variation regularization," IEEE Inter. Symp. Biomed. Imaging: Nano to Macro **2**, 1223–1226 (2004).

[3.31] N. Dey, L. Blanc-Feraud, C. Zimmer, P. Roux, Z. Kam, J. C. Olivio-Marin, and J. Zerubia, *3d microscopy deconvolution using richardson-lucy algorithm with total variation regularization*, Tech. rep., INRIA, 2004.

[3.32] R. C. Gonzalez, R. E. Woods, and S. L. Eddins, *Digital image processing using matlab*, (Pearson Education, Upper Saddle River, NJ, 2004).

[3.33] N. Dey, L Blanc-Feraud, C. Zimmer, P. Roux, Z. Kam, J. C. Olivo-Marin, and Zerubia, "Richardson-Lucy algorithm with total variation regularization for 3D confocal microscope deconvolution," Microsc. Res. Tech. **69**, 260–266 (2006).

[3.34] M. Laasmaa, *The analysis of richardson-lucy deconvolution algorithm with application to microscope images*, MS thesis, Tallinn University of Technology, 2009.

[3.35] M. Temerinac-Ott, *Tile-based lucy-richardson deconvolution modelling a spatially-varying psf for fast multiview fusion of microscopical images*, Tech. Rep. 260, University of Freiburg, 2010.

[3.36] Y. Oyamada, *Pre/post blur correction from a single photo shooting*, Ph. D. thesis, Keio Univeristy, 2011.

Chapter 4

[4.1] K. Shimizu, K. Tochio, and Y. Kato, "Improvement of transcutaneous fluorescent images with a depth-dependent point-spread function," Appl. Opt. **44**, 2154–2161 (2005).

[4.2] T. N. Tran, T. Namita, Y. Kato, and K. Shimizu, "Application of fluorescent PSF for 3D reconstruction of absorbing structure using slab transillumination images," Engineering in Medicine and Biology Society, 2013, Proceedings of the 35th Ann. Int. Conf. of the IEEE, 2644–2647, (2013).

Chapter 5

[5.1] D. J. Kroon, "Showvol isosurface render," Matlab central file exchange ID 25987, (2011).
(http://www.mathworks.com/matlabcentral/fileexchange/25987-showvol-isosurface-render)

[5.2] T. N. Tran, T. Namita, Y. Kato, and K. Shimizu, "Application of fluorescent PSF for 3D reconstruction of absorbing structure using slab transillumination images," Engineering in Medicine and Biology Society, 2013, Proceedings of the 35th Ann. Int. Conf. of the IEEE, 2644–2647, (2013).

Chapter 6

[6.1] T. N. Tran, K. Yamamoto, T. Namita, Y. Kato, and K. Shimizu, "3D reconstruction of internal structure of animal body using near-infrared light," Proc. SPIE 8952, Biomed. App. of Light Scat. VIII, 89521A, (2014).

Chapter 7

[7.1] Science Council of Japan, Guidelines for proper conduct of animal experiments, (2006).

[7.2] T. N. Tran, K. Yamamoto, T. Namita, Y. Kato, and K. Shimizu, "3D reconstruction of internal structure of animal body using near-infrared light," Proc. SPIE 8952, Biomed. App. of Light Scat. VIII, 89521A, (2014).

Chapter 8

[8.1] K. Shimizu., K. Tochio, and Kato Y., "Improvement of transcutaneous fluorescent

images with depth-dependtdent point-spread function," Appl. Opt. **44**, 2154–2161 (2005).

[8.2] S. Wray, M. Cope, D. T. Delpy, J. S. Wyatt, E. O. R. Reynolds, "Characterization of the near infrared absorption spectra of cytochrome aa3 and haemoglobin for the non-invasive monitoring of cerebral oxygenation," Biochim. Biophys. Acta. **933**, 184–192 (1988).

[8.3] Y. Taka, Y. Kato, and K. Shimizu, "Transillumination imaging of physiological functions by NIR light," Engineering in Medicine and Biology Society, 2000, Proceedings of the 22nd Ann. Int. Conf. of the IEEE, 771–774 (2000).

[8.4] Science Council of Japan, Guidelines for proper conduct of animal experiments, (2006).

[8.5] E. Tozawa, T. Namita, Y. Kato and K. Shimizu, "Fundamental study for 3D reconstruction object in biological body," Technical Report of IEICE **111**(482), 123–128, (2012).

[8.6] D. Ogawa, T. Namita, Y. Kato and K. Shimizu, "Development of imaging technique for fluorescent object in cylindrical turbid medium – For transcutaneous fluorescent imaging through animal tissue –," Technical Report of IEICE **113**(499), 121–126, (2013).

Acknowledgement

First and foremost, I would like to express my deep gratitude to my research supervisor, Professor Koichi Shimizu. He continually conveyed to me his spirit of unsurpassed and his enthusiasm in academic that reinforced my conviction and ambitious to pursue my research. I am grateful for his willingness to give his time and being patient with my ignorance. His persistent support and thoughtful guidance played an inconvertible role in the completion of the present study. From Professor Koichi Shimizu, I have learned not only the Do's and Don'ts in the research practices, but also how to grow on my entire career path.

I would also like to extend my gratitude to my co-advisors. Associate Professor Nobuki Kudo, thank you very much for your understanding, your warmth encouragement and your trust in me tremendously helped me tackle difficulties and frustration to finish my research. Professor Hiroshi Hirata, thank you very much for your insightful comments and suggestions.

Next I give my sincere gratitude to Assistant Professor Yuji Kato. Thank you very much for all the discussions over the past three years. It has always given me a new perspective on my research. Without your suggestions, I would not be able to finish the goal of this study.

I am especially grateful to thank Dr. Takeshi Namita (currently with the Graduate School of Medicine, Kyoto University), who always lending me a helping hand. I am extremely grateful for his extensive discussion and constructive comments on my research, as well as his kind and compassionate care and support over the past three years. I owe him a debt of gratitude for the time spent working with him over the past three years. Especially, without him I would not be able to obtain the result that presented in this thesis. You made my life so much simpler.

Without their guidance and help this thesis would not have been possible.

I would especially like to thank Hokkaido University. With the scholarship from the university, I never had to worry about financial aid and was able to devote my full attention to my study. I would also like to thank everyone at the IST office, who have always given me good guidances that allowed me to do this course in good conditions..

To my colleagues in the laboratory, it was my pleasure and my honor to make friend with all awesome people like you. All dear friends, thank you very much for your help during my stay in the laboratory. Especially, I would like to thank Hiroki Takahashi, Yuki Okuyama, Kohei Yamamoto and Hiroyuki Tanaka for your kindness and your contributions to my work. I am grateful for the time spent working Simon Eyer, Ana Priscila Alves, Ana Jevtic, and Pola Artur during their internship in my laboratory. I wish you good luck in your future.

A big thank to my friends Pham Viet Dung and Katherine Fuji, who always think about me during the winters in Sapporo.

I would like to thank my parents Dang Luong Mo and Tran Thi Anh Xuan, who gave me warmth and unending moral support to pursue my study. Thank you very much for always being beside me and for encouraging me to grow up in my academic career. I would also like to thank my girlfriend Bui Phuong Anh for her love, support, and continued patience over the past year. Without their help it would have been impossible for me to achieve the success in my research.

My doctoral journey with the sleepless nights, the very long winters in Sapporo, and best friends was formed a memorable time that I never forget for the rest of my life. Finally a big thanks to all those I have not mentioned the name here and a great prayer for forgiveness from them.

To them I dedicate this thesis.

Jun. 2014,
Tran Trung Nghia

研　究　業　績　目　録

氏　名　Tran　Trung　Nghia

1. 論文（学位論文関係）

I 査読付学会誌等

(1) Trung Nghia Tran, Kohei Yamamoto, Takeshi Namita, Yuji Kato, and Koichi Shimizu: “Three-dimensional transillumination image reconstruction for small animal with new scattering suppression technique,” Biomed. Opt. Express. 掲載決定 (IF= 3.176).

II 査読付国際会議プロシーディング

(1) Trung Nghia TRAN, Takeshi Namita, Yuji Kato, and Koichi Shimizu: “3D reconstruction of internal structure of animal body using NIR light - Preliminary results for feasibility study -,” J. Sci. Tech., Vol. 50, No. 5A (Special Issue on 1st Int. Sympo. on Eng. Phys. and Mech.), Ho Chi Minh City, Vietnam, Oct. 25-26, pp. 76-79 (2011).

(2) Trung Nghia Tran, Takeshi Namita, Yuji Kato, and Koichi Shimizu: “Feasibility study for 3D reconstruction of internal structure of animal body using NIR light,” Proc. 4th Int. Conf. on Develop. of Biomed. Eng., Ho Chi Minh City, Vietnam, Jan. 8-12, pp. 162-164 (2012).

(3) Tran Trung Nghia, Takeshi Namita, Yuji Kato, and Koichi Shimizu: “Application of fluorescent PSF for 3D reconstruction of absorbing structure using slab transillumination images,” Eng. in Med. and Biol. Soc. (EMBC), 2013 Annual Int. Conf. of IEEE, Osaka, Japan, Jul. 3-7, pp. 2644-2647 (2013).

(4) Tran Trung Nghia, Kohei Yamamoto, Takeshi Namita, Yuji Kato, and Koichi Shimizu: “3D reconstruction of internal structure of animal body using near-infrared light,” Proc. SPIE Vol.8952, Biomedical Applications of Light Scattering IX, San Francisco, USA, Feb. 1-6, paper 89521A (2014).

(5) Trung Nghia Tran, Kohei Yamamoto, Takeshi Namita, Yuji Kato, and Koichi Shimizu: “Development of new optical CT for 3D animal imaging - Practical technique using transillumination images -,” Biomed. Imag. Sensing Conf., part of Opt. & Photon. Int. 2014 Cong., Yokohama, Japan, Apl. 22-24, in press (2014).

2. 論文（その他）

（1）なし

3. 講演（学位論文関係）

（1）Koichi Shimizu, Naoya Tobisawa, Trung Nghia Tran, Takeshi Namita, and Yuji Kato: “Application of transillumination imaging to injection assist system,” The 4th International Conference on the Development of Biomedical Engineering, Ho Chi Minh City, Vietnam, pp. 153-156

(Jan. 2012).

（2）Tran Trung Nghia, Kohei Yamamoto, Takeshi Namita, Yuji Kato, Koichi Shimizu: “Development of Scattering Suppression Technique for Reconstruction of Absorption Structure using Point Spread Function for Cylindrical Scattering Medium,” Optics & Photonics Japan 2012　日本光学会年次学術講演会, 東京都江戸川区, 演題番号 23pA6 (2012 年 10 月).

（3）チャン　チュン　ギア, 山本　航平, 浪田　健, 加藤　祐次, 清水　孝一:「点拡がり関数を用いた散乱抑制による生体内部構造の 3 次元像再構成」Optics & Photonics Japan 2013　日本光学会年次学術講演会, 奈良市, 演題番号 14pD2 (2013 年 11 月).

（4）山本　航平, 田中　宏幸, チャン　チュン　ギア, 浪田　健, 加藤　祐次, 清水　孝一:「生体透視イメージングのための点拡がり関数による吸光像改善の試み」Optics & Photonics Japan 2013　日本光学会年次学術講演会, 奈良市, 演題番号 14pD1 (2013 年 11 月).

（5）Tran Trung Nghia, Takeshi Namita, Yuji Kato, and Koichi Shimizu: “Development of new optical CT for 3D animal imaging, - Practical technique using transillumination images -,” 第 16 回ソウル大学・北海道大学 ジョイントシンポジウム, ソウル, 韓国 (2013 年 12 月).

（6）山本　航平, チャン　チュン　ギア, 浪田　健, 加藤　祐次, 清水　孝一:「光による生体透視イメージングのための拡散媒質内部吸光像の画像改善」電子情報通信学会　ME とバイオサイバネティックス研究会, 町田市, 演題番号 MBE2013-136 (2014 年 3 月).

（7）山本　航平, チャン　チュン　ギア, 浪田　健, 加藤　祐次, 清水　孝一:「2 波長を用いた拡散媒質内部吸収体の深さ推定-光による生体透視の高解像化をめざして-」第 53 回日本生体医工学会大会, 仙台市 (2014 年 6 月).

4. 特許

なし

以　上